ErAs:In(Al)GaAs Photoconductive Mixers as Continuous-Wave Terahertz Detectors: Modelling and Applications

Dem Fachbereich Elektrotechnik und Informationstechnik
der Technischen Universität Darmstadt
zur Erlangung des akademischen Grades eines
Doktor-Ingenieurs (Dr.-Ing.)
genehmigte

Dissertation

von

M.Sc.
Anuar de Jesus Fernandez Olvera
aus Alvarado, Veracruz, Mexico

Referent:	Prof. Dr. rer. nat. Sascha Preu
Korreferent:	Prof. Dr. Guillermo Carpintero del Barrio
Tag der Einreichung:	30.11.2021
Tag der mündlichen Prüfung:	21.02.2022

Darmstadt 2022

Fernandez Olvera, Anuar de Jesus:
ErAs:In(Al)GaAs Photoconductive Mixers as Continuous-Wave Terahertz Detectors: Modelling and Applications

Darmstadt, Technische Universität Darmstadt,
Year thesis published in TUprints: 2022
URN: urn:nbn:de:tuda-tuprints-213403
Date of the viva voce: 21.02.2022

Abstract

This thesis demonstrates two application-oriented terahertz (0.1-10 THz) systems developed with ErAs:In(Al)GaAs photoconductors, and introduces new models to describe their performance as terahertz detectors.

ErAs:In(Al)GaAs photoconductors, and photoconductors in general, have been widely used as terahertz emitters and detectors in homodyne terahertz spectrometers for more than a decade. However, some fundamental aspects of their operation as terahertz detectors had not been fully modelled yet. The first part of this thesis proposes new models for those fundamental aspects. Such models are not only valid for ErAs:In(Al)GaAs photoconductors, but also for any short carrier-lifetime photoconductive mixer acting as a CW terahertz detector. The focus is on two aspects: the influence of the driving laser on the noise performance, and the relationship between the incoming terahertz power and the current output by the mixer.

The existing models for noise in short carrier-lifetime photoconductors neglect the influence of laser noise assuming that thermal noise is the dominant one. However, experimental evidence shows the contrary, at least for the optical power levels normally used in photoconductors. Thus, the model proposed in this thesis incorporates the influence of laser noise and that of generation-recombination noise into the picture. Its predictions were tested experimentally.

Since no comprehensive models to quantitatively describe the relationship between incoming terahertz power and output current existed for CW photoconductive detectors, the one proposed here for that purpose is the first one of its kind. Its predictions were confirmed by experimental measurements.

In addition to these models applicable to CW photoconductive terahertz detectors, the first part of this thesis also introduces a model to perform a detailed estimation of the spectral structure of the terahertz pulses emitted by a pulsed photoconductor when pumped by a MLL. Such models are required to examine some of the applications presented in the second part of this thesis.

The second part of this thesis consists of two different applications developed using ErAs:In(Al)GaAs photoconductors working as CW terahertz detectors.

The first one is a novel detection technique for terahertz pulses emitted by pulsed photoconductors driven by MLLs. The novel detection technique, coined FreSOD, allows to detect each of the modes composing a terahertz pulse with a resolution that exceeds by several orders of magnitude the resolution achieved with any time-domain optoelectronic detection technique. Such spectral resolution is not only relevant for terahertz measurements, but also for the characterization of the noise in the MLL driving the pulsed photoconductor.

The second one is a fully optoelectronic spectrum analyzer for the sub-terahertz

range operating without the need of an external electronic spectrum analyzer. The demonstrated resolution is on the 1-Hz level, with an operating range that goes from 0.05 to 0.09 THz. The range can easily be extended to more than 0.3 THz with relatively minor modifications.

Kurzfassung

In dieser Arbeit werden zwei anwendungsorientierte Terahertz-Systeme (0.1-10 THz) vorgestellt, die mit ErAs:In(Al)GaAs-Photoleitern entwickelt wurden, und es werden neue Modelle zur Beschreibung ihrer Leistung als Terahertz-Detektoren eingeführt.

ErAs:In(Al)GaAs-Photoleiter und Photoleiter im Allgemeinen werden seit mehr als einem Jahrzehnt in großem Umfang als Terahertz-Emitter und -Detektoren in Homodyn-Terahertz-Spektrometern eingesetzt. Einige grundlegende Aspekte ihrer Funktionsweise als Terahertz-Detektoren sind jedoch noch nicht vollständig modelliert worden. Im ersten Teil dieser Arbeit werden neue Modelle für diese grundlegenden Aspekte vorgeschlagen. Diese Modelle gelten nicht nur für ErAs:In(Al)GaAs-Photoleiter, sondern auch für alle photoleitenden Mischer mit kurzer Ladungsträgerlebensdauer, die als CW-Terahertz-Detektoren eingesetzt werden. Der Schwerpunkt liegt dabei auf zwei Aspekten: dem Einfluss des treibenden Lasers auf das Rauschverhalten und der Beziehung zwischen der eingehenden Terahertz-Leistung und dem vom Mischer abgegebenen Strom.

Die bestehenden Modelle für das Rauschen in Photoleitern mit kurzer Ladungsträger-lebensdauer vernachlässigen den Einfluss des Laserrauschens und gehen davon aus, dass das thermische Rauschen dominiert. Experimentelle Beweise zeigen jedoch das Gegenteil, zumindest für optische Leistungspegel, die normalerweise in Photoleitern verwendet werden. Das in dieser Arbeit vorgeschlagene Modell bezieht daher den Einfluss des Laserrauschens und des Generations-Rekombinationsrauschens in die Betrachtung mit ein. Die Modellvorhersagen wurden experimentell getestet.

Da keine umfassenden Modelle zur quantitativen Beschreibung des Verhältnisses zwischen der eingehenden Terahertz-Leistung und dem Ausgangsstrom für CW-Photoleiter-Detektoren existieren, ist das hier vorgeschlagene Modell das erste seiner Art. Die theoretischen Vorhersagen wurden durch experimentelle Messungen bestätigt.

Zusätzlich zu diesen Modellen, die auf CW-photoleitende Terahertz-Detektoren anwendbar sind, wird im ersten Teil dieser Arbeit auch ein Modell zur detaillierten Abschätzung der spektralen Struktur der Terahertz-Pulse vorgestellt, die von einem gepulsten Photoleiter emittiert werden, welcher mit einem MLL gepumpt wird. Solche Modelle sind erforderlich, um einige der im zweiten Teil dieser Arbeit vorgestellten Anwendungen zu untersuchen.

Der zweite Teil dieser Arbeit befasst sich mit zwei verschiedenen Anwendungen, die mit ErAs:In(Al)GaAs-Photoleitern als CW-Terahertz-Detektoren entwickelt wurden.

Bei der ersten Anwendung handelt es sich um eine neuartige Detektionstechnik für Terahertz-Pulse, die von gepulsten, durch MLLs betriebenen Photoleitern ausgesendet werden. Die neuartige Detektionstechnik, FreSOD genannt, ermöglicht es, jede der

Moden, aus denen sich ein Terahertz-Puls zusammensetzt, mit einer Auflösung zu detektieren, die die Auflösung anderer bisheriger Zeitdomänen-Detektionstechniken um mehrere Größenordnungen übertrifft. Eine solche spektrale Auflösung ist nicht nur für Terahertz-Messungen von Bedeutung, sondern auch für die Charakterisierung des Rauschens des MLL, die den gepulsten Photoleiter antreibt.

Der zweite ist ein rein optoelektronischer Spektrumanalysator für den Sub-Terahertz-Bereich, der ohne einen externen elektronischen Spektrumanalysator funktioniert. Die gezeigte Auflösung liegt im 1-Hz-Bereich, und der Betriebsbereich beträgt 0.05 -0.09 THz. Der Bereich kann mit relativ geringen Modifikationen leicht auf mehr als 0.3 THz erweitert werden.

Contents

Abstract **i**

1. Introduction **1**
1.1. Motivation . . . 1
1.2. Overview of Available Technologies for Terahertz Generation and Detection . . . 3
1.3. Thesis Outline . . . 8

2. Fundamentals of Photoconductive Mixers **11**
2.1. Introduction . . . 11
2.2. Basic Concepts . . . 11
2.3. Photocondutive Mixer Modelling . . . 13
2.3.1. Long Carrier-Lifetime Photocondutive Mixers, Narrow Absorption Region . . . 15
2.3.2. Short Carrier-Lifetime Photoconductive Mixers . . . 19
2.3.3. Short Carrier-Lifetime Photoconductive Mixers as Terahertz Detectors . . . 31
2.4. Noise in Short Carrier-Lifetime Photoconductive Mixers . . . 39
2.5. Coherent and Non-Coherent Detection in Photoconductive Mixers . . . 47
2.5.1. Coherent Detection . . . 47
2.5.2. Non-Coherent Detection . . . 48

3. ErAs:In(Al)GaAs Photoconductive Terahertz Detectors **49**
3.1. Introduction . . . 49
3.2. State of the Art . . . 49
3.3. ErAs:In(Al)GaAs Photoconductors as Terahertz Detectors . . . 53
3.4. Characterization of ErAs:InGaAs Photoconductors . . . 56
3.4.1. Responsivity Characterization . . . 58
3.4.2. NEP Characterization . . . 63
3.5. Excess Noise Reduction in ErAs:In(Al)GaAs Photoconductors . . . 65
3.6. Conclusion and Outlook . . . 69

4. Application 1: Frequency Selective Optoelectronic Downconversion of Pulses **71**
4.1. Introduction . . . 71
4.2. The Frequency Selective Optoelectronic Downconversion Process . . . 73
4.3. Spectral Characteristics of Downconverted Terahertz Pulses . . . 75
4.3.1. Experimental Demonstration . . . 80

4.3.2. Ultra High-Resolution Characterization of a Filter 81
4.3.3. Comparison of the 750^{th} and 3400^{th} terahertz modes 86
4.4. Conclusions 91

5. Application 2: A Sub-Terahertz Optoelectronic Spectrum Analyzer 93
5.1. Introduction and State of the Art 93
5.2. Spectrum Analyzer Architecture 95
5.2.1. EO-based Subsystem for CW Local Oscillator Generation . . . 95
5.2.2. Photoconductive Mixer 97
5.2.3. Intermediate Frequency Chain 99
5.3. Operation Modes 100
5.3.1. Operation Mode I (Wide-Span Mode) 100
5.3.2. Operation Mode II (High-Resolution Mode) 100
5.4. Measurements 101
5.4.1. Measurements with Operation Mode I 101
5.4.2. Measurements with Operation Mode II 103
5.5. Analysis of the Measurement Results 106
5.6. Conclusions and Outlook 108

6. Conclusion and Outlook 109

A. Appendix 1: Fabrication of ErAs:In(Al)GaAs Photoconductive Mixers 113

B. Acronyms 115

C. List of Own Publications 117

D. Acknowledgments 119

Bibliography 121

1. Introduction

1.1. Motivation

The terahertz region is perhaps the last region of the electromagnetic spectrum to be fully explored. Loosely, it is usually defined as the region located between the microwaves and the optical frequencies. Formally, it is usually defined as the frequency band going from 0.1 THz to 10 THz.

Being between optics and microwave engineering, the field of terahertz science and technology employs techniques from both realms, since after all, they deal with the same kind of phenomena: non-ionizing EM waves. However, unlike in those well established fields, no inexpensive sources and detectors have been developed for terahertz waves yet. The reason is that the periods of the terahertz waves are too fast for most conventional electronics, while their photon energy is too small for traditional optical devices based on interband transitions. This is what makes the terahertz field technically and scientifically interesting.

Besides being technically and scientifically interesting in itself, historically, the terahertz region has been very relevant for two important applications: high-speed communications [1, 2] and spectroscopy [3, 4]. These two applications have been the driving force of the field of terahertz science and technology for many years. However, applications such as non-destructive testing [5] and imaging [6] have gained importance after a series of key developments, and they are now seen as the future drivers of the field.

The relevance of the terahertz region for high-speed communications is quite evident, the higher the frequency of a communication system, the higher the available bandwidth, as beautifully expressed by the Shannon-Hartley theorem [7]. With the emergence of 5G, the allocated carrier frequencies of communication systems has been pushed up to 0.071 THz [2]. Future demands will only push it further.

The relevance of the terahertz range for the field of spectroscopy requires more elaboration. Historically, the optical frequencies, in particular the near-infrared and the mid-infrared range, have been the ones used by chemists to perform molecular spectroscopy, given that most of the molecular vibrations have spectral features that appear in that range. However, the rotations of gaseous polar molecules have features that appear in the terahertz and the sub-terahertz range [3]. Important polar molecules such as water, carbon monoxide, ammonia or hydrogen cyanide have strong rotational spectral features in the terahertz range. Indeed, such features have been utilized to perform astronomical observations with highly sophisticated spectrometers sent to space missions [8]. Such observations allowed the detection of water vapor in the asteroid belt of our solar system [9], using the rotational

spectral feature of water located at 0.557 THz. However, not only the rotation of gaseous polar molecules show spectral features in the terahertz range, vibrations of long molecular chains and intermolecular vibrations also do [3], given the weak nature of such long-range interactions. This means that for the case of solids, both intramolecular and intermolecular arrangements play a role on the appearance of terahertz spectral features, allowing to investigate not only the molecular composition of some solids but also their crystalline structure [10]. Examples of solid substances that show spectral features of interest to security applications in the terahertz range are cocaine, crack cocaine, MDMA (also known as ecstasy), heroin, amphetamine, carbamazepine, among many others [11]. In fact, by probing their crystalline structure using terahertz spectroscopy, it is possible to determine not only the purity of such substances, but also their sole presence [11]. This is usually known as terahertz fingerprinting detection, and it has been one of the major applications of terahertz technology, since it can be done contactless and without the need of any additional substances.

Although terahertz communications and spectroscopy are promising and interesting applications, their market relevance is not very significant yet, either because the market is very limited, as in the case of terahertz spectroscopy, or because of the market is not very mature yet, as in the case in terahertz communications. In contrast, terahertz non-destructive testing has gained significance over the last couple of years, becoming relevant for the manufacturing industry, in particular, for the quality control during the manufacturing polymer-based components, composite materials, textiles, pharmaceutical tablets, adhesives, paint coatings and electronic components [5]. This is because using terahertz waves for testing offers many competitive advantages compared to the existing available solutions, mostly based on ultra-sound waves, X-ray or infrared waves. Compared to ultra-sound waves, for example, terahertz waves do not require a contact medium, they are contactless due to the their EM nature. Moreover, some materials, like polymer foams, absorb or reflect ultrasound waves very strongly. Compared to X-rays, terahertz waves are non-ionizing, therefore, they are not hazardous to humans and do not require all the special protections required when working with X-rays. In addition, many materials relevant to the manufacturing industry are almost transparent to X-rays, offering little contrast. Finally, compared to infrared waves, terahertz waves can travel through materials that are optically opaque, like paint coatings, textiles or polymer-based and composite materials. All of these competitive advantages make terahertz technology a unique alternative for non-destructive testing, with a maturity that already permits industrial exploitation. Indeed, there are already many commercial terahertz products targeting that market, from devices to monitor the painting process in the car-manufacturing industry [12], to systems that monitor to the quality of plastic blow molding [13]. The development and improvement of such products and systems is now driving many of the recent advances in the terahertz field, like the development of terahertz cameras to optimize the monitoring process [14, 15], or the development of higher-power terahertz sources [16, 17].

1.2. Overview of Available Technologies for Terahertz Generation and Detection

The main problem with the development of the aforementioned products and applications still remains the same: the time scales associated with terahertz waves are too fast for conventional electronics, while the associated photon energies are too small to develop optical devices based on interband transitions such as laser diodes or photodetectors. Owing to this fact, the development of terahertz technology has been traditionally divided into three clearly defined groups:

1. Technology entirely based on a conventional electronic approach, such as voltage controlled oscillators or rectifying diodes, which directly generate or detect terahertz radiation at the lower frequency end of the terahertz range.

2. Technology based on optical approaches, such as quantum cascade lasers, molecular gas lasers and the so-called non-linear optical methods.

3. Terahertz technology based on optoelectronic approaches, in which the beating signal between two or more optical waves is transformed into a terahertz photocurrent by means of a fast photoconductor or a fast photodiode.

The topic of this thesis, terahertz detection by photomixng using ErAs:In(Al)GaAs photoncondutive mixers, is a technology that belongs to the third group. However, to clearly point out its advantages and disadvantages, I will briefly review all three groups mentioned before.

Let me start with terahertz technology based on conventional electronics. The fundamental element for the development of most conventional electronic components is the transistor, since it is the element the provides gain to any circuit. Hence, in order to have an active terahertz components based on conventional electronics, one must first have transistors operating in the terahertz range. This is very challenging for several reasons, but the main one is the short period of the terahertz waves. For the lowest frequency of the range, i.e. 0.1 THz, this is equal to 10 ps. For many transistor designs, this means that electrons between their terminals must be transported much faster than that for the transistor to work properly. Hence, transistors working at these frequencies must not only be small but also must be optimized for fast electron transport. The transistor with the highest frequency performance demonstrated so far is an Indium Phosphide (InP) high-electron-electron mobility (HEMT) with a 25-nm gate. It exhibited a 9 dB gain at 1 THz when working as an amplifier [18]. However, no fundamental oscillator emitting at that frequency has been demonstrated with that kind of technology so far. The fundamental oscillator with the highest frequency demonstrated so far is a 25-nm-gate InP heteorjunction-bipolar-transistor (HBT) based differential oscillator, emitting at 0.57 THz [19]. Higher emitted frequencies have been demonstrated with other transistor technologies, but none of such oscillators was emitting in its fundamental mode. For example, a 1.1-THz emitter composed of 42 fundamental oscillators all coherently emitting at their fourth harmonic has been

recently demonstrated with 130-nm-gate silicon-germanium (SiGe) HBTs by the RLE at MIT [20]. The total emitted power was measured to be 80 μW, while the injected DC power was 1.1 W, already indicating the limitations of this approach. Using only CMOS technology, the highest-frequency emitter demonstrated is 0.61-THz Colpitts oscillator emitting at its fifth harmonic [21]. The oscillator was implemented using 0.65-nm-gate CMOS transistor, and it emitted 5 μW for a total input DC power of 17 mW. Even higher frequencies can be achieved by using non-linear elements such as varactors, Schottky diodes or active mixers, which act as frequency multipliers, but one adds noise or loses power in the process [22].

Non-coherent emission at frequencies as high as 2 THz has also been demonstrated from AlGaN/GaN HEMT transistors [23, 24] owing to emergence of plasma oscillations, however, their non-coherent nature complicates its usage for most of the interesting terahertz applications. In fact, such devices are much closer to a superluminescent diode than to a conventional electronic oscillator. A device that is much closer to a conventional electronic oscillator but that is not based on transistors is the resonant-tunneling diode (RTD). It consists of a gain medium, arising due to a negative differential resistance exhibited under proper biasing conditions, and a high quality factor resonator attached to it. Given that the negative differential resistance exhibits a very fast dynamics, this type of oscillator can be implement efficiently over most of the terahertz range. The highest emitted frequency by an RTD so far is in the range of 1.92 THz, with a power of 0.4 μW [25], although powers as high as 1 mW have been reported for 0.26 THz [26]. Due to the relative simplicity of their design and competitive performance, they have been recently used in many high-speed communications experiments.

Regarding the detection of terahertz waves using conventional electronic devices, the most successful technologies so far have been Schottky diodes together with HEMT and CMOS transistors, both technologies operating as passive direct detectors. Owing to its non-linear electrical characteristics, a Schottky diode can easily rectify an incoming terahertz wave. Since no gain is required in direct detection, their performance is mostly limited by their diffusion and their junction capacitance, which are anyway low for a Schottky diode. This has allowed them to reach sensitivities as low as 1.5 pW for detection bandwidths of 1 Hz at 0.15 THz [27]. Indeed they have been the work horse of the terahertz research community performing communication experiments [1], although they have also been used regularly in spectroscopic and astronomical applications [28, 29]. The reason for their success is their simple planar lithographic construction, which results in small and convenient devices which can be easily mounted in other circuits, together with the fact that they do not require cyrogenic cooling. Moreover, low-barrier Schottky diodes have relatively low impedances, which allows a good matching with the 50 Ω impedance exhibited by the RF equipment used in high-speed communications and astronomical applications. Regarding the use of HEMT and CMOS transistors as direct terahertz detectors, their operation mechanism is more sophisticated than just non-linear rectification, and it can be divided into cases: resonant and non-resonant [30]. Their non-resonant operation is based on the propagation of the terahertz wave to be detected into

the transistor channel, where it decays into a steady DC current as it propagates thought it [30]. Their resonant operation is based on the excitation of a plasma wave in the transistor channel, enhancing the responsivity of the detection process [31]. However, this only occurs under appropriate resonant conditions [32]. Such plasmonic behaviour is closely related to the mechanism responsible for the emission of non-coherent terahertz radiation in AlGaN/GaN HEMT transistors mentioned before. Owing to the different nature of their rectification mechanism, transistor-based detectors have shown relatively flat performances up to 2 THz, with sensitivites reaching 70 pW at 1.5 THz for detection bandwidths of 1 Hz [33]. Narrowband designs have even shown sensitivities of around 15 pW at 0.2 THz for the same detection bandwidth [34].

Terahertz technology based on optical approaches dates back to the seventies, when the first molecular gas lasers were developed [35]. To my knowledge, they are the oldest technology used for the emission of coherent terahertz radiation. They use gaseous polar molecules having radiative rotational states in the terahertz range as a gain medium, which is usually pumped by a carbon dioxide laser. The excited gas molecules then relax, emitting terahertz radiation. By using different methanol isotopes, for example, a plethora of terahertz lasers emitting between between 0.1 and 15 THz have been produced [36]. More recently, a variation of this method, which instead of changing the lasing medium changes the pumping frequency, has been able to lase at 37 different different frequencies between 0.255 and 0.955 THz [37]. Each emitted line had a kHz linewidth and a power higher than 1 mW. The system was compact and operated at room temperature, making it a competitive option. The gain medium used was nitrous oxide, while the pumping laser was a tunable quantum cascade laser operating in the mid-infrared range.

Quantum cascade lasers are actually one of the most promising optical technologies in the terahertz range. Originally demonstrated in the mid-infrared range [38], they have been continuously optimized to work at the terahertz range [39, 40]. Unlike molecular gas lasers, the gain medium in quantum cascade lasers is based on expitaxially grown quantum wells, either made from GaAs/AlGaAs or from InGaAs/InAlAs. This makes them compact and allows to flexibly select their operating frequency, since the lasing frequency just depends on the cavity length and on the quantum well design, not on the discrete spectral features of some polar molecule. However, their operation at terahertz frequencies requires cryogenic cooling [39, 40], or at least some form of cooling. This is because, unlike in traditional laser diodes, the transitions responsible for the stimulated emission which are required to have optical gain, are not interband transitions but intraband transitions, given the small photon energies associated with the terahertz waves. Such intraband transitions are the result of the epitixially-grown quantum well structures, which originate from the periodical intercalation of of InGaAs and InAlAs layers, or GaAs and AlGaAs layers, depending on the material system used. Hence, in order to achieve population inversion within such closely spaced energy levels in the conduction band, it is necessary to cool down the laser. Nonetheless, recent developments have demonstrated emitted powers as high as 50 mW at 4 THz by just using electronic temperature controllers and not a

cryostat [41], an achievement that underscores the potential of this technology.

Due to their small photon energy, no such thing as interband-transition photodetectors exist for terahertz frequencies below 1.5 THz, and even those working above that range need to be cryogenically cooled to avoid the conduction band to be filled with electrons that would otherwise be thermally excited at room temperature [42]. However, there are terahertz technologies that do allow to probe the discrete quantum nature of terahertz radiation, and that precisely works for the lower terahertz range: SIS mixers and hot-electron bolometers.

SIS mixers are the most sensitive terahertz detectors for the lower end of the terahertz frequency range, routinely achieving quantum level sensitivities, with levels that are enough to detect as a few as two photons at 0.171 THz [43]. Their structure is rather simple, it consists of a very thin insulating layer sandwiched between two superconducting metal layers. The presence of the thin insulating layer creates a small potential barrier between the quasiparticles in each of the superconductors, which under the presence of a wave with a sufficiently low photon energy can be overcome to generate a net current between the two superconductors [44]. This process is called photon-assisted tunneling and can be seen as analogous to the generation of an electron-hole pair in an direct-bandgap photoconductor [44]. Thus, when two waves with similar frequencies, and consequently similar photon energies, are both incident on the SIS junction, they mix, generating a intermediate frequency current, which can be easily detected by an spectrum analyzer after low-noise amplification. However, the detailed modelling of this process requires a quantum-mechanical treatment [45]. It should also be pointed out that SIS mixers usually require cryogenic cooling close to 0 K to achieve superconducting behaviour, moreover, they require an external terahertz local oscillator to perform the mixing process, therefore broadband operation is difficult to achieve.

Due the photon-assisted tunneling properties of the superconductors, SIS mixers only work well for frequencies below 1 THz. Above that range, hot-electron bolometers take their place [44]. Although their operation mechanism is not based photon-assisted tunneling, they are also based on a superconducting element, but driven very close to its critical temperature [44]. Similarly, they reach quantum level-sensitivities.

With the exception of electronic direct detectors, which cannot preform frequency-resolved detection, the frequency range covered by the technologies discussed so far is rather narrow or not continuously tunable. This is because they are based on truly fundamental terahertz oscillators, which require a cavity to operate. When a broadband coverage is required, non-linear optical methods are usually employed.

The idea behind this approach is simple, to make use of the mature laser technology developed for the visible and near-to-visible frequencies in order to generate terahertz waves via non-linear frequency mixing. For example, if one takes two red-light lasers, one emitting at 400 THz, and another other one emitting at 401 THz, and one makes them incide on a crystalline material with high non-linear permittivity and low optical absorption, the non-linear interaction between the waves results in the generation of the sum and frequency difference as independent polarization terms [46]: the difference-frequency term is at 1 THz, and the sum-frequency term at 801

THz. Something similar occurs in a varactor diode when biased by two closely spaced RF frequencies.

Thus, since this approach is based on just transforming radiation already generated in the optical domain into the terahertz domain, it exhibits the following advantages:

1. Tunability and frequency coverage. Given that the frequency of the lasers can be tuned very easily and in a continuous manner, it is virtually possible to generate any desired terahertz frequency.

2. Coherence. Since the ultimate sources of the generation process are the lasers, the generated terahertz signals inherit their high coherence.

3. Room temperature operation. Unlike quantum cascade lasers or SIS mixers, it works very well at room operation.

4. Cost. Since they do not require a cryostat, and tunable lasers are relative inexpensive, this approach is a very cost-effective solution.

However, since the generation mechanism of this approach is a non-linear effect, it usually requires high amounts of optical power to work. Moreover, being a non-linear process akin to the one occurring in a varactor diode, it follows the Manley-Rowe relations, meaning that one highly-energetic optical photon must generate one low-energetic terahertz photon. Hence, it is not energetically efficient. For example, in order to generate 2 mW of average power at 1.9 THz, one needs 500 W of optical laser power [47].

If one wants to keep all the aforementioned advantages, but improve the optical-to-terahertz conversion efficiency, then optoelectronic terahertz technology is the way to go.

Unlike non-linear mixing, optoelectronic terahertz technology is based on a linear process: the absorption of an optical wave by a photoconductive material. This process scales linearly as a function of incident average optical power, hence, it requires much less laser power to work. The terahertz generation occurs due to the emergence of a photocurrent proportional to the amount of absorbed optical power by the photoconductive material after the application of a bias. Since the amount of electron and holes in the photocurrent is directly proportional to the average optical power, its value will follow the envelope of the time-varying optical intensity, resulting in the generation of components with frequencies equal to the frequency differences existing between the absorbed optical signals.

For example, if the two optical signals from before, i.e. the one at 400 THz and the one at 401 THz, are incident on a photoconductive material, the rate at which the number of electron-hole pairs are generated in the material will be given by the time average of the square of the sum of both optical fields, i.e. to the time-averaged total instantaneous optical intensity. Since the time average must be taken at the time in which optical absorption occurs, the sum-frequency component vanishes, leaving only a DC term and a 1 THz frequency component.

Note that the power in the generated terahertz photocurrent is given by the applied external bias, the optical power just determines what should be its magnitude. This is in stark contrast with the process of non-linear mixing, where the generated terahertz power comes entirely from the incident optical signal. This fundamental difference is what ultimately has allowed optoelectronic terahertz emitters to reach very high optical-to-terahertz conversion efficiencies, with emitted terahertz powers as high as 0.1 mW generated using only 1.4 mW of optical power [48]. All, while still keeping all the aforementioned advantages, i.e., tunability, frequency coverage, coherence, room temperature operation and low cost.

Although not self-evident, the optoelectronic approach can also be used for terahertz detection. For this, the optically generated charge density oscillating at the terahertz frequency is used as a local oscillator in order to downconvert an incoming terahertz field. In this respect, optoelectronic detectors are much more advantageous than simple electronic direct detectors, since they can provide the frequency and the phase of the detected signals without the need any filters or additional electronic local oscillators. This is extremely useful, and it is why they are so widely used in spectrometers and non-destructive testing instruments. Indeed the topic of this thesis is the use of photoconductors for the detection of CW, terahertz signals. In particular, the use of ErAs:In(Al)GaAs photoconductors, which are compatible with telecom-wavelength lasers. This allowed the use of several optical components developed for the telecom industry, and thus enabled the construction of sophisticated tunable laser systems that otherwise would not have made possible the applications demonstrate here.

The detailed description of the operation mechanism and the performance ErAs :InGaAs photocondutive mixers[1] as terahertz detectors, as well their use in the development of different terahertz applications, will be the topic of thesis.

1.3. Thesis Outline

The thesis can be roughly divided into two parts. The first part composed of Chapter 2 and 3, deals mainly with the theoretical modelling and characterization of the performance of CW ErAs:In(Al)GaAs photoconductive mixers operating as terahertz detectors, while the second part, composed of Chapter 4 and 5 deals with with their use in different applications, which mostly target the development of measurement tools for the further development of terahertz components.

Chapter 2 explains the fundamental principles of photocondutive mixing in a general way, without specializing them for ErAs:In(Al)GaAs photonconductors. Besides only explaining their vary basic principles, this chapter proposes a different approach to model their performance in detail. Although the focus of this thesis is on CW terarhertz detection, the pulsed case is also treated in this Chapter, given that some of the theoretical results are needed for the analysis of some of the developed applications. The proposed approach is useful because it allows to estimate how the

[1]The terms photoconductive mixer and photoconductor are used interchangeably in this thesis.

terahertz power is distributed between the different frequency components involved in the mixing process, something that is difficult to estimate with the existing theoretical approaches. Finally, this chapter also proposes a new theoretical model to explain noise in photocondutive mixers acting as terahertz detectors.

Chapter 3 gives an overview of the the state of the art of terahertz photoconductive detectors operating with telecom-wavelength lasers. It also presents an experimental characterization of the responsivity and the sensitivity of ErAs:In(Al)GaAs photoconductive detectors operating in a CW homodyne scheme. The experimental characterization is then used as a basis to establish a comparison with the estimated responsivity predicted by the theoretical model presented in Chapter 2. The experimentally measured properties of the noise in ErAs:In(Al)GaAs photoconductors are also analyzed and compared with the noise theory proposed in Chapter 2.

Chapter 4 presents a new technique for the detection of terahertz pulses implemented using CW ErAs:In(Al)GaAs photoconductive detectors. The presented technique has a resolution that exceeds by several orders mangnitude the resolution usually achieved in pulsed photocondutive-based terahertz spectrometers. Moreover, it can be used as diagnostic tool for the noise characterization of the MMLs widely used in terahertz generation. Extensive use of the theoretical approach presented in Chapter 2 is used to explain its working principle.

Chapter 5 demonstrates a new spectrum analyzer architecture for the sub-terahertz range based on CW ErAs:In(Al)GaAs photoconductive detectors. The demonstrated spectrum analyzer architecture covers the 0.05-0.090 THz range, and achieves a resolution well into the Hz level. However, its frequency coverage and resolution can easily be extended. Two exemplary measurements of two different spectral lines, both emitted at around 0.072 THz, are shown.

Finally, Chapter 6 summarizes the most important findings in this thesis and discusses future directions for further developments, both theoretical and technological, that still need to be achieved in the field of CW photoconductive terahertz detectors.

2. Fundamentals of Photoconductive Mixers

2.1. Introduction

In this chapter, I present the fundamental concepts, models and formulas that explain the operation of photoconductive mixers. They will serve to explain the operation of all the presented terahertz applications. Although most of the applications in this thesis deal with photoconductive mixers acting as terahertz detectors, their operation as pulsed terahertz emitters is also treated here. There are two reasons for this. The first one is that some of the ideas and concepts required to model the operation of photoconducutive mixers as CW terahertz detectors are easier to understand if they are introduced first for the pulsed case. The second one is that the theoretical treatment for pulsed terahertz emitters will be required in subsequent chapters, where CW photoconductive mixers are used to detect a terahertz pulse emitted by another photoconductive mixer.

This chapter is intended to be as general as possible, so that the concepts, the models and the equations presented here can be applied to any kind of short carrier-lifetime photocondutive mixer, regardless of the wavelength used to drive it or the photoconductive material used to build it. Section 2.2 introduces the basic concepts and the physical limitations of the photomixing process behind the photoconductive mixers. Section 2.3 presents a detailed modelling of the operation of short carrier-lifetime photoconductive mixers acting as pulsed terahertz emitters and as CW terahertz detectors, starting by analyzing the limitations of long carrier-lifetime photocondutive mixers. The presented models are distinct to previous existing models used to describe the performance of photoconductive mixers, and they allow to estimate the relationship existing between the DC power of the biasing source driving a pulsed photoconductive mixer and the emitted terahertz power. They also suggest the emergence of additional terahertz harmonics in the detection process of a single CW terahertz signal. Section 2.4 lays out the a new theoretical model to explain noise in CW-photoconductive detectors. Finally, section 2.5 points out the differences between coherent and non-coherent detection in photoconductive mixers.

2.2. Basic Concepts

Photomixing is a process that converts an optical frequency difference existing between two or more optical waves, into one or more electrical waves. Depending on the optical frequency difference, the generated electrical wave can be in Hz range or in

the THz range. Regardless of the frequency range, the physics behind the conversion process remains the same, the only difference is the efficiency of the process.

The physical mechanism behind the optical-to-electrical conversion is the absorption process of an optical wave by a photoconductive material. Evidently, the bandgap of the photoconductive material must be smaller than the photon energy of the optical wave for this process to occur. If that is the case, the rate $\frac{d}{dt}N_e(t)$ at which the photoconductive material absorbs the energy of the optical wave to excite electrons from the valence to the conduction band is given by the average power of the optical wave $P_L(t)$ [49]

$$\frac{d}{dt}N_e(t) = \frac{\eta}{hf}P_L(t) \tag{2.1}$$

h being the Planck constant, f the frequency of the optical wave, T its period, and η the quantum efficiency of the photoconductive material, which in this case also includes the optical power lost due to reflections at its interface. The value of $P_L(t)$ is proportional to

$$P_L(t) \sim \left\langle \big(E_L(t)\big)^2 \right\rangle_T \tag{2.2}$$

$E_L(t)$ the optical field, and $\langle\rangle_T$ the time-average operator over period T. The time average must be done over the period of the optical wave, since this is the time scale at which optical absorption occurs. This is an important point, because it is what differentiates photomixing from other similar process such as mixing in a non-linear crystal. For example, for two optical waves with magnitudes $E_1(t)$ and $E_2(t)$, having the same field strength E_0 and the same polarization, but with angular frequencies $\omega_1 = 2\pi f_1$ and $\omega_2 = 2\pi f_2$, i.e.

$$E_1(t) = E_0 \cos(\omega_1 t) \tag{2.3}$$

$$E_2(t) = E_0 \cos(\omega_2 t) \tag{2.4}$$

photomixing results in

$$\frac{d}{dt}N_e(t) \sim \frac{\eta}{hf}E_0^2\Big(1 + \cos\big((\omega_1 - \omega_2)t\big)\Big), \tag{2.5}$$

meaning that electrons-hole pairs are generated at two different rates: a constant rate, proportional to the sum of the squared optical field strengths, and a varying rate, proportional to the the frequency difference existing between the two optical waves[1]. This is the essence of the photomixing process.

[1] Note that non-linear mixing, being proportional to just $\big(E_L(t)\big)^2$, would result in the generation of four frequency components: $2f_1$, $2f_2$, $f_1 - f_2$ and $f_1 + f_2$. By using single exponentials to represent the optical fields, as it is normally done for the description of the photomixing process, i.e. $E_0 e^{j\omega_1 t}$ and $E_0 e^{j\omega_2 t}$, one would never get these four frequency components that do emerge in non-linear mixing. This is why the real representation of the optical fields was chosen instead.

However, in order to use this difference-frequency signal resulting from the photomixing process, one still needs to transform the excited electron-hole pairs into an electrical current, requiring an external electrical field for the generation of a steady flow. This is where the finite velocity of electrons and holes in the photoconductive material becomes important, severely limiting the maximum frequency of the currents that can be generated by photomixing.

Qualitatively, this fundamental limitation can be explained by noting that the photoexcited carriers cannot be transported as fast as they are generated. Since an electron will generate a current for as long as it is being transported [49], the net result is the destructive interference of the continuously generated currents. Even the fastest direct-bandgap photoconductive materials exhibit (saturation) transport velocities that do not exceed 4×10^5 m/s [50]. If one considers a short transport length of 1 μm, one obtains a transport time of 2.5 ps, which corresponds to 0.4 THz. This means that currents with periods smaller than that will start to interfere partially destructively with each other when generated at different times, hence the difficulty of generating terahertz currents.

In spite of the transport-time limitation, the generation of high-frequency currents by photomixing is very easy to implement, given that it does neither require cryogenic cooling to operate nor the use of a high-frequency transistors. It only requires two optical waves, as a minimum, and a photoconductive material with the appropriate bandgap. This is why it is so widely popular for terahertz generation.

Due to their high coherence and high availability, lasers are normally used as the optical wave sources in the process. Since small relative changes in their optical frequency results in significant changes in the frequency of the generated terahertz current, wide tunability can be achieved with relatively narrow tuning ranges. For instance, for a 1.55-μm laser, with a frequency of 193 THz, a tuning of 1 THz corresponds to a tuning of 0.5% of its center wavelength. Indeed, terahertz currents of up to 4 THz have been generated via photomixing with modulated grating Y-branch lasers [51].

After photomxing, the generated terahertz current can either be emitted by an antenna, guided to some other circuit through a waveguide, or used as a local oscillator to detect an incoming terahertz signal via a mixing process. The latter is the main topic of this thesis, hence the name.

2.3. Photocondutive Mixer Modelling

In order to understand why short carrier-lifetime photoconductive mixers are required for efficient terahertz generation and detection, it is essential to understand, in a quantitative manner, how the finite transport time limits the photomixing process in a photoconductor. To this end, one can use the microscopic charge continuity equation, which relates the finite-velocity charge carrier flow, the generation rate and the carrier lifetime.

However, in order to use the charge continuity equation, it is first necessary to

find the relationship between the charge velocity $\vec{v}_d$, the external biasing field $\vec{e}_b$ and the charge flow. If one assumes relatively long time scales (longer than the scattering time of the photoconductor), then, on average, the carrier acceleration process can be seen a linear process mediated by the carrier mobility μ. For most direct-bandgap photocondutive materials, the mobility of the electrons is much higher than that of the holes. Therefore, only electrons will be considered from now on, and μ will represent the electron mobility, which is taken to be constant. Thus,

$$\vec{v}_d = -\mu\vec{e}_b, \tag{2.6}$$

resulting in a net current flow density $\vec{j}(r,t)$ given by

$$\vec{j}(\vec{r},t) = n(\vec{r},t)e\vec{v}_d. \tag{2.7}$$

where $\vec{r}$ represents the spatial coordinate, $n(\vec{r},t)$ the volume electron density and e the electron charge.

For electrons, the charge continuity equation then states that any point inside an infinitesimal volume of the photoconductor, the rate at which the number of electrons changes must be equal to the rate at which they are generated minus the rate at which they are recombined, plus any changes in the current flow. In other words, charge must be conserved. Mathematically, this can be expressed as

$$\frac{\partial}{\partial t}n(\vec{r},t) = -\frac{1}{\tau}n(\vec{r},t) + \frac{1}{e}\nabla\cdot\vec{j}(\vec{r},t) + g(\vec{r},t) \tag{2.8}$$

where τ is the recombination time and $g(\vec{r},t)$ the generate rate, determined by the laser power. Note that the changes in the current flow are accounted by $\nabla\cdot\vec{j}(\vec{r},t)$, meaning that for a constant flow of electrons inside the volume, $\vec{j}(\vec{r},t)$ plays no role in Eq. 2.8. However, in reality, for a time-varying electron density, it is not possible to have a constant flow of electrons inside a photoconductor, even if $\vec{v}_d$ is constant and $g(\vec{r},t)$ is spatially uniform over the whole photoconductor volume. This is a direct result of the finite transport velocity, which will always end up sweeping out of the photoconductor much faster the electrons that were generated closer to one of its bounding faces, resulting in charge accumulation in the opposite bounding face. Therefore, Eq. 2.8 cannot be independently solved for $\vec{r}$ or for t, except for some special cases that result from a few simplifying assumptions. However, for those cases, this first continuity equation enables to adequately model the electron time dynamics.

In addition to charge, energy must also be conserved, meaning that the rate at which the photoconductive mixer gives out energy must equal the rate at which is given energy. This can be simply expressed as

$$\langle p_{in}(t)\rangle_T = \langle p_{out}(t)\rangle_T \tag{2.9}$$

which just says that the time-averaged power given to the photoconductor $\langle p_{in}(t)\rangle_T$ must be equal to the time-averaged power dissipated or emitted by the photoconductor

$\langle p_{out}(t)\rangle_T$. The key for the enforcement of this equation is the realization that the energy required for the emergence of an optically generated current comes from the biasing field.

The enforcement of charge and energy conservation allow to model the performance of photoconductive mixers, acting as emitters or detectors in CW or in pulsed operation, in great detail.

Three cases will be distinguished in each of the following subsections:

1. The case in which τ is long as compared to the time required for the electrons to be transported, resulting in negligible recombination during transport. Thus, this case allows a quantitative analysis of the limitations purely related to the the transport time. For simplicity, only the CW case in which the electrons are generated over a narrow region of the photoconductor will be treated.

2. The case in which τ is short as compared to the time required for the electrons to be transported. In this case, recombination dominates the transport process, and the transport-time dynamics can be neglected. Both CW and pulsed terahertz generation will be treated since the photoconductors used in this thesis fall into this case, i.e. they are short carrier-lifetime photoconductors. The ultimate goal of this subsection is to determine the terahertz power distribution of the generated terahertz pulses in photoconductors through the enforcement of the energy conservation.

3. The case of terahertz detection in short carrier-lifetime photoconductors, in which the transport-time dynamics can only be partially neglected in spite of the short carrier lifetime exhibited the photoconductors. The ultimate goal of this subsection is the determination of the power responsivity of CW photoconductive mixers acting a CW terahertz detectors, also through the enforcement of the energy conservation.

2.3.1. Long Carrier-Lifetime Photocondutive Mixers, Narrow Absorption Region

For the case in which the electrons are generated in a small region with length l_g, thickness d and width l, as shown in Fig. 2.1, and where τ is long as compared to the time required for the electrons to be transported out of the generation region by the constant field $\vec{e}_b$, Eq. 2.8 reduces to

$$\frac{d}{dt}n(t) = g(t) \tag{2.10}$$

i.e. the rate of change of electrons is equal to the generation rate. Note that the spatial dependence in Eq. 2.10 has been dropped due to the assumption of a small absorbing region with little spatial variation.

Eq. 2.10 implies that the magnitude of the electron flow density at the end of the generation region $j_g(t)$ should be given by

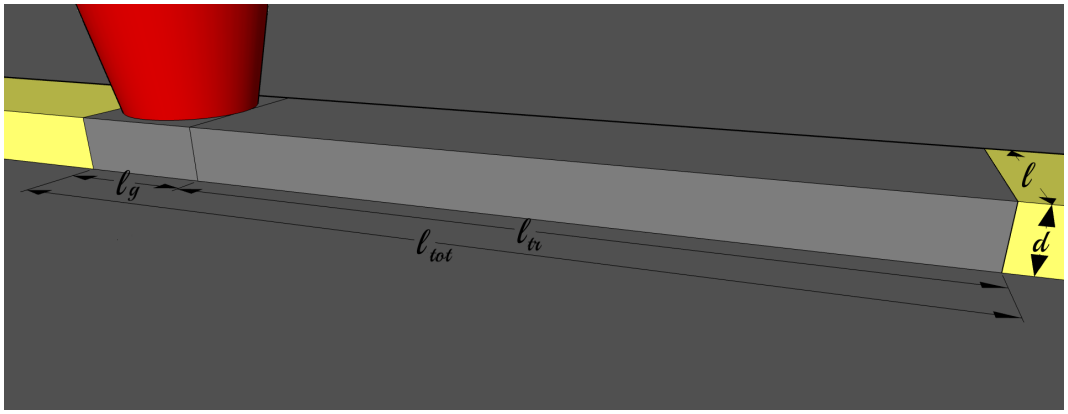

Figure 2.1.: Graphical depiction of the photoconductor geometry for the long carrier-lifetime case and a narrow absorbing region.

$$j_g(t) = e g_{cw}(t) l_g \tag{2.11}$$

where $g_{cw}(t)$ is the generation rate for a CW optical excitation. Its value must be given by the time-averaged intensity $I_{CW}(t)$ of the incident optical beam, composed of two optical waves with angular frequencies $\omega_1 = 2\pi f_1$ and $\omega_2 = 2\pi f_2$. For simplicity, it will be assumed that both optical waves have the same field strength $E_{CW,0}$ and the same polarization. Thus[2],

$$I_{CW}(t) = \frac{1}{Z}\left(E_{CW,0}^2 + E_{CW,0}^2 \cos\left((\omega_1 - \omega_2)t\right)\right). \tag{2.12}$$

Formally, $I_{CW}(t)$ must exhibit a spatial dependence, reflecting how the total optical power $P_{CW}(t)$ in the optical beam is distributed over space. For most cases, this spatial distribution is Gaussian or close to Gaussian [52]. However, due to the small absorbing region assumption made before, a uniform optical power distribution will be used, implying that $P(t) = I(t)S$, S being the the transverse surface of the beam. Under these assumptions,

$$g_{cw}(t) = \frac{1}{d}\frac{\eta_{eff}}{hf}\frac{E_{CW,0}^2}{Z}\Big(1 + \cos(\omega_{THz} t)\Big) \tag{2.13}$$

where Z is the impedance of the medium, $\omega_{THz} = \omega_1 - \omega_2$ and the effect of the finite optical absorption has been incorporated in η_{eff}. Note that it has been assumed that $f = \frac{f_1+f_2}{2}$ represents well the absorption at both f_1 and f_2.

After generation, the electrons are transported by the biasing filed $\vec{e}_b$ with velocity $\vec{v}_d$, resulting in waves of current flow propagating in the longitudinal direction x towards it respective collecting electrode, having a magnitude

[2]Since a real representation of the field is used, there is no need to include the additional factor of two multiplying Z.

$$j_g(t,x) = \frac{l_g}{d}\frac{e\eta_{eff}}{hf}\frac{E_{CW,0}^2}{Z}\left(1+\cos\left(\omega_{THz}\left(t-\frac{x}{v_d}\right)\right)\right). \tag{2.14}$$

These waves of electron flow will interfere with each other during their transit time from the generation point to the electrode, resulting in a frequency roll-off.

To determine such frequency roll-off, one can take the spatial average of the current flow magnitude over the whole photoconductive region length $l_{tot} = l_g + l_{tr} \approx v_d\tau_{tr}$, τ_{tr} being the time that the electrons take to go through l_{tr} [53]. One is allowed to do that because $l_{tr} \gg l_g$, and thus the transport is dominated by the properties of the non-absorpbing region where no electrons are generated or lost. This implies that the electron flow can be assumed to be steady, and hence one does not lose or gain any charges in the averaging process.

If one neglects the influence of the generated displacement current flow, the magnitude of this average current density j_{avg} is simply given by

$$j_{avg}(t) = \frac{1}{l_{tot}}\int_0^{l_{tot}} j_g(t,x)dx \tag{2.15}$$

resulting in

$$j_{avg}(t) = \frac{l_g}{d}\frac{e\eta_{eff}}{hf}\frac{E_{CW,0}^2}{Z}\left(1+\mathrm{sinc}\left(\frac{\omega_{THz}\tau_{tr}}{2}\right)\cos\left(\omega_{THz}\left(t-\frac{\tau_{tr}}{2}\right)\right)\right) \tag{2.16}$$

after substituting x by $v_d t$ and using $l_{tot} \approx v_d\tau_{tr}$. Note that this is the same result given in [54].

Since $j_{avg}(t)$ was assumed to be steady, it is straight-forward to obtain the optically excited average current $i_{avg}(t)$ by using

$$i_{avg}(t) = j_{avg}(t)A \tag{2.17}$$

$A = ld$ being the transverse are of the photoconductor. Therefore,

$$i_{avg}(t) = ll_g\frac{e\eta_{eff}}{hf}\frac{E_{CW,0}^2}{Z}\left(1+\mathrm{sinc}\left(\frac{\omega_{THz}\tau_{tr}}{2}\right)\cos\left(\omega_{THz}\left(t-\frac{\tau_{tr}}{2}\right)\right)\right) \tag{2.18}$$

Two conclusions can be inferred from Eq. 2.18:

1. The average DC current due to the optically generated electrons is independent from the biasing electric field[3]. This might seem surprising but it is indeed expected. If the recombination of the electrons takes much longer than τ_{tr}, the rate at which one can pull the optically generated electrons out of the photoconductor must be determined by optical power for the case of a DC

[3] As long as the biasing field is different from zero. Otherwise there is no flow of electrons.

current. In other words, if they are not recombined on their way to the electrode, one should be able to recover all the optically generated electrons of the DC current. The effect of the finite transport velocity is just a delay.

2. The AC current due to the optically generated electrons does depends on the biasing electric field via τ_{tr}. The faster the optically generated electrons are transported, the less time the generated AC currents can interfere, and the higher the AC current value. This makes the amplitude of the AC current decrease as the frequency increases. Clearly, in the limit in which the electron transport can be taken to be instantaneous, one again recovers the DC value. However, with the usual transport times, this is only possible for low frequencies.

The ratio between AC and DC power produced by the optically generated current as a function of frequency can be readily obtained by taking the square of the ratio between the amplitudes of the AC and DC components of Eq. 2.18. The envelope of the ratio $\eta_{tr}(f)$ can be approximated as

$$\eta_{tr}(f_{THz}) = \frac{1}{1 + (2 f_{THz} \tau_{tr})^2}, \tag{2.19}$$

as given in [54], which is a very useful expression for the quantitative analysis of the limitations in long carrier-lifetime photoconductors. For example, if one takes the previously estimated transport time of 2.5 ps for a 1 μm transport length and and optimistic transport velocity of 4 $\times 10^5$ m/s, one obtains that even for 0.2 THz $\eta_{tr} = 0.5$, and the photoconductor would produce two times more heat than terahertz power. This excessive amount of heat ultimately leads to the thermal destruction of the photoconductor. This is why long carrier-lifetime photoconductors are not used for CW terahertz generation or detection. For this reason, the analysis of the energy conservation will not be performed.

The point of this subsection was rather to illustrate the limitations of long carrier-lifetime photoconductors under the assumption that electrons are all generated in a very narrow region close to one of the electrodes. On the one hand, this case can be considered as a worst-case scenario, since a uniform generation over the whole photoconductive region would result in some electrons exhibiting shorter transport times, smoothing out the sharp dips exhibited by Eq. 2.18. On the other hand, if one would consider not only electron generation and transport, but also hole generation and transport over the whole photoconductive region, the heavy and slow holes would slow down the overall transport process. A full model incorporating such considerations requires a full solution to the system of partial differential equations set by Eq. 2.8 and its corresponding version for holes, a feat that is out of the scope of this thesis. Still, the illustrative case that has been considered here allows to identify the strategies that can bu used to overcome the limitations imposed by the transit time:

1. Improving the electron transport process in the photoconductor: So far it has been assumed that the electrons move with a constant velocity. In fact, electron

transport in photoconductors is not that simple and the holes make the process even more complicated. However, for very short distances and under proper biasing conditions, electrons can be transported ballistically [55], significantly reducing the transport time. This is usually done with terahertz PIN diodes, but its design requires the use of sophisticated simulation tools and its fabrication the use of advanced technological process.

2. Decreasing the transport distance: In principle, one can reduce the distance the electrons need to travel by making the electrode separation very small. However, this also decreases the amount of generated electrons due to the reduced dimensions of the resulting photoconductive structure and may increase the capacitance of the structure, making it store any generated terahertz power. This results in a roll-off for higher terahertz frequencies, usually known as RC roll-off. Still, such approach can be implemented with the right engineering techniques. This is usually done with plasmonic photoconductors [56, 57], but the lithographic techniques required to produced them ($l_{tr} < 1$ μm) limits the implementation possibilities.

3. Reducing the lifetime of the optically generated electrons: If the lifetime of the electrons is much smaller than τ_{tr}, the magnitude of the generated DC current is decreased, and consequently the generated heat. Moreover, the time in which the generated AC currents can interfere with themselves is reduced, increasing the AC frequency that can still propagate without excessive heat generation. This is the approach used in this thesis for the development of photoconductive mixers for terahertz detection. In its most basic versions, this approach is the easiest to implement. However, the most sophisticated versions demand state-of-the-art material science engineering, as it will be shown in later chapters.

2.3.2. Short Carrier-Lifetime Photoconductive Mixers

Before proceeding with the analysis of the charge and energy conservation equations corresponding to short carrier-lifetime photoconductive mixers when employed for terahertz generation, it is pertinent to discuss some relevant aspects about short carrier-lifetime photoconductors. In particular, what are the implications of a short carrier lifetime, and the trade-offs that often need to be done to get an adequate short carrier-lifetime photoconductive material.

The lifetime of an optically excited electron in a photoconductor, i.e. the time that it spends in the conduction band being able to be accelerated to generate a current, depends on the mechanism dominating the recombination of excited electrons and holes. There are two types of recombination processes in a photoconductor, and in general in any semiconductor: radiative recombination and non-radiative recombination [58]. In the first one, the excited electron directly recombines with a hole in the valence band, resulting in the emission of a photon [58]. This process is the predominant one in light emitting diodes (LEDs) and lasers, however, it is very

slow compared to the transport times required for terahertz generation. Therefore, it does not play a significant role in photoconductive mixers analyzed here.

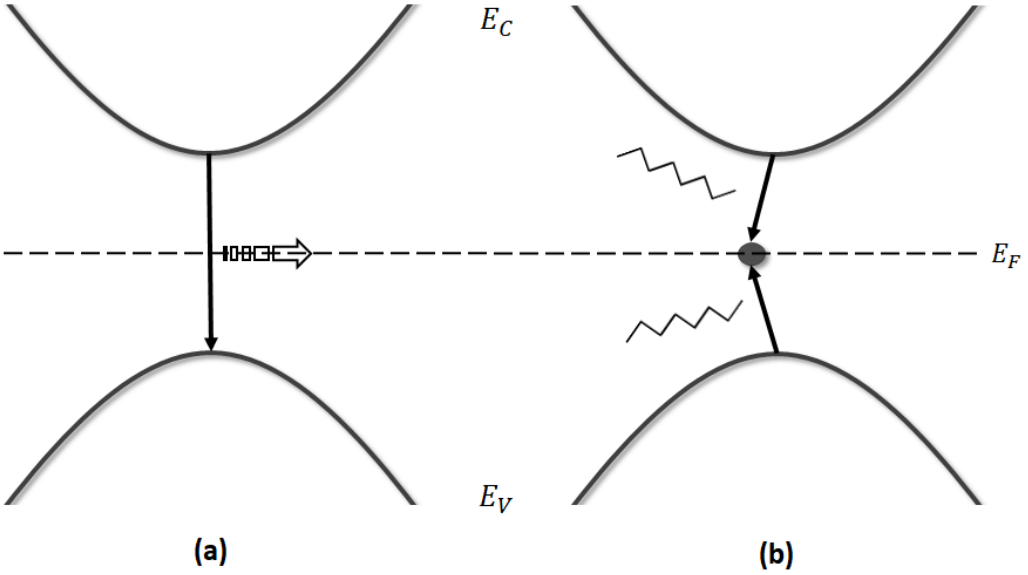

Figure 2.2.: Graphical representation of the two different recombination processes in the energy-momentum space. (a) Radiative recombination. (b) Shockley-Read-Hall recombination in a trap state located close to the Fermi energy level. E_C represents the conduction band, E_V represents the valence band and E_F the Fermi level.

In the second type of recombination[4], the excited electron recombines with a hole via a midgap state, as as shown in Fig. 2.2 (b). Since this is not a direct transition, phonons are usually emitted during the process. This is known as Shockley-Read-Hall recombination, and it involves two-steps: the transition of an electron to the midgap state and the subsequent transition of a hole to the same state [58]. The order of the transitions can also be reversed, the key requirement is that both, an electron and a hole, are captured by the same midgap state so that they recombine. The midgap states have their origin in defects within the crystalline structure making up the photoconductor. However, in order to be effective recombination centers, the midgap states need be to be located deep within the bandgap. Otherwise, the electrons (holes) can easily go back to the conduction (valence) band and do not stay long enough to recombine with a carrier of opposite charge.

There are different ways of introducing defects in the crystalline structure of a photoconductive material. The most common one is adding defects while growing

[4]In theory, there is another type of non-radiative recombination process which involves the transfer of energy to a second electron, the so-called Auger recombination [58]. However, since it involves the excitation of another electron, it is not a desirable process in photoconductors used for terahertz generation

it [58]. However, one can also introduce them via ion implantation [58] or simply by altering the temperature at which the crystalline photoconductive material is grown [59]. In general, the higher the density of the defects the more recombination centers, and the shorter the carrier lifetime [58]. However, introducing defects has more consequences than just reducing the lifetime.

First of all, it may spoil the crystalline structure of the photoconductor. Further, the defects are also efficient scatterers, impacting the host lattice ability to transport the electrons efficiently once they are excited. In practice this means a reduced mobility [58].

Secondly, their presence alters the position of the Fermi energy. This is a direct result of their ionization, which, in the worst case, makes the defects to effectively behave as dopants. In case the energetic levels of the defects are indeed very close to center of the bandgap, their presence usually decreases the background conductivity, i.e. the amount of electrons that are excited without any optical excitation or biasing field. However, if such defects are easily ionizable due to the an energetic closeness to the conduction or the valence band, their presence will increase the dark conductivity. A high background conductivity results in a poor thermal performance, given that even a small biasing field results in a very high idle DC current, usually called dark current. This current does not produce any terahertz but it does produce heat. In fact, in the energy conservation equations derived in this thesis, the effect of the dark currents will be neglected, assuming that their magnitude is much smaller than the one of the optically generated currents. However, in some short carrier-lifetime photoconductive materials this is not necessarily the case. The issue is especially critical in narrow bandgap photoconductors like InGaAs, the photoconductive material required for telecom-wavelength operation, where small shifts in the Fermi level can result in drastic changes in the background conductivity [60].

The details about the photoconductive materials for optimal operation at telecom-wavelengths will be discussed in the next Chapter. However, after this brief discussion, it must be clear that achieving a short carrier lifetime in a photoconductive material is much more complicated than just incorporating defects into its structure. In most cases, there is no optimum solution, and one faces a trade-off between achieving a short carrier life time or low dark conductivity.

With a short carrier lifetime, i.e. $\tau \ll \tau_{tr}$, and a constant biasing field $\vec{e}_b$, the charge continuity equation can be reduced to

$$\frac{d}{dt}n(t) = -\frac{1}{\tau}n(t) + g(t). \tag{2.20}$$

where the $g(t)$ is now acting over the whole photoconductor, as shown in Fig. 2.3. The short carrier lifetime of the electrons allows to drop the spatial derivatives appearing in Eq. 2.8, given that, on average, no electrons can propagate more than $v_d\tau$, hence, everything that happens after that distance becomes irrelevant. This is also the reason why $g(t)$ can now be allowed to act over the whole photoconductive region, whereas on a long carrier-lifetime photoconductor, the same condition would lead to charge accumulation, resulting in a significant spatial dependence even for

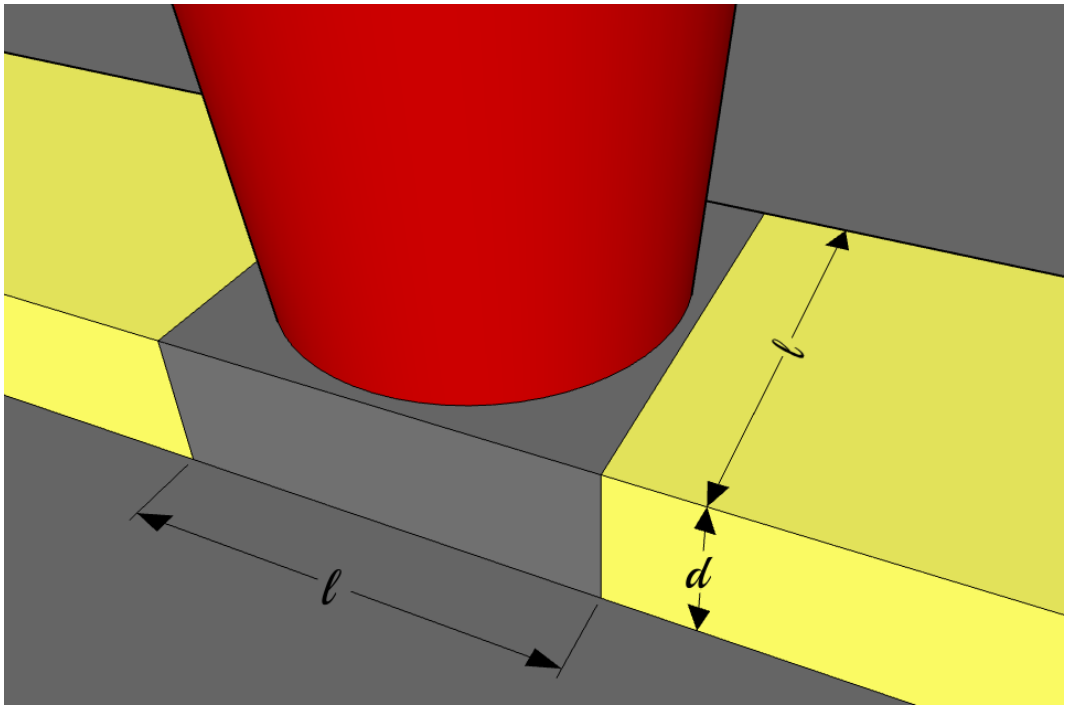

Figure 2.3.: Graphical depiction of the photoconductor geometry for the short carrier-lifetime case.

constant and uniform bias $\vec{e}_b$.

In other words, when τ becomes very short as compared to all the other time constants of the photoconductor, it completely dominates the electron dynamics.

Under those conditions, and for the CW generation term given by Eq. 2.13, the steady-state solution to Eq. 2.20 is

$$n_{cw}(t) = \frac{\tau}{d}\frac{\eta_{eff}}{hf}\frac{E_{CW,0}^2}{Z}\left(1 + \frac{\cos(\omega_{THz}t + \phi_{cw})}{\sqrt{1+(\omega_{THz}\tau)^2}}\right) \tag{2.21}$$

with $\phi_{cw} = \arctan(\omega_{THz}\tau)$, which is the same solution found in [61] and [54] for this case. The magnitude of the generated current density $j_{cw}(t)$ then reads

$$j_{cw}(t) = \frac{v_d\tau}{d}\frac{e\eta_{eff}}{hf}\frac{E_{CW,0}^2}{Z}\left(1 + \frac{\cos(\omega_{THz}t + \phi_{cw})}{\sqrt{1+(\omega_{THz}\tau)^2}}\right). \tag{2.22}$$

Note that no spatial average is performed now, given that the length over which the current flows can interfere is very small. The value of the total generated current $i_{cw}(t)$ can easily be obtained using Eq. 2.17, resulting in

$$i_{cw}(t) = v_d\tau l\frac{e\eta_{eff}}{hf}\frac{E_{CW,0}^2}{Z}\left(1 + \frac{\cos(\omega_{THz}t + \phi_{cw})}{\sqrt{1+(\omega_{THz}\tau)^2}}\right) \tag{2.23}$$

l being the total generation length, a shown in Fig. 2.3. A significant difference between this result and the one obtained for the long carrier-lifetime case, i.e. Eq. 2.18, is the fact that the DC current due to the optically generated electrons now depends linearly on the biasing electric field as $\vec{v}_d = \mu\vec{e}_b$. This is a direct consequence of the fact that, due to recombination, it is not possible to recover all the optically excited electrons.

The reduction in the DC current due to the recombined electrons, with respect to the value obtained in the long carrier-lifetime case, is given by $g = \frac{v_d\tau}{l} = \frac{\tau}{\tau_{tr}}$. In most references [54], g is referred to as the photoconductive gain, although it is much smaller than unity. The importance of this smaller-than-unity gain is that it results in the generation of much less heat compared to the long carrier-lifetime case. Moreover, since τ can be made as small as a few hundreds of femtoseconds by introducing the appropriate kind of defects in the photoconductor, the frequency at which the photoconductive mixer starts to generate more heat than terahertz power is increased significantly. This the reason why short carrier-lifetime photoconductive mixers are regularly used for terahertz generation.

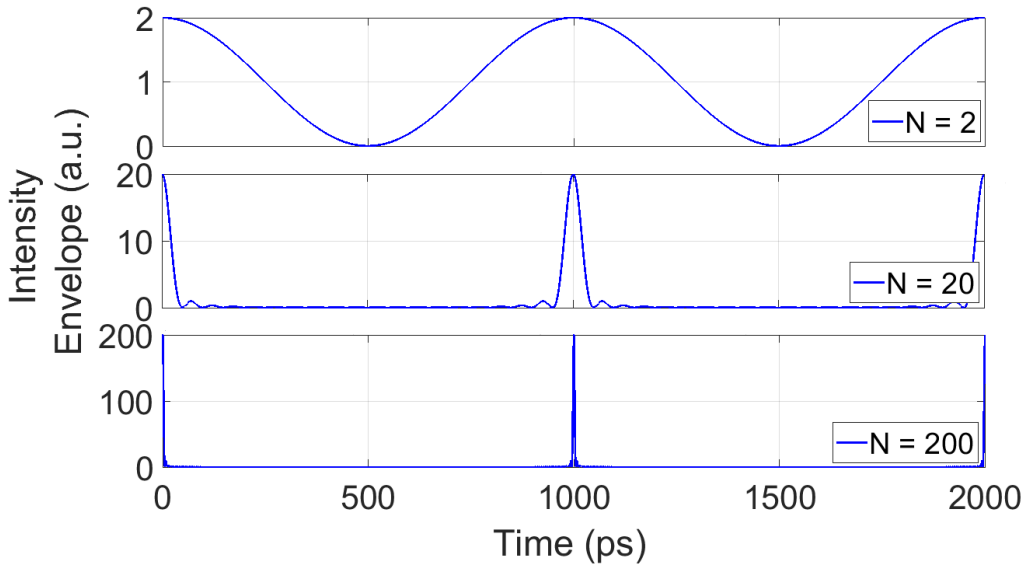

Figure 2.4.: Resulting optical excitations for an increasing number N of optical waves. The optical waves, or modes, are assumed to have the same field strength and polarization. The frequency difference $\Delta\omega$ between any two spectrally adjacent modes is set to 0.001 THz. Note that the case $N = 2$ is the one usually referred to as CW.

Although modelling the performance of a short carrier-lifetime photoconductor under a CW optical excitation is interesting for a direct comparison with the performance of a long carrier-lifetime photoconductor, the relevant case for the purposes of this thesis is the modelling of a short carrier-lifetime photoconductor

under a pulsed optical excitation for terahertz emission. Usually, these two cases are treated separately [54], with different equations governing their carrier dynamics. However, this does not necessarily needs to be the case. Indeed, the CW case can be seen a special case of the pulsed case, as shown in Fig. 2.4. To realize this, one just needs to consider the spectral structure of the ultrashort optical pulses used to excite the photoconductive mixers during pulsed operation.

At this point, a clarification needs to be made. Here, the term ultrashort optical pulse will refer to the output of an MLL with a duration of a few hundreds of femtoseconds. Those are the kind of optical pulses most commonly used in modern pulsed terahertz systems. The treatment presented here will apply specifically for that case.

An ultrashort optical pulse generated by a MLL is just a collection of optical waves with different frequencies in which the frequency separation between each of the waves is regularly spaced by the repetition rate, and the phase relationship between them is kept constant. Each of these optical waves is referred to as a mode. Mathematically, the total magnitude of its optical field $E_{PL}(t)$ can be described as [62]

$$E_{PL}(t) = \sum_{n=0}^{N-1} E_{PL,0} \cos\big((\omega_{PL} + n\Delta\omega)t\big) \tag{2.24}$$

where n is the mode index, $E_{PL,0}$ the field strength of each mode, $\omega_{PL} = 2\pi f_{PL}$ the lowest angular frequency above lasing threshold, $\Delta\omega = 2\pi\Delta f$ and Δf the mode spacing. $N\Delta f$ is the bandwidth of the pulse, and it is what determines the pulse duration when no chirping is present (as implicitly assumed here).

For a uniform spatial distribution in the optical beam, the magnitude of the time-averaged optical pulse intensity $I_{PL}(t)$ is given by

$$I_{PL}(t) = \frac{1}{Z}\left(\frac{N}{2}E_{PL,0}^2 + \sum_{n=1}^{N-1} E_{PL,0}^2 (N-n)\cos(n\Delta\omega t)\right). \tag{2.25}$$

an expression that can be proven by mathematical induction. Please note that it has been assumed all modes have the same field strength. This just means that the temporal structure of the pulse is sinc-squared shaped, having a slightly longer temporal duration than a Gaussian-shaped pulse.

The optical excitation term $g_{pl}(t)$ for the continuity equation then becomes

$$g_{pl}(t) = \frac{1}{d}\frac{\eta_{eff}}{hf_{PL}}\frac{E_{PL,0}^2}{Z}\left(\frac{N}{2} + \sum_{n=1}^{N-1}(N-n)\cos(n\Delta\omega t)\right). \tag{2.26}$$

where, as a good simplifying approximation, the photon energy, hf_{PL} was also chosen the same for all frequency components. Formally, they just differ by less than 4 %.

By substituting the generation rate of Eq. 2.26 into Eq. 2.20, it is possible to find the dynamics of the electron density $n_{pl}(t)$ in a short carrier-lifetime photoconductor

for an optical pulsed excitation, again, one just needs to solve the differential equation for the steady-state case[5], which results in

$$n_{pl}(t) = n_{pl,0} + \sum_{n=1}^{N-1} n_{pl,n} \cos(\omega_n t + \phi_n) \tag{2.27}$$

with

$$n_{pl,0} = \frac{\tau}{d} \frac{\eta_{eff}}{hf} \frac{E_{PL,0}^2}{Z_0} \frac{N}{2} \tag{2.28}$$

and

$$n_{pl,n} = \frac{\tau}{d} \frac{\eta_{eff}}{hf} \frac{E_{PL,0}^2}{Z} \frac{(N-n)}{\sqrt{1+(\omega_n \tau)^2}} \tag{2.29}$$

for $n > 0$, where $\omega_n = n\Delta\omega$ and $\phi_{pl,n} = \arctan(-\omega_n \tau)$.

While the current excited in the photoconductor for this case $i_{pl}(t)$ can be written as

$$i_{pl}(t) = i_{pl,0} + \sum_{n=1}^{N-1} i_{pl,n} \cos(\omega_n t + \phi_n) \tag{2.30}$$

with

$$i_{pl,0} = v_d \tau l \frac{e\eta_{eff}}{hf} \frac{E_{PL,0}^2}{Z_0} \frac{N}{2} \tag{2.31}$$

and

$$i_{pl,n} = v_d \tau l \frac{e\eta_{eff}}{hf} \frac{E_{PL,0}^2}{Z} \frac{N-n}{\sqrt{1+(\omega_n \tau)^2}} \tag{2.32}$$

for $n > 0$.

The advantage of treating the pulsed case as a collection of modes is that it allows to estimate the emitted terahertz power by each of the individual modes. This advantage becomes evident when incorporating the photoconductor resistance to the analysis, which is a strong function of frequency (or time, depending on how one sees it). It is this clear separation between the DC component and the different AC components that ultimately allows to enforce energy conservation by equating the biasing power to the consumed terahertz power for each and every component.

To do so, one first needs to find the equivalent circuit of a photoconductive mixer directly attached to an antenna. In principle, there are two different two options: the one originally proposed by E. Brown [61] in his seminal paper, favored mostly

[5]Since the equation is linear, it is possible solve it for the DC component and for each of the AC modes separately, and then just add the steady-state solutions to find the total pulsed electron carrier density.

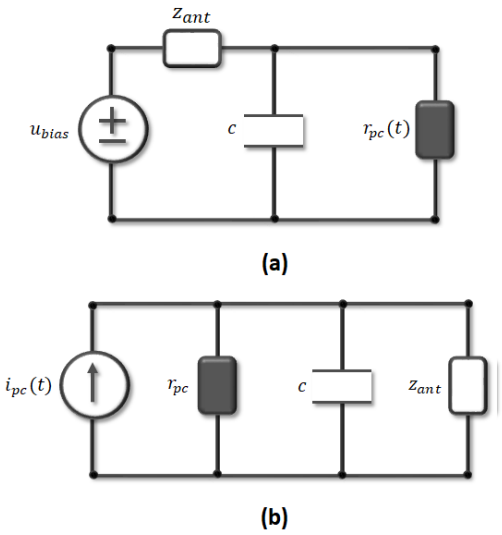

Figure 2.5.: (a) Equivalent circuit proposed by Brown et al. in [61]. (b) Equivalent circuit proposed by Duffy et al. in [63]. In both circuits i_{pc} represents the optically excited current, c the capacitance of the electrodes, z_{ant} the antenna impedance and r_{pc} the photoconductor resistance. In (a) u_{bias} represents the applied DC bias.

in British universities [64, 65], and the one originally proposed by S.M. Duffy et al. [63], favored everywhere else [54, 66, 67]. Both models are depicted in Fig. 2.5. Here, it was decided to use a synthesis of both to be able to get an equivalent circuit that incorporates the effect of the biasing source, but that at the same time models the photoconductor as a voltage-dependent current source.

The devised equivalent circuit is shown in Fig. 2.6 (a). For the sake of clarity in the analysis, only the photoconductor without antenna is considered in the equivalent circuit, the antenna will be incorporated later. The key feature of the equivalent circuit is the fact that the power for the terahertz emission is provided by the DC source. The photoconductor transforms the DC power into AC terahertz power by accelerating the optically excited electrons. The amount of power that needs to be given to each of them is determined by the number of excited electrons and by their velocity. Thus, it is ultimately determined by the MLL power, the electron mobility, and the applied biasing field. The first two set the value of the resistance, while all three set the value of the current for each modes.

In this sense, the photoconductor is similar to a brushed DC motor, which also transforms DC power into AC power. Hence, it is possible to write a similar power balance equation using the previously defined currents for each of the modes, the resistances of each of them, and the applied bias. This results in

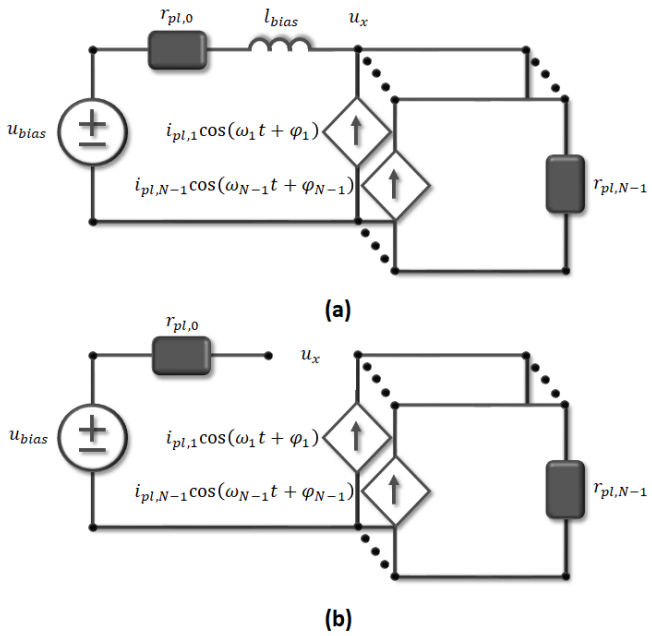

Figure 2.6.: (a) Proposed equivalent circuit of a photoconductive mixer operating as a pulsed terahertz emitter (without antenna). (b) Simplified version of the proposed equivalent circuit.

$$u_{bias} i_{pl,0} = i_{pl,0}^2 r_{pl,0} + \sum_{n=1}^{N-1} \frac{1}{2} i_{pl,n}^2 r_{pl,n} \tag{2.33}$$

where $r_{pl,n}$ is the resistance of each of the modes, u_{bias} the applied bias to the photoconductor, and where it has been assumed that the inductance of the biasing line l_{bias} is high enough so that no AC mode can propagate through the DC path[6] and that the terahertz power can be modeled as an electromotive force. In fact, if one omits the inductance of the biasing line, assuming that no modes will propagate through the DC path, and models the effect of the AC terahertz sources as an electromotive force u_x, the equivalent circuit can be redrawn as shown in Fig. 2.6 (b).

The left hand side of Eq. 2.33 is the available power, given by the DC biasing source but determined both by the applied voltage and the optical power. The right hand side of Eq. 2.33 represents the consumed average power. It is composed of a DC part and an AC part. The DC part is dissipated as heat. The AC part represents the power given to the voltage-dependent current sources of the equivalent circuit. In a DC motor, the DC power would be the one given to the armature resistance

[6] I have also neglected any non-linear effects that can arise due to the effect of the AC modes in the biasing. This is a reasonable assumption given that the DC biasing voltage is usually much higher than that of the voltages of the AC modes.

and to the armature inductance, while the AC power would be the one given to the electromotive force[7].

The absolute value of $r_{pl,n}$ depends on the photoconductor charge mobility under illumination and on the amount of charge per mode. However, if one assumes that the mobility under illumination is constant, the relative change in $r_{pl,n}$ as a function of mode number will depend only on the amount of available carriers per mode, which is entirely determined by the MLL and by the absorption in the photoconductive material. Therefore, one can rewrite the photoconductor resistance as a multiple of a fundamental resistance r_p using Eqs. 2.28 and 2.29. This results in

$$r_{pl,0} = \frac{2}{N} r_p \tag{2.34}$$

and

$$r_{pl,n} = \frac{\sqrt{1 + (\omega_n \tau)^2}}{N - n} r_p \tag{2.35}$$

for $n > 0$. After substituting Eq. 2.34 and Eq. 2.35 in Eq. 2.33, and subsequently solving for r_p, one obtains

$$r_p = \left(\frac{u_{bias}}{2 i_{pl,0}} \right) \left(\frac{N^2}{N + \sum_{m=1}^{N-1} \frac{N-m}{\sqrt{1+(\omega_m \tau)^2}}} \right). \tag{2.36}$$

Finally,

$$r_{pl,0} = \left(\frac{u_{bias}}{i_{pl,0}} \right) \left(\frac{N}{N + \sum_{m=1}^{N-1} \frac{N-m}{\sqrt{1+(\omega_m \tau)^2}}} \right) \tag{2.37}$$

and

$$r_{pl,n} = \left(\frac{u_{bias}}{2 i_{pl,0} (N - n)} \right) \left(\frac{N^2 \sqrt{1 + (\omega_n \tau)^2}}{N + \sum_{m=1}^{N-1} \frac{N-m}{\sqrt{1+(\omega_m \tau)^2}}} \right). \tag{2.38}$$

for $n > 0$. Please note that $i_{pl,0}$ is just the measured DC photocurrent in the photoconductor and u_{bias} the applied DC bias, so these expressions are rather simple to evaluate once the number of modes, the repetition rate of the MLL and the carrier lifetime in the photoconductor are known. Also note that the knowledge of $i_{pl,0}$, the aforementioned parameters and Eqs. 2.31 and 2.32, allows to determine $i_{pl,n}$ for each and every mode. This avoids the usage of u_{bias} in the determination of the values of $i_{pl,n}$, which in turn would require an accurate knowledge of the photoconductor mobility under illumination in order to obtain $r_{pl,0}$. Still, one must keep in mind

[7] Note that in a photoconductor the current is determined by the incident laser power and by the number of modes, while in a DC motor the current is determined by the mechanical load attached to it.

that the value of $i_{pl,n}$ depends on $\frac{u_{bias}}{l}$, or more precisely on $\frac{u_x}{l}$, and that that value of u_x is in turn given by

$$u_x = u_{bias} - \frac{i_{pl,0}}{r_{pl,0}} \tag{2.39}$$

as can be determined from the equivalent circuit of Fig. 2.6 (b).

The usage of this procedure for the determination of $r_{pl,n}$ and $i_{pl,n}$ implies a change of view in the way one normally sees the resistance of a pulsed photoconductive mixer. It is usually thought that the large biasing fields applied to pulsed photoconductive mixers reflect a relatively high illuminated resistance, but Eqs. 2.37 and 2.38 indicate that such high biasing fields are mostly used to accelerate the carriers of the thousands of modes excited in the photoconductor. This in turn means that the true DC resistance, and that of the first few hundreds of modes, is actually much lower than usually thought. This conclusion has been reached before but with a less rigorous method in [67], and it has important consequences for the estimation of the emitted terahertz power, as it will be shown here and in Chapter 4.

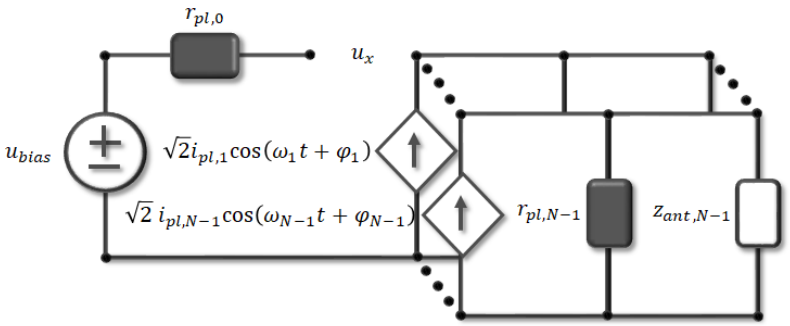

Figure 2.7.: Proposed equivalent circuit of a photoconductive mixer operating as a pulsed terahertz emitter incorporating the antenna.

To determine the amount of emitted terahertz power, one has to incorporate the antenna to the equivalent circuit, modelled by its impedance $z_{ant,n} = r_{ant,n} + jx_{ant,n}$, as shown in Fig. 2.7. In some references, an additional term is also added to account for the capacitance of the two electrodes of the photoconductive mixer. In [54, 66], for example, it is assumed that when the reactance associated with such capacitance becomes comparable to $z_{ant,n}$, it shorts the antenna, giving rise to the so-called RC roll-off. However, in most pulsed photoconductive mixers, the electrode structure is big enough for their effect to be already taken into account in the EM antenna simulations used to obtain $z_{ant,n}$. In fact, when the electrodes are relatively long, their effect is rather inductive than capacitive, as shown in [67]. Thus, I will assume here that such effects are well captured by the EM antenna simulations, and that their contribution is incorporated in $x_{ant,n}$.

Note that due to the incorporation of the antenna in the circuit, the amplitude of the voltage-dependent current sources representing each of the modes has been

multiplied by $\sqrt{2}$. This factor guarantees that in the case of maximum transfer of power, the power is conserved in the equivalent circuit. This is easier to see after determining the amplitude of the terahertz current going to the antenna for each of the modes $i_{ant,n}$.

To do so, one first needs to calculate the the value of $i_{ant,n}$, given by

$$i_{ant,n} = \frac{r_{pl,n}}{r_{pl,n} + z_{ant,n}} \sqrt{2} i_{pl,n}, \tag{2.40}$$

according to the equivalent circuit of Fig. 2.7. Then, the radiated average power by the antenna for each of the modes $p_{pl,n}$ can be easily calculated using

$$p_{pl,n} = \frac{|i_{ant,n}|^2 r_{ant,n}}{2}. \tag{2.41}$$

If one evaluates the average radiated power for the case $z_{ant,n} = r_{pl,n}$, i.e. the case of maximum transfer or power, one obtains $\frac{i_{pl,n}^2 r_{pl,n}}{4}$. The same amount of average power stays in $r_{pc,n}$. Thus, the total average power in the circuit equals $\frac{i_{pl,n}^2 r_{pl,n}}{2}$, which is the available average power in each of the modes, as given by Eq. 2.33. If the factor of $\sqrt{2}$ was not incorporated, the total power in the circuit would be $\frac{i_{pl,n}^2 r_{pl,n}}{4}$.

Using Eq. 2.40, it is also possible to give an expression for the amplitude of the radiated terahertz field $e_{pl,n}$ for each modes, viz.

$$e_{pl,n} \sim \omega_n i_{ant,n}. \tag{2.42}$$

Ultimately, the total emitted terahertz average power $p_{pl,tot}$ can be written as

$$p_{pl,tot} = \sum_{n=1}^{N-1} p_{pl,n} \tag{2.43}$$

while the magnitude of the total emitted field $e_{pl,tot}(t)$ can be expressed as

$$e_{pl,tot}(t) = \sum_{n=1}^{N-1} e_{pl,n} \cos(\omega_n t + \phi_n). \tag{2.44}$$

In sum, the set of equations presented in this subsection allows for an estimation of the spectrum and power emitted by a short carrier-lifetime pulsed photocondutive mixer. The model can certainly be refined by using a non-constant mobility, a Gaussian pulse shape, or other nonidealities. One nonideality that certainly must not be neglected is the propagation loss $\eta_{prop,n}$ experienced by the terahertz pulse as it propagates through free space, which as a first approximation, can be written as [68]

$$\eta_{pl,n} = \frac{\eta_{min}}{1 + \left(\frac{\omega_c}{\omega_n}\right)^2} \tag{2.45}$$

where η_{min} is the minimum propagation loss experienced by the pulse as it propagates through the terahertz setup, and ω_c the frequency at which $\eta_{pl,n} = \frac{\eta_{pl}}{2}$.

Although the derivation of Eq. 2.45 is rather heuristic [68] (based on the numerical aperture of a finite-sized mirror or lens aperture), it models reasonably well the frequency behaviour of the parabolic mirrors and the other quasioptical elements usually present in a terahertz setup, which only start to show close-to-ideal behaviour for the higher frequency range due to the their finite size. The particular values of η_{min} and ω_c depend on the specific type of setup, the alignment, and on the antenna used.

Finally, as mentioned at the beginning, the equations presented here can also be used to estimate the emitted power for the CW case, since this is just the special case in which $N = 2$ and $\Delta\omega = \omega_{THz}$.

2.3.3. Short Carrier-Lifetime Photoconductive Mixers as Terahertz Detectors

The main difference between a short carrier-lifetime photoconductive mixer acting as a terahertz emitter and a short carrier-lifetime photoconductive mixer acting as a terahertz detector is the nature of the applied biasing field used to generate the optically excited current. While in a terahertz emitter one applies a static electric field, namely $\vec{e}_b$, in a detector one a applies a terahertz time-varying electric field $\vec{e}_{THz}(t)$. This time-varying field modulates the rate at which the optically excited electrons are transported out of the photoconductor, a process that can be approximated as a multiplication between the instantaneous electron density and the incident electric field by using Eqs. 2.6 and 2.7. In this sense, the photocondutive mixer indeed behaves as a mixer.

Under this simplified view, when the frequency of the biasing electric field is the same as the one of the optically excited electron density, the generated photocurrent is a rectified version of the biasing field. This is more evident in the CW case, as depicted in Fig. 2.8. Note that magnitude of the generated DC current in the rectification process is influenced by the phase difference between the incident field and the optical signals used to pump the photoconductor. Therefore, a photoconductive mixer is able to detect not only the magnitude of $\vec{e}_{THz}(t)$, but also its (relative) phase. Although this is only possible as long as the terahertz signal and the optical signals are mutually coherent, as it will be discussed in the last section of this Chapter. For the time being, it will be assumed that they are all mutually coherent.

Since the mixing process depends on the magnitude of $\vec{e}_{THz}(t)$, the electrode gap plays an important role. Ideally, the smaller the gap, the higher the magnitude of $\vec{e}_{THz}(t)$ for a given applied bias $u_{THz}(t)$ or received terahertz power $u_{THz}(t) \sim \sqrt{p_{THz}(t)}$. Therefore, one would be tempted to use the smallest gap possible, given that energy in the signal to be detected is limited, and one cannot just increase the bias as in the emitter case. However, the smaller the gap, the smaller the photocondutive area able to absorb the incoming optical optical power. For this reason, photoconductive mixers used for CW terahertz detection employ an interdigitated electrode structure as the one shown in Fig. 2.9, with, an effective absorbing transverse area equal to $w_l d$, an effective electrode gap l, and a volume $V = w_l dl$. Intuitively, the

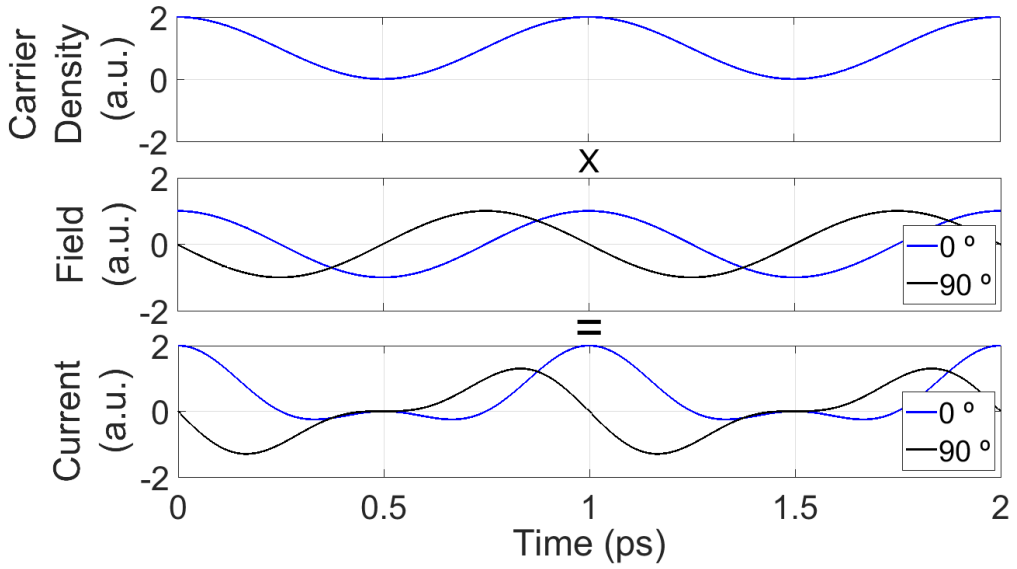

Figure 2.8.: Graphical approximation of the terahertz detection process as a mixing process. Note the difference between the generated current during the mixing process when the biasing field has no phase shift with respect to the instantaneous carrier density, and the one generated when there is 90^{o} phase shift. The generated DC current is unity in the first case, and zero in the second one.

interdigitated structure can be as a collection of N_f electrodes connected in parallel, resulting in an non-negligible capacitive effect, as it will be discussed later.

The geometry of the photoconductive mixer employed to model the CW terahertz detection process shown in Fig. 2.9 is the basis for a more rigorous modelling of its performance. As in the case of terahertz emitters, such modelling will be based on the enforcement of charge continuity equation and energy conservation. The parameters of the photoconductor and those of the lasers will be considered to be same as in the emitter case. Similarly, the spatial power distribution of the laser and its absorption will also be assumed constant.

Two cases will be distinguished: the small signal case and the large signal case. Let me begin with the small signal case, which is the one relevant for the applications shown in this thesis. As explained at the beginning of this Chapter, the charge continuity equation, i.e. Eq. 2.8, allows to determine the electron dynamics and subsequently the optically excited current for constant biasing field. However, for the detection case, the electric field responsible for the transport of electrons is not constant, but the sinusoidal terahertz signal reaching the electrodes of the photoconductor $e_{dt}\cos(\omega_{THz}t + \phi_{dt})$, proportional to the magnitude of $\vec{e}_{THz}(t)$, the field received by antenna incorporated to the mixer. Nevertheless, if the magnitude of the time-varying transport field is small as compared to the other terms higher

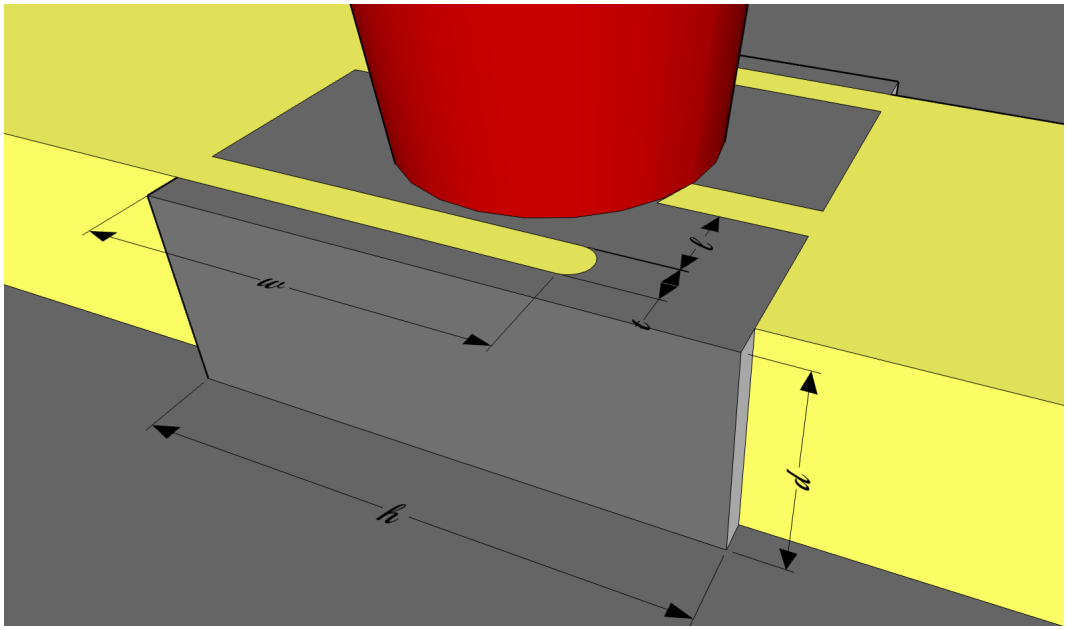

Figure 2.9.: Graphical depiction of the electrode structure of a CW photoconductive mixer employed as a terahertz detector. Note that the total length of the electrode structure w_l can be approximated as $(N_f - 1)(w + t + l)$, N_f being the number of electrodes. For the particular depiction shown here $N_f = 4$.

order effects can be neglected. The charge continuity equation then reduces to short carrier-lifetime case, i.e. Eq. 2.20, resulting in the same electron density $n_{cw}(t)$ given by Eq. 2.21. Thus, the effect of the time-varying biasing field transporting the electrons out of the photoconductor can be simply incorporated using Eqs. 2.6 and 2.7, which relate the drift current density with the biasing field and the electron density. The magnitude of the generated current density $j_{dt}(t)$ when detecting a small terahertz signal is therefore given by

$$j_{dt}(t) = e n_{cw}(t) \mu_{AC} e_{dt} \cos(\omega_{THz} t + \phi_{dt}). \tag{2.46}$$

with

$$\mu_{AC} = \frac{\mu}{\sqrt{1 + (\omega_{THz}\tau_s)^2}} \tag{2.47}$$

τ_s being the effective scattering time of the electrons [69]. The reason for using Eq. 2.47 instead of just using μ is because the applied field is not constant but time varying. However, since most short carrier-lifetime photoconductors exhibit scattering times well into the tens of femtoseconds due to the amount of defects in their crystalline structure, the roll-off due to the scattering time only starts to be significant for very high terahertz frequencies. For example, for τ_s equal to 50 fs,

the value of μ_{AC} is 0.95μ. Since no frequencies higher than 1 THz are considered in the applications or characterizations presented in this thesis, it will be assumed that $\mu \sim \mu_{AC}$. Yet, for longer values of τ_s, like the ones exhibited in some plasmonic photoconductive mixers that utilize long carrier-lifetime photocondutive materials, or for frequencies higher than 1 THz, the frequency-dependent value of μ_{AC} must be taken into account.

Using that approximation, Eq. 2.46 can be written as

$$j_{dt}(t) = en_{cw,0}\mu e_{dt}\left(\cos(\omega_{THz}t + \phi_{dt}) + \frac{1 + \cos(2\omega_{THz}t + 2\phi_{dt})}{2\sqrt{1 + (\omega_{THz}\tau)^2}} \right) \tag{2.48}$$

where $n_{cw,0} = \frac{\tau}{d}\frac{\eta_{eff}}{hf}\frac{E_{CW,0}^2}{Z}$. Note that the phase of the incoming terahertz wave ϕ_{dt} has been assumed to be the same as the phase of the CW optically-excited electron density ϕ_{cw}. In general, this does not need to be the case, as it will be discussed in the last section of this Chapter. However, it must be the case when enforcing energy conservation for the determination of the maximum value of the responsivity, as it will be done here.

With $j_{dt}(t)$ at hand, it is straight-forward to obtain the resulting drift current arising from the detection process $i_{dt}(t)$, i.e.

$$i_{dt}(t) = en_{cw,0}\mu e_{cw}w_l d\left(\cos(\omega_{THz}t + \phi_{cw}) + \frac{1 + \cos(2\omega_{THz}t + 2\phi_{cw})}{2\sqrt{1 + (\omega_{THz}\tau)^2}} \right) \tag{2.49}$$

which can be rewritten as

$$i_{dt}(t) = \frac{u_{dt}}{r_{dt}}\left(\cos(\omega_{THz}t + \phi_{cw}) + \frac{1 + \cos(2\omega_{THz}t + 2\phi_{cw})}{2\sqrt{1 + (\omega_{THz}\tau)^2}} \right) \tag{2.50}$$

with $r_{dt} = \frac{1}{n_{cw,0}e\mu}\frac{l}{w_l d}$ and $u_{dt} = e_{dt}l$. Note that $i_{dt}(t)$ is composed of three modes: one DC mode and two AC modes at frequencies ω_{THz} and $2\omega_{THz}$, respectively. Normally, the DC mode is referred to as the detected current, given that it is the only mode than can be detected using conventional post-detection electronics. The other two modes are usually neglected, however, they play a role in the energy conservation.

The energy conservation equation for this case is obtained by the application of the Poynting theorem for a conducting medium, which is the natural energy conservation equation for EM fields. It states that the time-averaged energy flux of an EM wave entering a conducting medium must be equal to the rate at which the EM wave performs work on the charged particles inside the medium, and also to the rate at which the EM energy is stored capacitively or inductively inside the medium [70]. In this case, the conducting medium is the photoconducutor and the EM wave is the terahertz wave. Hence, the work per cycle required to transport the optically-excited electrons in the photoconductor, and the rate at which the energy is stored in it,

must be equal to the integrated time-averaged energy flux of the terahertz wave reaching the electrode structure covering the photoconductor. Mathematically, this can be expressed as

$$\left\langle \oiint_S \vec{e}_{dt}(t) \times \vec{h}_{dt}(t) \cdot d\vec{S} = -\frac{d}{dt} \iiint_V w_{dt}(t) dV - \iiint_V \vec{e}_{dt}(t) \cdot \vec{j}_{dt}(t) dV \right\rangle_T \tag{2.51}$$

where $\vec{h}_{dt}(t)$ is the magnetic field associated with $\vec{e}_{dt}(t)$, $w_{dt}(t)$ the EM energy stored in the electrode structure, S the surface of the photoconductor.

The negative signs in the right-hand side of Eq. 2.51 just represent the fact that the energy balance must be zero, i.e. that all the terms in the equation should add up to zero. The critical step is rather to determine the values of each of the terms in Eq. 2.51.

To determine the value of first term in the right-hand side of Eq. 2.51, i.e. the amount of average power stored by the photoconductor electrode structure, it will be assumed that the electrode structure can only store energy in the form an electric field due to the capacitve nature of its interdigitated structure. The energy stored in the form of magnetic field will be neglected. Thus, if u_{dt} is the amplitude of the CW voltage reaching the electrode structure and c its capacitance, one has

$$\left\langle \iiint_V w_{dt}(t) dV \right\rangle_T = \frac{u_{dt}^2 \omega_{THz} c}{2}. \tag{2.52}$$

For the last term of the right-hand side of 2.51, i.e. the amount of average power required to transport the electrons in the conduction current, it is easier to calculate its value by rewriting the integral as

$$\left\langle \iiint_V \vec{e}_{dt}(t) \cdot \vec{j}_{dt}(t) dV = \iiint_V \sigma_{dt} e_{dt}^2(t) dV \right\rangle_T \tag{2.53}$$

where σ_{dt} is the optically-excited conductivity of the photoconductor, whose value, for each of the modes, can be directly obtained from Eq. 2.48, resulting in

$$\left\langle \iiint_V \vec{e}_{dt}(t) \cdot \vec{j}_{dt}(t) dV \right\rangle_T = \frac{eVn_{cw,0}\mu e_{dt}^2}{2} + \frac{eVn_{cw,0}\mu e_{dt}^2}{2\sqrt{1+(\omega_{THz}\tau)^2}} + \frac{eVn_{cw,0}\mu e_{dt}^2}{4\sqrt{1+(\omega_{THz}\tau)^2}} \tag{2.54}$$

which can be succinctly written as

$$\left\langle \iiint_V \vec{e}_{dt}(t) \cdot \vec{j}_{dt}(t) dV \right\rangle_T = \frac{u_{dt}^2}{2r_{dt}} + \frac{u_{dt}^2}{2r_{dt}\sqrt{1+(\omega_{THz}\tau)^2}} + \frac{u_{dt}^2}{4r_{dt}\sqrt{1+(\omega_{THz}\tau)^2}}. \tag{2.55}$$

The value of the term on the left-hand side of Eq. 2.51, i.e. the total amount of power going to the electrode structure of the photoconductive mixer, is then

completely determined. However, not all the incoming terahertz power reaches the electrode structure. If one is interested in determining the amount of incident terahertz power that reaches the electrode structure to determine the responsitivty of the photonconductive mixer, it is necessary to determine the relantionship between u_{dt}, the voltage at electrode structure, and u_{THz}, the equivalent voltage of the incoming terahertz wave. This relationship depends on the value of the antenna impedance z_{ant} connected electrode structure, and also on its efficiency to collect terahertz power.

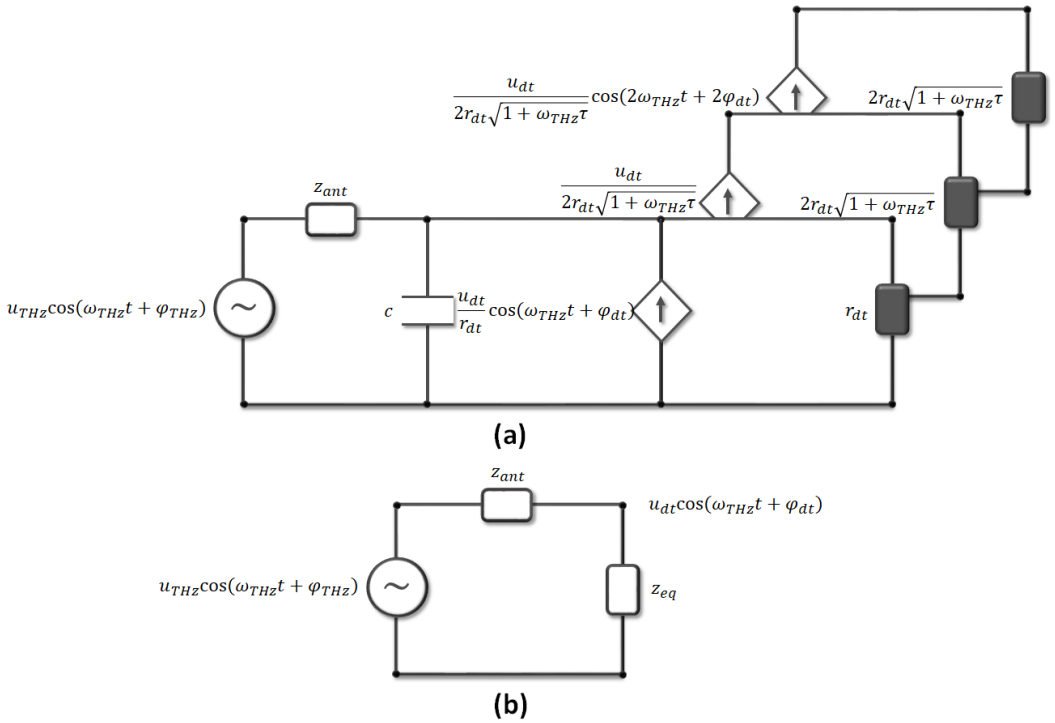

Figure 2.10.: (a) Full equivalent circuit of a photoconductive mixer operating as a CW terahertz detector in the small signal regime. (b) Simplified version (valid only for power conservation purposes).

In order to find such relationship, it is convenient to define the equivalent circuit of a photoconductive mixer operating as a CW terahertz detector. Since there is no proper equivalent circuit for this in the literature, I propose the one of Fig. 2.10 (a). This equivalent circuit is somewhat similar to the one proposed for the pulsed emitter case, except that instead of a DC source providing the power there is now an AC source, and instead of $N-1$ modes there are only three modes. In this circuit, the incoming terahertz wave to be detected is modelled as voltage source with frequency ω_{THz}, and whose amplitude is given by

$$u_{THz} = \sqrt{2\eta_{THz}p_{THz}r_{ant}} \tag{2.56}$$

p_{THz} being the average power of the wave, η_{THz} the antenna coupling efficiency and r_{ant} the real part of its impedance. This is the orthodox treatment used by the antenna engineering community to model receiving antennas [71]. This theoretical treatment gives reasonable results when estimating the power that the antenna delivers to the load connected to it[8], with the caveat that the power given to the load can never surpass 50% of the incoming power [72]. This theoretical treatment, however, does not properly model what happens with the reflected or the scattered power. There has been heated discussions in the literature about this topic [73–77], which still remains unresolved. Nevertheless, since the interest here is only the estimation of the power delivered to the load, i.e. to the electrode structure covering the photoconductor, the orthodox theoretical treatment will still be used.

Please note that the equivalent circuit models each of the optically excited currents as voltage-dependent current sources. The magnitude of their current depends on the amplitude u_{dt} of the AC voltage reaching the electrode structure. The value of their source resistance is the one obtained during the determination of the average power required for their generation.

Using the equivalent circuit of Fig. 2.10 (a), the capacitance of the electrode structure, and the value of the resistances for each of the modes, it is possible to determine the voltage u_{dt} if one knows u_{THz}. To this end, one can consider the total average power p_{dt} that must be consumed by the electrode structure of the photoconductor as a function of u_{dt} by using Eqs. 2.52 and 2.55, resulting in

$$p_{dt} = \frac{u_{dt}^2}{2}\left(\frac{3+\sqrt{1+(\omega_{THz}\tau)^2}+j\omega_{THz}r_{dt}c\sqrt{1+(\omega_{THz}\tau)^2}}{r_{dt}\sqrt{1+(\omega_{THz}\tau)^2}}\right) \tag{2.57}$$

which can be rewritten as

$$p_{dt} = \frac{u_{dt}^2}{2z_{eq}} \tag{2.58}$$

with

$$z_{eq} = \frac{r_{dt}\sqrt{1+(\omega_{THz}\tau)^2}}{3+\sqrt{1+(\omega_{THz}\tau)^2}+j\omega_{THz}r_{dt}c\sqrt{1+(\omega_{THz}\tau)^2}}. \tag{2.59}$$

This implies that, for the purpose of power conservation, the effect of the optically excited modes at the different frequencies, and that of capacitance of the electrode structure, can be represented by an equivalent impedance z_{eq} at the frequency ω_{THz}, as shown by 2.10 (b). Such concept is central to describe the performance of a mixer

[8] For travelling-wave antennas, one can compare the result predicted by the orthodox model to the result obtained by treating the antenna as a transmission line with a characteristic impedance equal to the antenna impedance and terminated in a load. One can then determine the power reflection coefficient to find the power reflected by the load, and thus the power given to the load. A similar result can be found using Fresnel equations, if one assumes that the antenna and the load can be treated as infinitely extended dielectrics. Both approaches render a similar result to the one predicted by the orthodox model for the transmission case.

of any kind, and in fact it is also expressed by Eqs. 2.33, 2.34 and 2.35 in the previous subsection. To my knowledge, it was proposed in the forties by H.C. Torrey in his magnificent book 'Crystal Rectifiers' [78]. However, it has been repeatedly used in all the theoretical treatments that model mixers, for example, in SIS mixers [45] or in varactor-based mixers [79]. Indeed, a comprehensive theoretical treatment would require the definition of an impedance matrix, that would express how the impedance at a given frequency is reflected at any other frequency. For this particular case, it suffices with the value of z_{eq}, which allows to determine the value of u_{dt} given the value of u_{THz} by using the equation of a simple voltage divider

$$u_{dt} = u_{THz}\frac{z_{eq}}{z_{ant} + z_{eq}}. \tag{2.60}$$

The determination of u_{dt} makes possible not only to determine the amount of power reaching the electrode structure, but also the percentage of total terahertz power going to the detected DC mode, i.e. the conversion loss $\Gamma_{dt,0}$, with value

$$\Gamma_{dt,0} = \left| \frac{4\eta_{THz} r_{ant} z_{eq}^2}{r_{dt}\sqrt{1 + (\omega_{THz}\tau)^2}(z_{ant} + z_{eq})^2} \right| \tag{2.61}$$

Finally, using the value of $\Gamma_{dt,0}$ and the previously calculated resistance of the DC mode, it is also possible to determine the DC current $i_{dt,0}$ detected by the post-detection electronics as

$$i_{dt,0} = \sqrt{\frac{p_{THz}\Gamma_{dt,0}}{2r_{dt}\sqrt{1 + (\omega_{THz}\tau)^2}}} \tag{2.62}$$

which allows to derive an expression for the responsivity $g_{dt,0}$, defined as

$$g_{dt,0} = \frac{i_{dt,0}^2}{p_{THz}} = \frac{\Gamma_{dt,0}}{2r_{dt}\sqrt{1 + (\omega_{THz}\tau)^2}}. \tag{2.63}$$

Besides the small-signal operating regime treated so far, photoconductive mixers acting as terahertz detectors can also operate in the large-signal regime, where the biasing electric field does shape the carrier dynamics. The carrier dynamics in this regime is given by solving the full spatially-dependent continuity equation, i.e. Eq. 2.8, consisting of a time-varying drift term $v_d(t)$ determined by $e_{dt}\cos(\omega_{THz}t)$ with $\phi_{dt} = 0$.

The first step to find a simplified analytical solution to the problem is to determine the value that $\nabla\cdot\vec{j}_{dt}(\vec{r},t)$ must have in the differential equation. Using vector calculus identities and assuming that the terahertz field is spatially uniform over the electrode structure, this term can be written as

$$\nabla\cdot\vec{j}(\vec{r},t) = e\mu\nabla n(\vec{r},t)\cdot\vec{e}_{dt}\cos(\omega_{THz}t). \tag{2.64}$$

and the continuity equation turns into

$$\frac{\partial}{\partial t}n(\vec{r},t) = -\frac{1}{\tau}n(\vec{r},t) + \mu\nabla n(\vec{r},t)\cdot\vec{e}_{dt}\cos(\omega_{THz}t) + g_{cw}(\vec{r},t). \tag{2.65}$$

Assuming spatial dependence only on x, one obtains

$$\frac{\partial}{\partial t}n(x,t) = -\frac{1}{\tau}n(x,t) + \mu\frac{\partial}{\partial x}n(x,t)e_{dt}\cos(\omega_{THz}t) + g_{cw}(x,t) \tag{2.66}$$

which is not easy to solve. One possibility is to assume that $n(x,t)$ can be expressed as $n(x)n(t)$, and then use the method of separation of variables to find a solution as a sum of harmonics, implying the emergence of many modes during the detection process. To test this assumption experimentally, a terahertz wave with an angular frequency equal to $2\omega_{THz}$ was made incident on a photoconductive mixer driven by a pair of lasers having a frequency difference equal to ω_{THz}. The result was the detection of a DC current, a fact that would indeed be explained by the emergence of more modes than the ones predicted by the small-signal model. However, the conversion loss for this case was found to be at least one order of magnitude smaller than the one found when both frequencies, i.e. the terahertz frequency and the optical frequency difference, had the same value.

A full model for the large-signal regime is out of the scope of this thesis. It suffices to say that when the terahertz wave to be detected is powerful enough, the carrier dynamics changes, and the small-signal model might not be fully adequate anymore.

2.4. Noise in Short Carrier-Lifetime Photoconductive Mixers

The modelling of noise in photoconductive mixers acting as CW terahertz detectors has been largely neglected by the terahertz research community. The literature is almost non-existent despite their extremely high sensitivity, which can reach the femtowatt level, as it will be demonstrated in Chapter 3, or even quantum level, as suggested in [80]. In the only available resource in the literature about the topic [81], the noise floor in photoconductive mixers is assumed to be set by shot noise when the laser beam incides in an asymmetric manner with respect to the electrodes, and by thermal noise when it incides symmetrically. The latter being the fundamental limit. However, there are two inconsistencies with this view:

1. It assumes the photoconductive mixer is in thermal equilibrium when pumped symmetrically by a pair of lasers having a significant amount of optical power.

2. It does not explain why the noise can be partially cancelled using special electrode structures, as will be demonstrated in Chapter 3.

Therefore, an improved model for noise in short carrier-lifetime photoconductive mixers is proposed in this thesis. In this model, the noise is determined by the fluctuations in the intensity of the lasers used to pump the mixer, and by the

random recombination events of the carriers excited by the lasers. It is the interplay between these two stochastic processes that ultimately sets the detection limit in photoconductors when significant laser intensities are used to pump them.

Given that noise is a stochastic process, it is important to explain the concepts used in its modelling. Here, it will be assumed that the stochastic noise process are ergodic[9]. In such cases, the stochastic process can be modelled using its mean, its variance and its autocorrelation function.

For an ergodic stochastic process $x(t)$ measured over a time T, the mean μ_x is defined as

$$\mu_x = \frac{1}{T}\int_0^T x(t)dt \tag{2.67}$$

the variance σ_x^2 as

$$\sigma_x^2 = \frac{1}{T}\int_0^T \big(x(t) - \mu_x\big)^2 dt \tag{2.68}$$

and the autocorrelation function $R_{xx}(t')$ as

$$R_{xx}(t') = \frac{1}{T}\int_0^T \big(x(t) - \mu_x\big)\big(x(t+t') - \mu_x\big)dt, \tag{2.69}$$

as given in [82]. The autocorrelation, by means of the Wiener-Khinchin theorem [83], allows to determine the power spectral density of the stochastic process $x(t)$, while the variance delivers the magnitude of that density. Note that the autocorrelation of the process evaluated at $t' = 0$ is just the variance, i.e. $R_{xx}(0) = \sigma_x^2$.

For a noise process $n(t)$ with zero mean and zero autocorrelation (except at $t' = 0$), the autocorrelation function is

$$R_{nn}(t') = \sigma_n^2 \delta(t'), \tag{2.70}$$

and from the Wiener-Khinchin theorem [83], it can be implied that the process would have a power spectral density given by σ_n^2. Such is the case of the noise process in a resistor in thermal equilibrium. The problem is then reduced to finding the value of σ_n^2, which can be obtained using the equipartition theorem [84], resulting in

$$S_n(f) = 4kT \tag{2.71}$$

$S_n(f)$ being the noise power spectral density, k the Boltzmann constant and T the temperature of the resistor. The issue of applying this model to a photoconductive mixer becomes evident now: since the photoconductor is not in thermal equilibrium, the temperature is not uniform, and the equipartition theorem cannot be used. In addition to that, if one tries to estimate its temperature using the version of Eq. 2.71 that incorporates the noise current density, one obtains unrealistic values. As an example, take the photoconductive mixer presented in [85], with a resistance of

[9] Well-behaved processes from which the measurement of several samples, is enough to determine its statistical properties.

5.6 kΩ when operated using 26 mW of laser power. For a detection bandwidth of 1.66 Hz, the measured RMS noise current was 10 pA. This would imply a temperature of 6,300 K, assuming that the contributions from the post-detection elections are negligible (which for a well designed system must be the case).

For those reasons, the noise model proposed here is not based on thermal equilibrium arguments, but rather on the random fluctuations in the intensity of the lasers and in the recombination events.

Indeed, the proposed noise model is based on the one used in optical mixers implemented with photodiodes [86]. In those mixers, a strong laser signal with field $E_{LOP}(t)$ is combined with the optical signal to be detected $E_{INP}(t)$ by means of a beam splitter. The combined optical signal is then focused onto a photodiode, which outputs the difference frequency signal when such frequency is within the detection bandwidth of the photodiode. The process can actually be called photomixing, but with the purpose of determining the amplitude and phase of a incoming optical signal, not with the purpose of terahertz generation.

The noise power spectral density in such optical mixers can be divided into two independent components. The first one is usually referred to as excess noise, since it can be suppressed using a balanced detection scheme given that the laser intensity fluctuations are mutually correlated [86]. The second one is usually referred to as the fundamental limit. It is made up of the dark shot noise and the thermal noise [87]. Thus,

$$S_{pd}(f) = 2ei_{pd} + 2e\gamma(f)i_{pd}^2 + 4kT \tag{2.72}$$

$S_{pd}(f)$ being the noise power spectral density in the photodiode, i_{pd} the absolute value of the DC photocurrent, and γ a laser-dependent proportionality constant that relates the square of the mean laser intensity with its fluctuations. The first term in Eq. 2.72 represents the shot noise quantum limit. The second term represents the excess noise, which can be seen as the rectification of the laser intensity fluctuations by the built-in field and/or the applied DC bias in the photodiode. The third term represents the thermal noise.

Since in most applications the intensity of the laser used as local oscillator is relatively high, the value of DC photocurrent also becomes high. Consequently, the excess noise dominates and the thermal component is usually neglected, as it done in [86], resulting in

$$S_{pd}(f) \approx 2ei_{pd} + 2e\gamma(f)i_{pd}^2. \tag{2.73}$$

From Eq. 2.73, it can be inferred that the variance of the absolute laser intensity fluctuations is roughly proportional square of the mean intensity[10]. A fact that has been confirmed experimentally [88–91]. Therefore, one can expect the variance of the total number of excited carriers in a photoconductor to be proportional to the

[10]Note that relative intensity fluctuations (RIN), i.e. the ratio between the variance of the laser intensity fluctuations and the mean laser intensity, remains more or less constant as the laser intensity increases.

square of the mean laser intensity. In principle, there is no built-in field or external DC bias that rectifies such fluctuations in a photoconductive mixer acting as a terahertz detector when no signal is incident on it. However, there is a diffusion current induced by the Gaussian profile of the incident laser beam. The combined effect of this diffusion current and the random recombination events of the carriers composing that current effectively results in an optical rectification mechanism even without geometric asymmetry.

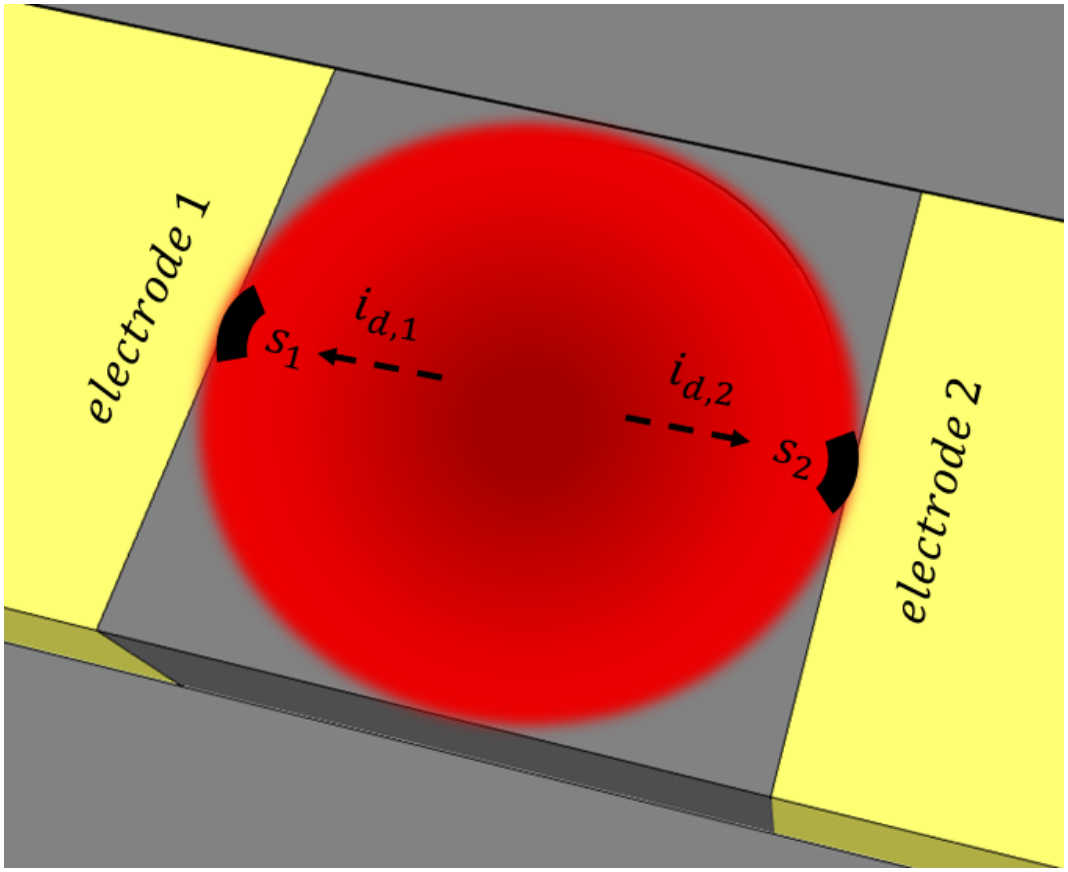

Figure 2.11.: Graphical depiction of the process of pumping a photoconductive mixer using a Gaussian beam showing the direction of the generated diffusion currents $i_{d,1}$ and $i_{d,2}$, and the relevant generation areas s_1 and s_2.

In order to analyze this random rectification process in detail, let me consider the physical process of pumping a photoconductive mixer with a Gaussian laser beam in a simplified symmetric geometry with only two electrodes. Due to the Gaussicity of the beam, a spatial gradient is formed in the photoconductor, resulting in a net diffusion current, as shown in Fig. 2.11. This effect is known as the lateral photo-Dember effect [92], and it has been shown to result in the emission of terahertz pulses when the electrodes of a photoconductive mixer are asymmetrically illuminated by an

ultra-short pulsed laser [93]. It also results in the emission of radially polarized terahertz pulses when a bare photoconductor (with no electrodes) is illuminated by an ultra-short pulsed laser [94].

Clearly, the situation is different in a photoconductive mixer acting as a terahertz detector. If the electrodes of the mixer are illuminated symmetrically by the laser beam, ideally no diffusion current would be collected by the electrodes because the diffusion currents flowing to each of the electrodes ($i_{d,1}$) and ($i_{d,2}$) would be the same, as shown in Fig. 2.11. In other words, the same number of carriers would reach electrode 1 and electrode 2 at all times. However, in a short carrier-lifetime material, recombination or trapping of optically excited carriers would occur randomly before they actually reach the electrode, resulting in a sort of random rectification process.

Noise processes in semiconductors originating from random generation and recombination events have been studied extensively [83, 95, 96], usually using the Langevin equation. However, no lasers were involved in the generation processes for the cases that have been studied. Therefore, thermal equilibrium is always assumed, and consequently, the results obtained in those studies are not applicable for photocondutive mixers acting as terahertz detectors.

Thus, a different treatment to model the noise process in photoconductive mixers pumped by a pair of lasers had to be used. One that is based on compounding the two stochastic processes responsible for the noise: the laser intensity fluctuations and the random recombination of the optically excited carriers. Due to its extremely fast dynamics, it will be assumed that the recombination process determines the dynamics of the autocorrelation function $R_{ll}(t')$ of such noise process $x_l(t)$. In that case

$$R_{ll}(t') = \sigma_l^2 e^{-\frac{|t'|}{\tau}} \tag{2.74}$$

given that the generation events occurring a $t' = 0$ cannot be correlated with the generation events occurring after $t' = \tau$, i.e. after the mean recombination time[11].

Since $R_{ll}(t')$ is an even function, one can use the cosine transform instead of the complex Fourier transform to obtain the noise power spectral density, as dictated by the the Wiener-Khinchin theorem. This results in

$$S_l(f) = \frac{4\tau}{1 + (2\pi f\tau)^2}\sigma_l^2 \tag{2.75}$$

$S_l(f)$ being the noise power spectral density associated with the noise current, which for small detection bandwidths reduces to

$$S_l(f) \approx 4\tau\sigma_l^2. \tag{2.76}$$

[11]The reason for choosing an exponential function to represent such relation is rather heuristic. Indeed, one could chose a rectangular function for the same purpose and the results obtained with it would be very similar for time scales much shorter than τ, which are the ones of interest for the detection process. However, with an exponential function the obtained results are much smoother.

The problem is then reduced to find σ_l^2, i.e. the variance of the current due to laser intensity fluctuations and random recombination events. To this end, one has to resort to the discrete nature of the current.

The starting point are the key assumptions that:

1. The photoconductive mixer is illuminated symmetrically and no external bias is applied to it.

2. The steady state of the photoconductive mixer is determined by the mean intensity of the lasers, i.e. their intensity fluctuations are much smaller than the mean.

3. The carrier lifetime is independent of the laser intensity[12].

4. The electron contributions are much higher than the hole contributions due to their higher diffusion coefficient. Hence, as in the previous subsections, only electrons will be considered.

Under those assumptions, one can consider the extra electrons originating from the laser intensity fluctuations to be transported by the gradient set by the Gaussian profile of the mean laser intensities. A useful analogy of this process is to think of the "noisy" electrons excited by the fluctuations as going down through a slide set by the "noiseless" electrons excited by the mean intensity. The transport velocity v_d must have spatial dependence determined by the specific Gaussian profile of the laser beams, the diffusion coefficients of the electrons, and their carrier lifetime. However, it will be further assumed that due to the short carrier lifetime of the electrons, only the ones generated in the small regions s_1 and s_2 very close to the electrodes really contribute to the measured fluctuations. For those small regions, with length l, usually far away from the strongest variations of the Gaussian spatial distribution, the diffusion velocity can be taken to be constant.

Continuing with the assumption of symmetry, it will be considered that the "noisy" electrons are excited roughly at the same distance from its respective collecting electrode, otherwise one would right away have a steady rectification mechanism. This means that one can group the electrons excited in each of the small regions s_1 and s_2 in pairs.

Once a pair of electrons is excited in the regions s_1 and s_2, it has four possibilities, each one assigned with the same probability:

1. The electron excited in region s_1 recombines, while the electron excited in region s_2 gets collected.

2. The electron excited in region s_2 recombines, while the electron excited in region s_1 gets collected.

[12]This is only true when the photoconductor is not saturated, which is the state in which one would ideally like to operate the mixer.

3. Both electrons recombine before reaching their respective electrode.

4. Both electrons are collected by its respective collecting electrode.

Of the four possibilities, only the first two result in the detection of a net current fluctuation, but the current fluctuations generated in each of those cases have opposite signs. Therefore, one can model the electron pair transport towards the electrodes using the discrete random variable I_d with probability mass function

$$P(I_d = i_d) = \begin{cases} \frac{1}{2} & \text{for } i_d = 0 \\ \frac{1}{4} & \text{for } i_d = \frac{-ev_d}{l} \\ \frac{1}{4} & \text{for } i_d = \frac{ev_d}{l} \end{cases} \tag{2.77}$$

and the total current fluctuations detected in the photoconductor as the compound random variable I_l that results from the sum of $\frac{N_e}{2}$ electron pair transport events

$$I_l = \sum_{n=1}^{N_e/2} I_{d,n}. \tag{2.78}$$

N_e being the random variable representing fluctuations in the number of excited electrons.

Note that Eq. 2.78 is a random sum of discrete random variables. In order to find its mean $E\big[I_l\big]$ and its variance $Var\big[I_l\big]$, one can make use of the formulas derived for these types of discrete random sums in [97], resulting in

$$E\left[\sum_{n=1}^{N_e/2} I_{d,n}\right] = E\big[I_d\big]E\left[\frac{N_e}{2}\right]. \tag{2.79}$$

and in

$$Var\left[\sum_{n=1}^{N_e/2} I_{d,n}\right] = Var\big[I_d\big]E\left[\frac{N_e}{2}\right] + E\big[I_d\big]^2 Var\left[\frac{N_e}{2}\right] \tag{2.80}$$

where $Var[]$ and $E[]$ are the variance and expected value operators, as usually defined for discrete random variables (not to be confused with μ_x and σ_x^2, defined for a continuous-time stochastic process $x(t)$).

The values of $E[I_d]$ and $Var[I_d]$ can be readily obtained from Eq. 2.77, giving as a result

$$E[I_d] = 0 \tag{2.81}$$

and

$$Var[I_d] = \frac{1}{6}\left(\frac{ev_d}{l}\right)^2, \tag{2.82}$$

thus,

$$E\left[\sum_{n=1}^{N_e/2} I_{d,n}\right] = 0 \tag{2.83}$$

and

$$Var\left[\sum_{n=1}^{N_e/2} I_{d,n}\right] = \frac{1}{6}\left(\frac{ev_d}{l}\right)^2 E\left[\frac{N_e}{2}\right]. \tag{2.84}$$

The value of $E\left[\frac{N_e}{2}\right]$ can be obtained by assuming that the optical fields of the lasers used to pump the photocondutive mixer are in a coherent state and not in an squeezed state (as it is always the case for terahertz generation), resulting in N_e having a Poisson distribution [98]. Hence,

$$E[N_e] = Var[N_e] \tag{2.85}$$

and thus

$$E\left[\frac{N_e}{2}\right] = \frac{1}{2}Var\left[N_e\right] \tag{2.86}$$

resulting in

$$Var\left[\sum_{n=1}^{N_e/2} I_{d,n}\right] = \frac{1}{12}\left(\frac{ev_d}{l}\right)^2 Var\left[N_e\right]. \tag{2.87}$$

and since N_e represents the fluctuations in the number of electrons, $Var\left[N_e\right]$ must be proportional to the square of the mean laser intensity, as stated at the beginning.

Therefore, one can state that the variance of the noise current output by photoconductive mixers, when pumped by a total laser power $P_{TOT,CW}$ and with no biasing field applied to it, is proportional to $P^2_{TOT,CW}$, i.e.

$$\sigma_l^2 \sim \frac{1}{12}\left(\frac{ev_d}{l}\right)^2 P^2_{TOT,CW} \tag{2.88}$$

resulting in

$$S_l(f) \approx 4\tau\lambda i_0^2 P^2_{TOT,CW} \tag{2.89}$$

where $i_0 = \frac{1}{\sqrt{12}}\left(\frac{ev_d}{l}\right)$ and λ is a proportionality constant that depends on the specific type of lasers used to pump the mixer. Note that the mean of the noise is still zero.

Eq. 2.89 represents rather a lower bound for the noise associated with terahertz photoconductive detectors. Any geometrical asymmetries would result in additional rectification processes that would produce excess noise, as it occurs in a photodiode.

When such rectification processes are steady, their contribution to the noise floor can be removed, as it will be shown in Chapter 3. However, this excess noise is not shot noise as pointed out in [81], since its power spectral density scales quadratically with $P_{TOT,CW}$ for the reasons explained here. Moreover, thermal noise would also need to be added to fully model the noise process, since it always present.

One of the consequences of the noise model proposed here is the realization of the fact that short carrier-lifetime photoconductive mixers are not thermally limited when acting as terahertz detectors, at least not for the high pumping optical powers required to operate them. Another one is the recognition of the influence that the lasers can have in the detection process with photocondutive mixers.

2.5. Coherent and Non-Coherent Detection in Photoconductive Mixers

So far it has been assumed that during the CW detection process, the terahertz wave to be detected and the optical waves pumping the photoconductive mixer are completely coherent, i.e. that their phases evolve in time in exactly the same way. In general, however, the phase of EM waves does not have a predictable time evolution. It is subjected to random fluctuations, similar to the ones described in the previous subsection. Indeed, the phase can also be modelled as a stochastic process, as it will be done in Chapter 4.

The time evolution of those phase fluctuations is usually modelled by adding a stochastic term to the phase of the EM wave called timing jitter. Depending on the source originating of the EM terahertz wave, the timing jitter can be within the seconds range or within the microseconds range.

2.5.1. Coherent Detection

Even though the phase can fluctuate in the microsecond scale for typical lasers with MHz linewidth, it is still possible to perform phase-resolved terahertz measurements on longer time scales, as the detection process is due to mixing two waves with a relative delay much shorter than microseconds. Such type of measurements will be referred to as coherent measurements in this thesis.

With photoconductive mixers, coherent measurements are performed by using the same set of lasers to simultaneously pump the terahertz emitter and the terahertz detector. This measurement configuration, also known as homodyne, guarantees that the phase of the emitted terahertz signal, and that of the optically-excited electron density acting as local oscillator, fluctuate in exactly the same manner, permitting to disregard the effect of the timing jitter in the detected terahertz signal $i_{dt,0}$, which can be simply expressed as

$$i_{dt,0} \sim e_{THz} \cos(\phi) \tag{2.90}$$

where ϕ does not represent anymore the absolute phase of the emitted terahertz wave but its relative phase difference with respect optically-excited local oscillator at the photocondutive detector. As long as the relative phase difference stays the same, the value of the $i_{dt,0}$ would remain the same if e_{THz} does not change. In this way, it is possible to measure changes in the phase of the the emitted terahertz wave induced by a sample by comparing the value of $i_{dt,0}$ obtained with sample and without a sample. Certainly, this requires the measurement of $i_{dt,0}$ over several frequency points to fully discriminate between periodic variations of the phase and variations in the amplitude of the terahertz signal.

This measurement configuration is used in Chapter 3 to perform the modelling and characterization of ErAs:In(Al)GaAs photoncoductive detectors, given that this configuration prevents that the influence of the phase fluctuations affect the characterization.

2.5.2. Non-Coherent Detection

When the interest is rather on the characterization of the phase fluctuations of a terahertz wave, the laser system pumping the photoconductive mixer acting as terahertz detector must not be mutually coherent with the terahertz wave to be detected. For this reason, this measurement configuration is referred to as non-coherent. In the literature, it is frequently referred to as terahertz heterodyne detection.

Non-coherent terahertz measurement systems based on photocondutive mixers allow the measurement of the absolute timing jitter of an incoming terahertz signal, granted that the timing jitter of the optical local oscillator signal is significantly smaller than that of the incoming terahertz signal, as it will be discussed in Chapter 4. The measurement of the absolute timing jitter can ultimately be used to measure absolute frequency, and this fact can be exploited to perform spectral analysis, as demonstrated in Chapter 5.

3. ErAs:In(Al)GaAs Photoconductive Terahertz Detectors

3.1. Introduction

In this chapter I present a thorough experimental characterization of the responsivity, the NEP and the noise properties of ErAs:In(Al)GaAs photoconductive mixers acting as terahertz detectors. The experimental characterization of the responsivity and the NEP was done using a fully coherent detection scheme during my secondment in TOPTICA Photonics AG, and the results were published in [99]. The experimental characterization was then used to develop a model of the responsivity and the NEP of the mixers using the theory introduced in Chapter 2. The experimental characterization and the developed model set the baseline for the expected performance of the demonstrated applications in the subsequent chapters, and can help to determine the feasibility of future applications.

Section 3.2 starts by describing the state-of-the-art of short carrier-lifetime photoconductive mixers driven by 1.55-μm lasers. Section 3.3 explains in detail the operating principles and the structure of the ErAs:In(Al)GaAs photoconductive mixers as terahertz detectors. Section 3.4 presents the experimental characterization and the simplified theoretical modelling of the ErAs:InGaAs photocondutive mixers operating as fully coherent detectors from 0.1 to 1 THz. Finally, section 3.5 shows the first experimental demonstration of excess noise cancellation in photoconductive mixers.

3.2. State of the Art

Even though there has been a lot of progress in the development photoconductive mixers in recent years, a significant part of it has been done for devices operating with 0.8-μm lasers, given that the material development is much easier for this wavelength. However, such photoconductive mixers are not compatible with the 1.55-μm components developed for the telecom industry. This hinders the development of applications and systems that make use of telecom components, and increases their cost. In fact, many of the applications presented in this thesis would not have been possible without extensive use of all the commercial-off-the-shelf components developed for the telecom industry. Thus, the review of the state-of-the-art will be mostly focused on the developments done for photocondutive mixers operating at telecom wavelengths, with the exception of the plasmonic photoconductive mixers

developed for 0.8-μm operation, which have shown outstanding results that deserve a mention.

As the name implies, the most important characteristic of a short carrier-lifetime photocondutive mixer used as a detector is its carrier lifetime. The carrier lifetime determines how the responsivity rolls off as a function of frequency, as given by Eq. 2.63. However, this is not the only characteristic that matters. The photoconductor must also have a high mobility to allow for an efficient transport of the excited electrons. Moreover, it must show a high ratio between dark and illuminated resistance, otherwise, the dark current and its associated heat generation compromises the thermal endurance of the photoconductor. The latter is very difficult to achieve in photoconductors operating at telecom wavelengths. The main problem is that in order to absorb 1.55-μm laser radiation efficiently, the photocondutive material, usually InGaAs, must have a narrow bandgap. This means that the material is much more conductive in dark conditions, since the intrinsic carrier concentration increases exponentially as the bandgap decreases. It also means that the photoconductive material is much more sensitive to shifts in the Fermi level resulting from the incorporation of dopants or impurities required to achieve a short carrier lifetime.

In particular, the very successful procedure used to fabricate short carrier-lifetime photoconductors operating at 0.8-μm wavelengths based on the low-temperature growth of GaAs for the formation of deep traps [59] [61], does not work for InGaAs. This is because the energetic level of the traps that result from low-temperature growth of InGaAs turns out to be very close to its conduction band, i.e. they are not deep-level traps anymore but shallow traps, which means they can be activated thermally at room temperature. The net effect is a significant n-type doping that results in low ratio between dark and illuminated resistance [60].

Through the years, several solutions have been explored to overcome this problem. One the first ones, was to use low temperature grown (LTG) GaAs as an extrinsic photonductor to absorb 1.55-μm laser radiation [100]. Although the approach worked, it resulted in a lower optical-to-terahertz conversion efficiency, and so far, it has only been demonstrated under pulsed operation. Later, the use of iron-implanted InGaAs was shown to exhibit carrier lifetimes short enough for terahertz detection, and resistances comparable, or even higher, than those of intrinsic InGaAs [101]. The reason for this is that iron defects effectively behave as deep traps, deep acceptors in fact, having an energetic level very close to mid of the InGaAs bandgap. However this approach was not explored or optimized further at that time. Then, the use of beryllium doping, in conjunction with a special LTG-InGaAs stochiometry demonstrated also good results in terms of terahertz detection [102], mainly due to the effective p-type doping effect of beryllium, which pushes the Fermi energy away from the conduction band edge. Another approach was the use of heavy-ion-bombarded InGaAs, which due to the extremely high energy of the ions used for the bombardment did not result in a net incorporation of the ions within the InGaAs crystalline structure, just on the disruption of the crystal lattice [103]. This in turn meant a short carrier lifetime with no effective doping. However, the mobility was severely reduced.

Material	Carrier Lifetime	Mobility	Resistivity	DNR	BW
Homogeneously Be-doped InGaAs:InAlAs [104]	270 fs	517 cm ^{2}/(Vs)	29.7 Ω·cm	90 dB	5 THz
ErAs:InGaAs [105]	380 fs	775 cm^2/(Vs)	290 Ω·cm	91 dB	6 THz
ErAs:InGaAs [106]	380 fs	775 cm^2/(Vs)	290 Ω·cm	101 dB	5 THz
Rh-doped InGaAs [107]	220 fs	1010 cm^2/(Vs)	3189 Ω·cm	105 dB	6.5 THz

Table 3.1.: Comparison between the best 1.55-μm-compatible photoconductive materials for terahertz detection under pulse operation. The displayed terahertz performance is normalized to an average of 1000 measurements. The optical power used to pump the detector was 20 mW for all cases, except for the one in [106], which was pumped with only 15 mW.

At the same time, a more sophisticated approach based on InGaAs superlattices was also tried. Two distinct types of superlattices were proposed: one incorporating ErAs layers as recombination centers and InGaAs as photoconductive layers (ErAs:InGaAs) [108] [109], and one incorporating InAlAs layers as a means to increase resistance and LTG InGaAs as short carrier-lifetime photoconducting layers (InAlAs:InGaAs) [60]. Both approaches were found to exhibit a short carrier lifetime, a relatively high restistance and a decent mobility. Indeed, the approach based on ErAs:InGaAs superlattice was the one ultimately used in the photoconductive mixers presented in this thesis. However, both of the superlattice-based approaches offered more degrees of freedom than any of the other approaches, and this gave them a noticeable advantage when trying to optimize all for the desired characteristics at the same time.

A steady process of optimization then began, which started to incorporate more elements into the superlattices, resulting in a significant improvement of the performance of photoconductive mixers for both terahertz generation and detection. A summary of the best results obtained with both approaches is summarized in Table 3.1. The table also includes the results obtained with a new approach based solely on doping InGaAs with rhodium [107], which also results in deep traps with energetic levels very close to mid of the InGaAs bandgap, as in the case of iron. However, the heavy optimization performed in [107], resulted in a much better performance than the one previously demonstrated in [101].

Given that the developed photoconductive materials are normally tested and benchmarked under pulsed operation, the Table shows the figures of merit for the

Photoconductive Mixer Detector	Integration Time	DNR	Maximum Measured BW
InGaAs:InAlAs Superlattice [51]	0.84 s	117 dB	4 THz
ErAs:InGaAs Superlattice (This thesis)	0.3 s	108 dB	3.8 THz

Table 3.2.: Comparison between the terahertz performance of the two superlattices when used as CW terahertz detectors. The terahertz emitter was a commercial terahertz PIN diode in both cases.

pulsed case. The performance in pulsed operation does not exactly translate to the CW case, however, it is still a very good indicator of CW performance. Indeed, Table 3.2 presents a comparison of the actual terahertz performance of photocondutive mixers acting as CW coherent detectors achieved with each of the two superlattice approaches. Although the comparison serves as a reference, given that it was done under relatively similar conditions, a fair comparison would need to take into account the exact incident terahertz power on the photoconductive mixer, and the post-detection electronics used in each case. Indeed, this is what is done in this Chapter for the case ErAs:InGaAs photoconductive mixers.

In addition to the photoconductive material, the layout of the electrode structure of the mixer itself plays an important role on its performance. Some designs, although pumped by 0.8-μm-wavelength lasers, have shown an outstanding performance as terahertz detectors, and they are worth a mention here. They are based on a high spatial confinement of the incident optical field used to pump the mixer, which allows them to increase the responsivity for a limited amount of optical power, as shown in Fig. 3.1. This approach is usually called plasmonic-enhanced photomixing because the mechanism behind the high spatial optical confinement is the emergence of a surface plasmon wave at the boundary between the photoconductor and the metal electrode structure [110]. Given that the dimensions of the electrode structures required to achieve such performance are in the order of a few hundreds of nanometers, this approach can benefit from the resulting short transport times, allowing the use of long carrier-lifetime materials with higher mobilities and higher quantum efficiencies in some cases [111]. As already mentioned, the implementation of photoconductive mixers as terahertz detectors using this approach has been mostly limited to devices driven by 0.8-μm lasers. For example, in [80] it was suggested that the quantum-level terahertz sensitivity could be achieved by using plasmonic photocononductive mixers pumped at 0.8 μm. The claim was later questioned [112], but it still showed that plasmonic photoconductive mixers could detect radiation of broadband thermal sources in a non-coherent detection scheme. More recently, a DNR of 100 dB and a bandwidth of 6 THz was achieved using only 0.1 mW of laser power at 0.8 μm in pulsed coherent operation [111].

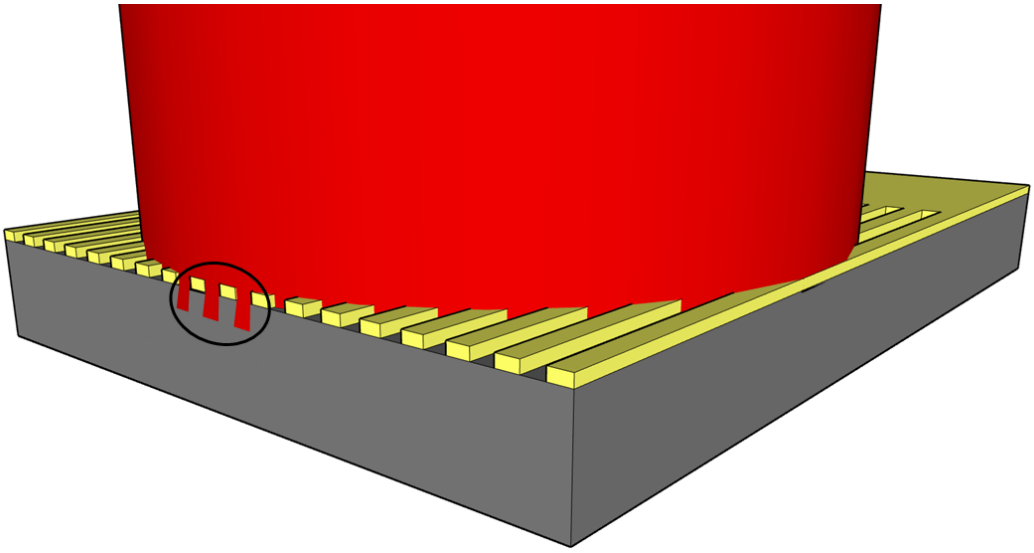

Figure 3.1.: Graphical depiction of a single electrode arm of a plasmonic photoconductive mixer. The size of the electrodes, as well as their periodicity, force the optical field to strongly confine on the small slits, as indicated by the black circle. Note that for the plasmonic effect to occur, the slits must have an optical sub-wavelength size, i.e. they must be around a few hundreds of nm.

The fact that these results were achieved with photoconductive mixers pumped by 0.8-μm lasers certainly has to do with the difficulties of using InGaAs as photoconductor for terahertz detection when pumped by 1.55-μm laser radiation, as explained in [113], where a plasmonic photoconductive mixer pumped by a 1.55-μm pulsed laser was demonstrated. Although the results showed a DNR of 122 dB for an optical pump power of 5 mW and an average of 1000 measurements, the bandwidth was still limited to 3.6 THz. This might be related to the slightly longer duration of the optical pulse used to pump the mixer, or to the spiral antenna attached to the electrodes. In any case, further developments are still required to establish a direct comparison between plasmonic photoconductive detectors and their standard short carrier-lifetime counterparts when both are pumped by 1.55-μm lasers.

3.3. ErAs:In(Al)GaAs Photoconductors as Terahertz Detectors

The core of the photoconductive mixers used throughout this thesis is the ErAs:InGaAs superlattice, used as the photoconductive material. As mentioned in the previous subsection, the inclusion of ErAs layers results in deep traps that act as recombination centers. However, due to their semimetallic nature, the ErAs layers effectively behave as an n-type dopant, shifting up the Fermi level of the overall

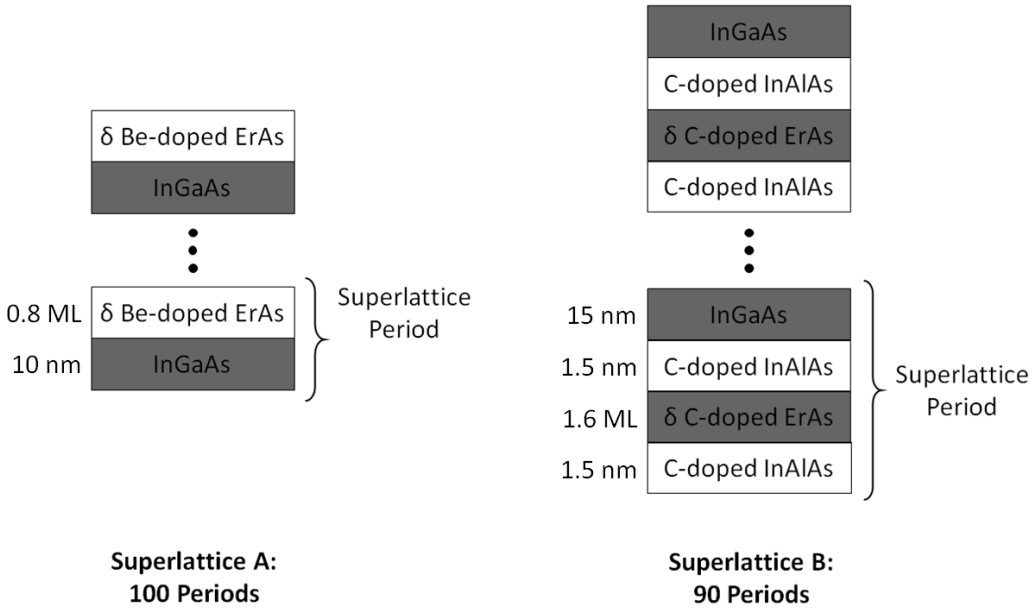

Figure 3.2.: Details of the specific ErAs:In(Al)GaAs superlattice structures used in this thesis.

Superlattice	**Carrier Lifetime**	**Mobility**	**Resistivity**
A	380 fs	2080 $cm^2/(Vs)$	45 Ω·cm
B	2.27 ps	798 $cm^2/(Vs)$	61 Ω·cm

Table 3.3.: Characteristics of the two ErAs:In(Al)GaAs superlattices used in this thesis.

structure, lowering its resistance. To counteract this, the ErAs layers are delta p-doped with either Carbon or Beryllium [114]. The resulting photoconductive material has a short carrier lifetime, a relatively high dark resistance and a high mobility, given that the InGaAs layers are undoped and highly crystalline. If the resistance or the break-down field of the photoconductive material needs to be increased more, as in the case of terahertz emitters, InAlAs layers can be incorporated to structure, resulting in the ErAs:In(Al)GaAs superlattice. However, the inclusion of InAlAs layers also increases the carrier lifetime of the material, since the carriers then have to tunnel through the InAlAs layers to get recombined in the ErAs recombination centers [106].

The details of the specific ErAs:In(Al)GaAs superlattices used as photoconductive materials in the mixers presented in this thesis are shown in Fig. 3.2, and their characteristics in Table 3.3. Their carrier lifetime was obtained using optical pump-probe measurements, while their dark resistivity and mobility was measured using a

$\mathbf{N}_f$	**h**	**w**	**d**	**t**	**l**
4	10 μm	7.5 μm	1.1 μm	1 μm	2 μm

Table 3.4.: Dimensions of the electrode structure. The graphical definition of each of the parameters can be found in subsection 2.3.3.

Hall effect measurement setup [106]. They were grown at the University of California at Santa Barbara by Dr. Justin Norman and Prof. Dr. Hong Lu, while the design of the superlattice structure was devised by Prof. Dr. Sascha Preu. The layout of the mixers is rather standard, having an interdigitated electrode structure with no plasmonic enhancement, and a broadband antenna directly attached to it. The collection of the terahertz radiation is done by means of a 10-mm diameter hyperhemispherical silicon lens with a hyperhemisphericity of 0.95 mm, which is directly attached to the 0.5-mm thick photoconductor substrate.

The mixers were fabricated using contact lithography and metal evaporation with a 0.04-μm layer of titanium, followed by a 0.2-μm layer of gold. The area containing the electrode structure, termed active area, was covered with a 0.60-μm CVD-grown SiN layer that served both as an optical antireflection coating and as a protective layer. More details about the fabrication process can be found in Appendix 1.

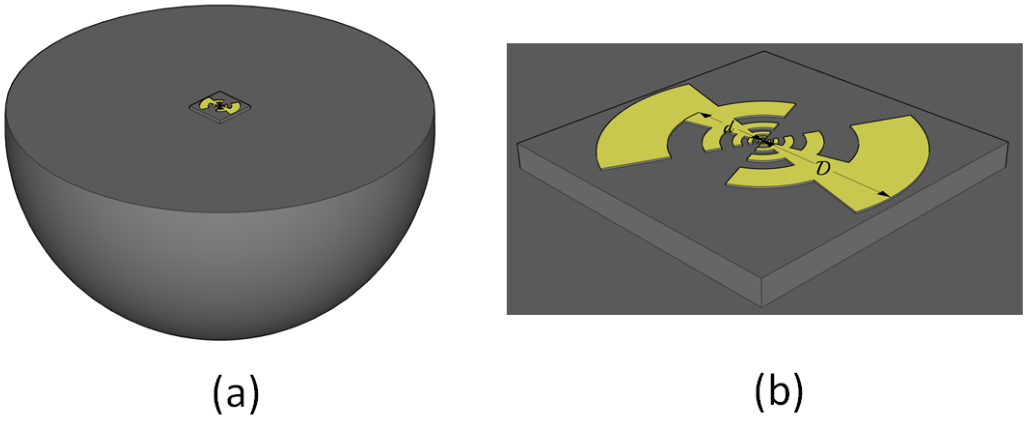

Figure 3.3.: (a) Full view of the photoconductive mixer design used for most experiments in this thesis. (b) Zoomed-in view showing the antenna, composed of 11 resonant arms per side, each one subtending an angle of 45°. The width of each arm is defined by an inner and an outer radius, represented by d and D for the largest arm. The ratio between outer and inner radii is $\sqrt{2}$, while the ratio between consecutive arm radii is 2. The outer radii of the smallest and the largest arms are 10 μm and 355 μm, respectively.

For all of the applications shown in subsequent chapters, the photoconductive material used was superlattice A, while the dimensions of the electrode structure are the ones shown in Table 3.4, in accordance to the definitions of subsection 2.3.3.

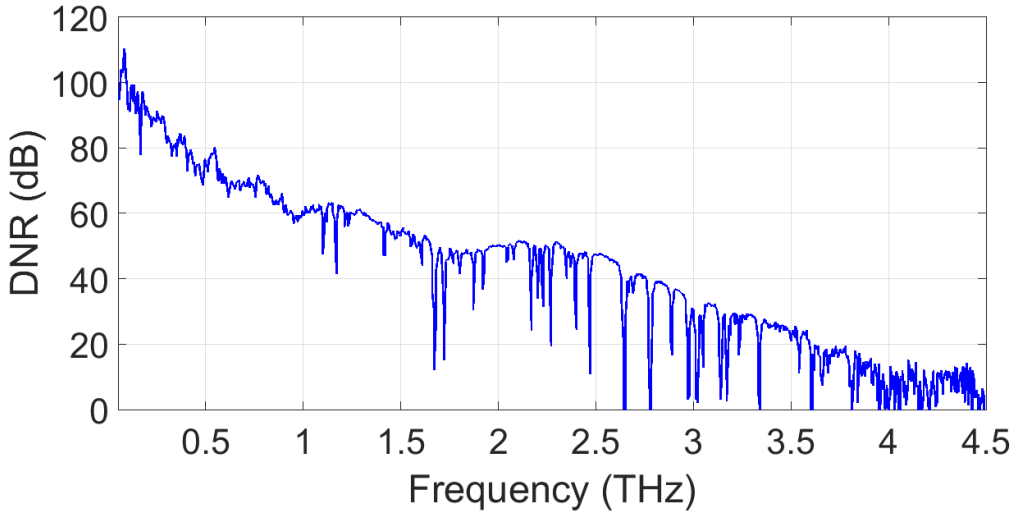

Figure 3.4.: Measured DNR obtained with the photoconductive mixer used for the characterization presented in this Chapter. The measurement was done at the Fraunhofer Heinrich-Hertz Institute using one of their emitters. The integration time was set to 300 ms.

The antenna attached to the electrode structure was either a self-complementary logarithmic periodic design based on the one presented in [115] and illustrated in Fig. 3.3, or a self-complementary logarithmic spiral with a maximum radius of 600 μm. The characterization presented in this Chapter was done for mixers implementing the antenna shown in Fig. 3.3. The only different photocondutive mixer design using superlattice B was the one employed to demonstrate noise reduction.

A graphical depiction of the photoconductive mixer used for the characterization and most of the applications is shown in Fig. 3.3, while a exemplary DNR, measured in cooperation with the Fraunhofer Heinrich-Hertz Institute using a homodyne detection scheme and one of their PIN diodes as an emitter, is shown in Fig. 3.4.

3.4. Characterization of ErAs:InGaAs Photoconductors

The characterization of the responsivity and the NEP of ErAs:InGaAs photoconductive mixers as coherent terahertz detectors was done using the TeraScan laser system and a commercially available terahertz PIN diode, both from TOPTICA photonics. Two mixers, termed A1 and A2, both with the design specified in the previous section, viz. Fig. 3.3, were characterized.

The laser system consisted of two telecom-wavelength DFB lasers with a linewidth of around 2 MHz [116]. The two fiber-coupled laser beams were combined in a 2x2 symmetric fiber-coupler to drive the PIN diode and the ErAs:InGaAs photoconductive mixer simultaneously. For the characerization of mixer A1, the average optical power

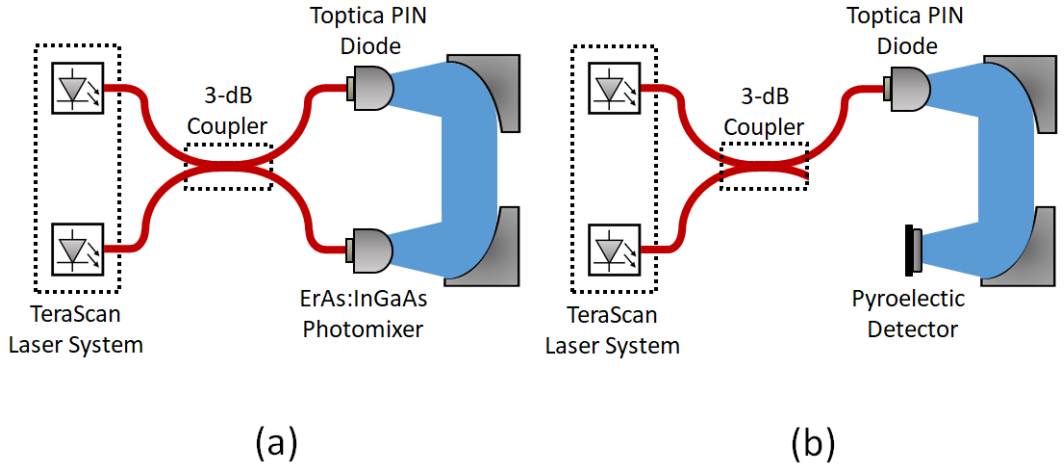

Figure 3.5.: Schematic diagram of the homodyne system used to perform the responsivity and the NEP characterization. (a) Configuration used to measure the detected terahertz current. (b) Configuration used to measure the terahertz power.

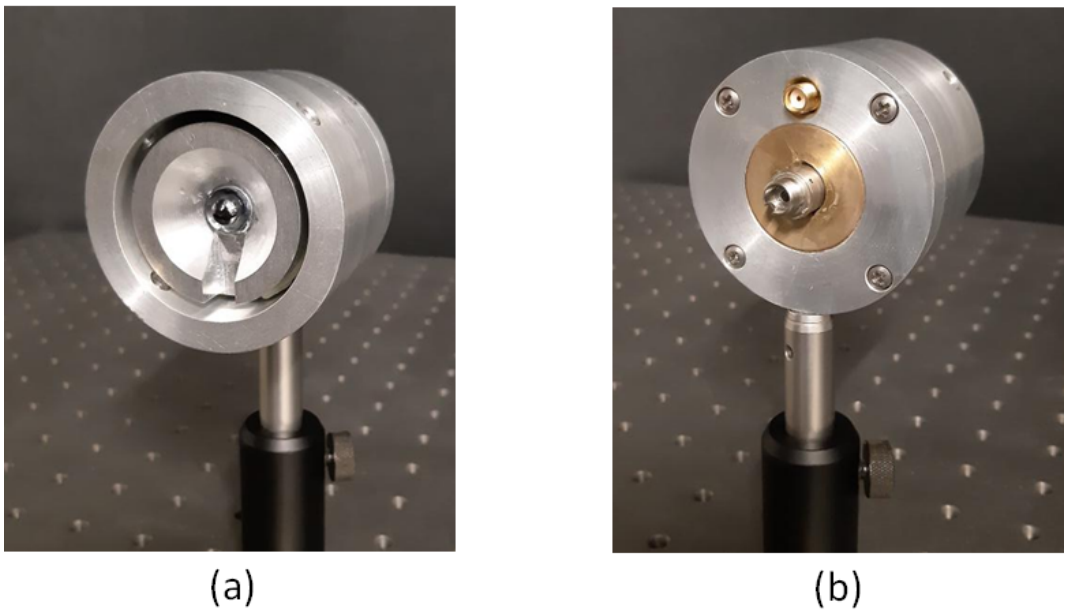

Figure 3.6.: Packaged ErAs:InGaAs photoconductive mixer: (a) front and (b) back.

reaching the PIN diode was 22 ± 0.3 mW, while the one reaching the ErAs:InGaAs photoconductor was 24.7 ± 0.3 mW. For the characerization of mixer A2, the average optical power reaching the PIN diode was 26 ± 0.07 mW, while the one reaching the ErAs:InGaAs photoconductor was 25.3 ± 0.6 mW.

The terahertz beam emitted by the PIN diode, assumed to be Gaussian, was collimated by a first parabolic mirror and then refocused onto the silicon lens of the ErAs:InGaAs photoconductive mixers by a second parabolic mirror. Both parabolic mirrors had a diameter of 508 mm, and focal length of 762 mm. The post-detection electronics employed to amplify and process the detected terahertz current consisted of a PDA-S TIA from TEM Messtechnik set to a gain of 3.33×10^5 V/A, and of the integrated lock-in amplifier in the TeraScan system controlling the lasers. The input of the TIA was directly connected to the ErAs:InGaAs photocondutive mixers through a SMA connector incorporated in a packaging structure specifically developed for this characterization and the subsequent applications. The output of the TIA was in turn connected to the TeraScan lock-in amplifier. A schematic diagram of the whole homodyne system used for the characterizations of both mixers is shown in Fig. 3.5, while a photograph an ErAs:InGaAs photoconductor in a sample package is shown in Fig. 3.6.

Although the characterization of both mixers was done using the same system, each characterization was done at a different point in time, and the system had to be rebuilt each time. Each characterization required the measurement of the emitted terahertz power by a calibrated detector and of current detected by the mixer. For each of the mixer characterizations, the measurement of the detected terahertz current was done immediately after measurement of the terahertz power.

3.4.1. Responsivity Characterization

The current detected by the ErAs:InGaAs photoconductive mixers was recorded using the TeraScan system for the frequency range between 0.1 and 1 THz using an integration time of 300 ms, and a chopping of the PIN diode bias of 1.983 kHz. The AC amplitude of biasing signal was set to 0.8 V, while the DC offset to -0.3 V. The latter ensures that the diode operates in its optimum biasing region. The detected terahertz current is shown in Fig. 3.7. The terahertz power emitted by the PIN diode was measured using a pyroelectric detector calibrated by the National Metrology Institue of Germany (PTB). To this end, the ErAs:InGaAs photoconductive mixers and the PDA-S TIA were replaced by the pyroelectric detector and by its respective calibrated TIA, while the chopping frequency was changed to 15.5 Hz to allow for thermal the relaxation of the pyroelectric detector. The detector was placed slightly tilted in order to reduce reflections within the setup as it was done during its calibration procedure. Everything else in the setup remained the same. The measurements were done overnight at room temperature to keep the measurements conditions as stable as possible. The terahertz power emitted by the PIN diode when characterizing mixer A1 and A2 are shown Fig. 3.8. The measurement of terahertz power and detected current provides an experimental characterization

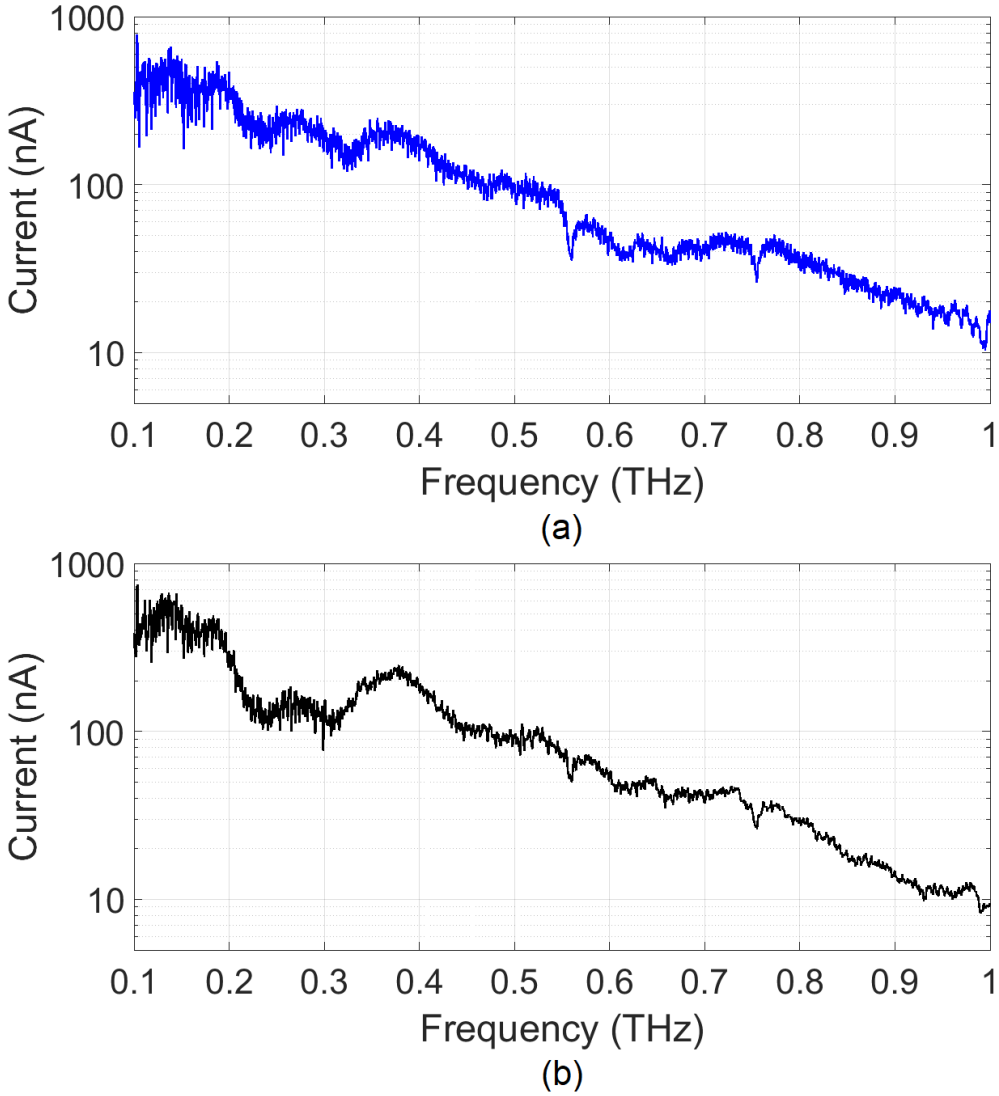

Figure 3.7.: Detected terahertz current with mixer: (a) A1 and (b) A2.

of the responsivity for the range between 0.1 and 1.0 THz. A characterization for higher frequencies was not possible due to the limited sensitivity of the calibrated pyroelectric detector. The theoretical model for the small-signal operating regime presented in section 2.3.3 allows to estimate the responsivity for higher frequencies or even for other ErAs:InGaAs photoconductive mixers, like the ones used in the applications in this thesis.

This estimation requires the determination of the parameters of the model presented

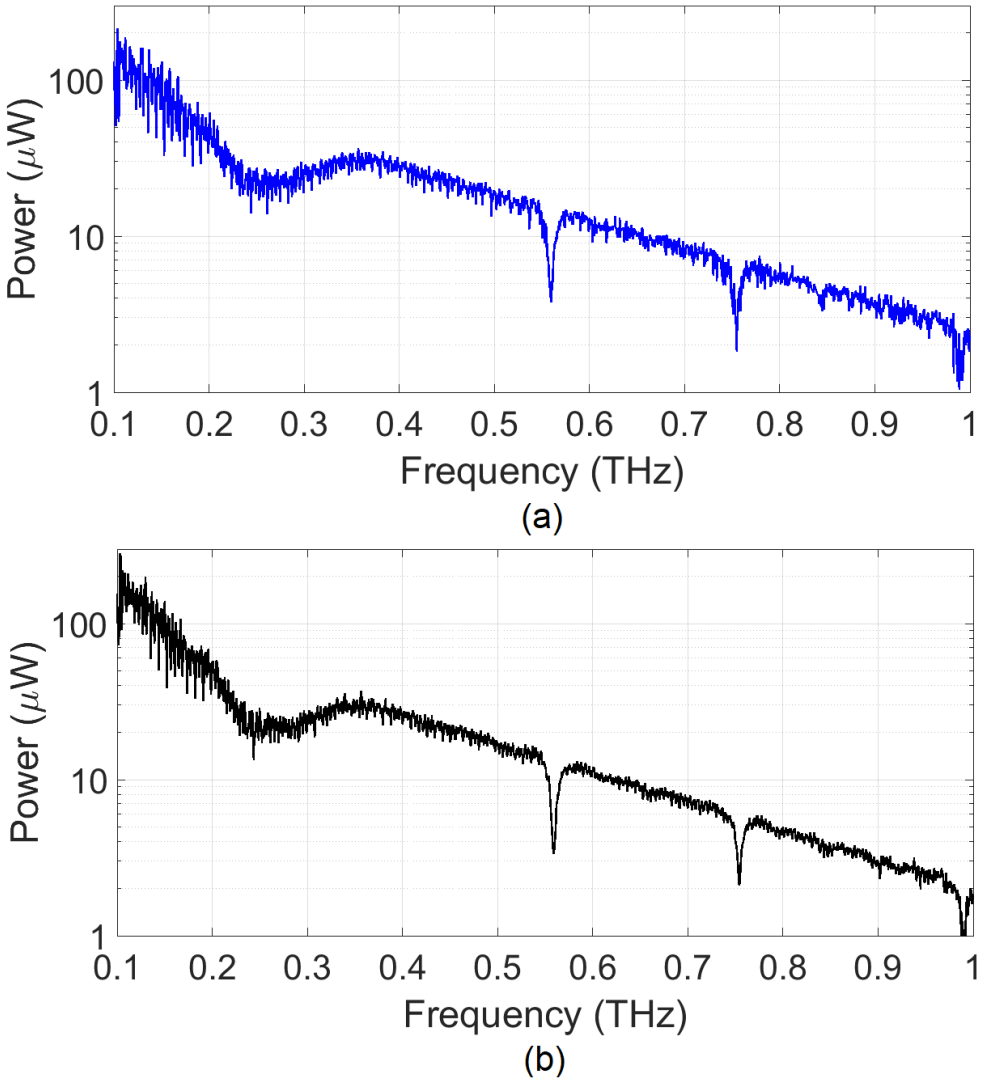

Figure 3.8.: Measured terahertz power impinging on mixer: (a) A1 and (b) A2.

in section 2.3.3, summarized in Table 3.5.

The first parameter is the recombination time τ. As previously stated, its value was determined to be 0.38 fs by means of an optical pump-probe measurement.

The second parameter is the illuminated resistance r_{dt}, which can be obtained from the DC characteristics of the illuminated photoconductor, resulting in a value of 12.8 kΩ for mixer A1, and of 16.6 kΩ for mixer A2. The dark resistance, although not required to model the responsivity, was around 0.5 MΩ for both devices.

The third one is the capacitance c of the interdigitated electrode structure incorporated in the the mixer. This parameter can be obtained using an electrostatic solver

Mixer	τ	r_{dt}	c	η_{THz}
A1	380 fs	12.9 kΩ	4 fF	0.0039
A2	380 fs	16.6 kΩ	4 fF	0.0039

Table 3.5.: Parameters used for the estimate the responsivity and the NEP.

and the geometry and the material properties of the structure, rendering a value of 4 fF. However, since the available electrostatic solver could not simulate lossy dielectric materials, this value does not take into account the influence of the laser on the photoconductive material making up the electrode structure of the mixer.

The fourth one is the coupling efficiency of the antenna and its attached silicon lens η_{THz}, defined as the ratio between the power given to the load, i.e. the photoconductor, and the total terahertz power input to the antenna-silicon-lens system, for which there is no previous experimental values or estimates. Hence, its value was determined experimentally via a fitting. To this end, different values of terahertz power and their associated values of detected terahertz current were recorded at three different frequencies using mixer A1. The selected frequencies for the measurements were 0.15, 0.2 and 0.3 THz. The measurements were done using the same conditions and experimental setup described before, the only parameter that varied was the PIN diode bias. The results are shown in Fig. 3.9.

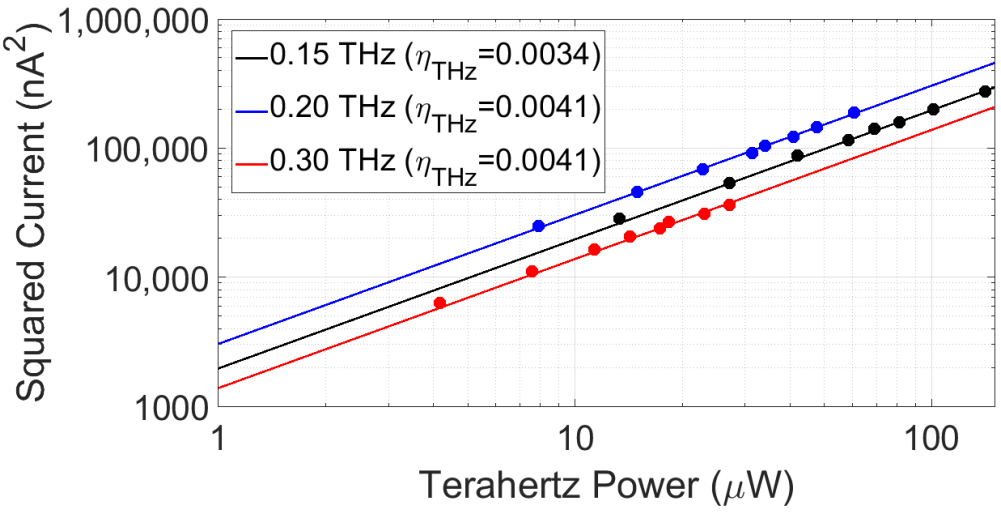

Figure 3.9.: Square of the current detected with mixer A1 versus terahertz power impinging on it for 0.15, 0.2 and 0.3 THz. The points indicate the experimentally obtained values while the lines the values obtained with the fitted η_{THz}.

To determine the value of η_{THz} from the measured data, it is necessary to use the expression for the responsivity $g_{dt,0}$ derived in section 2.3.3, which is defined as the ratio between the square of the detected current $i^2_{dt,0}$ and the incident terahertz power p_{THz}, i.e.

$$g_{dt,0} = \frac{i^2_{dt,0}}{p_{THz}} = \frac{\Gamma_{dt,0}}{2r_{dt}\sqrt{1+(\omega_{THz}\tau)^2}} \tag{3.91}$$

$\Gamma_{dt,0}$ being the conversion loss, $\omega_{THz} = 2\pi f_{THz}$ and f_{THz} the terahertz frequency.

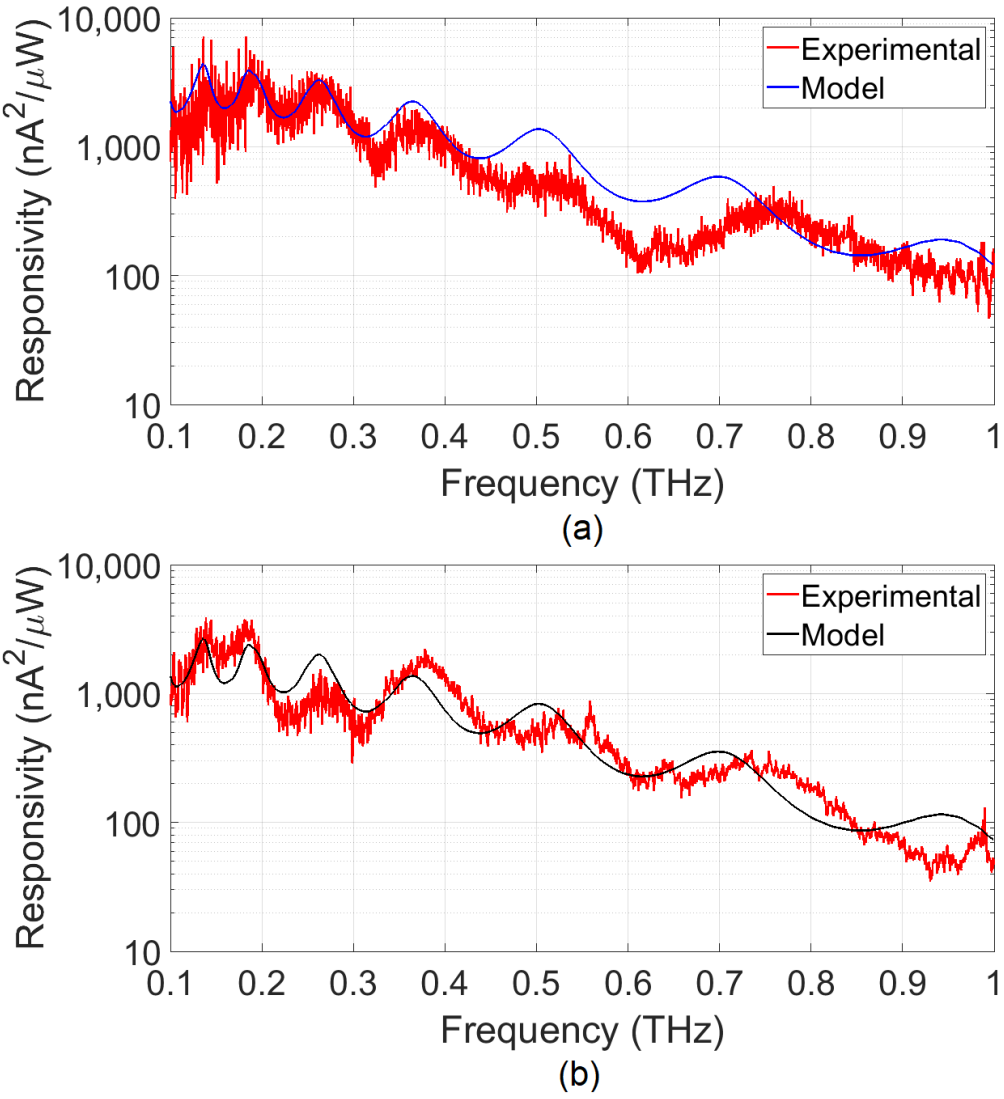

Figure 3.10.: Comparison between the experimentally-obtained responsivity and the one estimated with the model for mixer: (a) A1 and (b) A2.

Using the expression for $\Gamma_{dt,0}$ given by Eq. 2.61 of section 2.3.3, it is possible of write $g_{dt,0}$, as a function of the parameters in Table 3.5, resulting in

$$g_{dt,0} = \left| \frac{4\eta_{THz} r_{ant} z_{eq}^2}{r_{dt}^2 \sqrt{1 + (\omega_{THz}\tau)^2}(z_{ant} + z_{eq})^2} \right| \tag{3.92}$$

$z_{ant} = r_{ant} + jx_{ant}$ being the antenna impedance and

$$z_{eq} = \frac{r_{dt}\sqrt{1 + (\omega_{THz}\tau)^2}}{3 + \sqrt{1 + (\omega_{THz}\tau)^2} + j\omega_{THz} r_{dt} c \sqrt{1 + (\omega_{THz}\tau)^2}} \tag{3.93}$$

as defined in section 2.3.3.

For the determination of η_{THz}, Eq. 3.92 was fitted to the measurements done at 0.15, 0.2 and 0.3 using the parameters of Table 3.5 and the values of z_{ant} obtained with an EM solver for the antenna geometry shown Fig. 3.3. The results of the fitting are also shown in Fig. 3.9. The fitted value of η_{THz} was found to be 0.0034, 0.0041 and 0.0041 for each of the measured frequencies, respectively. This resulted in a average value of 0.0039, which was then used for both mixers. Please note that this value also reflects the effect of all the idealizations made in the estimation of all the other parameters, and does not take into account the directivity of the silicon lens or of the antenna. The skin-depth effect in the thin gold layers has also been neglected. Thus, the value η_{THz} might not be constant over frequency. Still, the values obtained for η_{THz} are quite consistent for a frequency range that spans an octave.

The responsivities predicted by Eq. 3.92, as well as the ones found experimentally for the 0.1-1.0 THz frequency range, are shown in Figure 3.10. There is excellent agreement between the predicted and the experimental responsivity for both mixers, despite the strong dependence on the quasi-optical alignment of the elements in the experimentally obtained values. There is, however, a slight shift in the location of the minima and the maxima in the estimated responsivity. The shift is caused by a non-perfectly captured antenna-photoconductor impedance interplay, e.g. the capacitance is possibly a bit off or the photoconductor might not be placed perfectly in the electrical center of the lens. In any case, the consistency of the responsivity model for both mixers is quite remarkable.

3.4.2. NEP Characterization

The NEP will be defined here as the power of the terahertz wave that produces the same squared current as the mean squared noise current for a measurement bandwidth Δf of 1 Hz.

For a noise process with zero mean, as the one occurring in a photoconducutive mixer, the mean squared noise current is just the variance $\sigma_{i,n}^2$. Hence, using Eq. 3.91, the NEP can be written as

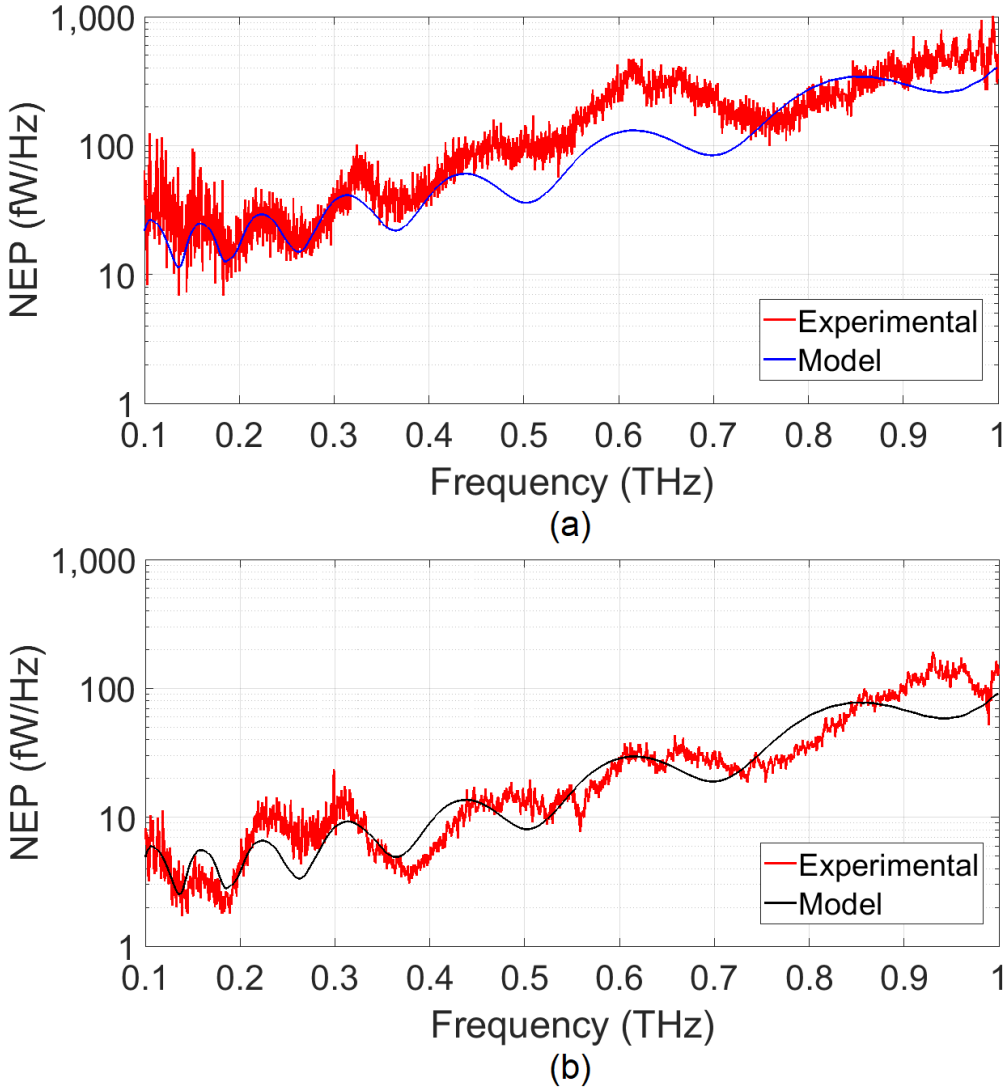

Figure 3.11.: Comparison between the experimentally-obtained NEP and the one estimated with the model for mixer: (a) A1 and (b) A2.

$$NEP = \frac{\sigma_{i,n}^2}{g_{dt,0}} \frac{1}{\Delta f} \tag{3.94}$$

or, using the notation of section 2.4, as

$$NEP = \frac{S_{i,n}}{g_{dt,0}} \tag{3.95}$$

where $S_{i,n}$ is the squared-noise-current spectral density. This is a direct result from

the fact that the noise power spectral density is uniform for the detection bandwidths usually used in photoconductive mixers, as derived in section 2.4. Therefore, once $\sigma_{i,n}^2$ and Δf are known, the NEP can easily be obtained from the responsivity.

For the measurements done here, $\sigma_{i,n}$ was measured to be 9 pA and 3.3 pA for mixer A1 and A2, respectively. According to the lock-in amplifier manufacturer, the integration time of 300 ms corresponded to a Δf of 1.66 Hz. This resulted in a $S_{i,n}$ of 48.8 $\mathrm{pA}^2/\mathrm{Hz}$ and of 6.4 $\mathrm{pA}^2/\mathrm{Hz}$ for mixer A1 and A2, respectively.

Using those values and the previously obtained responsivity model, an estimation of the NEP was calculated for both of the mixers. The estimation is shown Fig. 3.11 together with the experimentally-obtained value. The minimum NEP was found to be 1.8 fW/Hz, attained at 0.188 THz with device A2.

3.5. Excess Noise Reduction in ErAs:In(Al)GaAs Photoconductors

In order to demonstrate excess noise reduction in photocondutive mixers, a dual photocondutive mixer configuration was designed. It consisted of two separate photoconductive elements with two distinct electrode structures, each one connected to a different antenna. Both photoconductive elements were located next to each other, while the antennas attached to them were mirrored with respect to each other, as shown in Fig. 3.12.

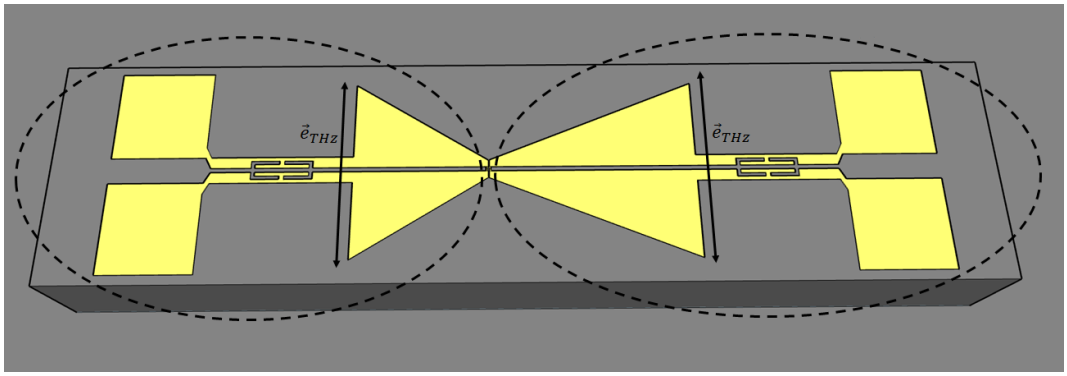

Figure 3.12.: Dual photoconductive mixer design for balanced detection used to demonstrate noise reduction. The dashed ellipses show of the photoconductive mixers composing the design.

The ultimate goal of the design is to perform balanced detection by modifying the phase difference between the terahertz waves arriving at each of the photoconductive elements. This is achieved by changing the point, with respect to the position of the photoconductive elements, at which the terahertz wave is received in each of the two antennas, i.e. the point at which the two antennas become resonant. Since the tapering angle is different in each of them, each antenna will become resonant

N_f	h	w	d	t	l
2	10 μm	6.5 μm	1.6 μm	1 μm	2 μm

Table 3.6.: Dimensions of the electrode structures in the dual photocondutive mixer configuration according to the definitions presented in subsection 2.3.3.

at a different point, resulting in net phase difference between the terahertz waves received by each of the photoconductive elements. Note that although the design resembles a bow-tie antenna, its polarization is orthogonal to the one exhibited by a bow-tie antenna, as indicated in Fig. 3.12.

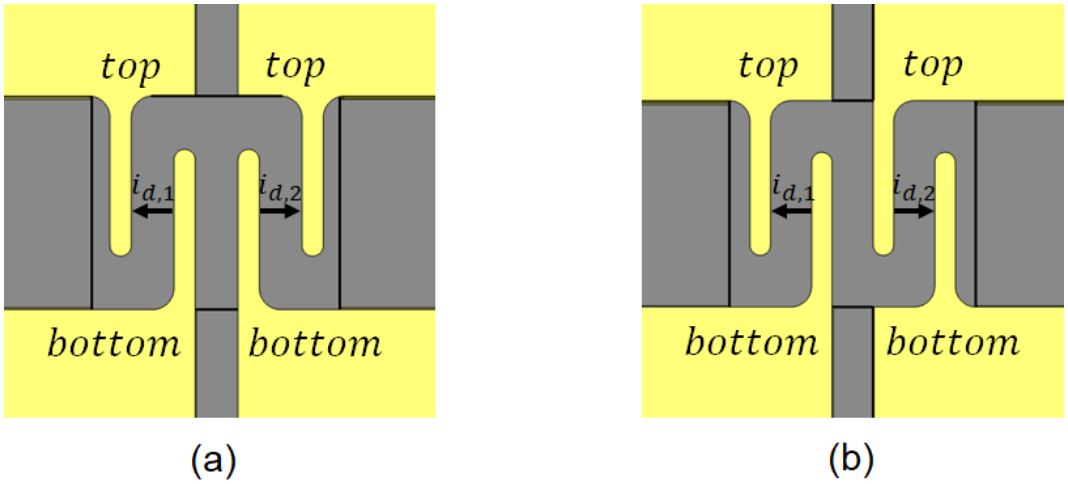

Figure 3.13.: Different types of electrode structures: (a) mirrored and (b) point-symmetric, mounted at the center of the structure shown in Fig. 3.12, right between the two antenna elements. Arrows indicate the direction of diffusion currents responsible for rectification of intensity fluctuations.

By independently modifying the tapering angle of each of the two antennas, it is possible to roughly achieve a 180° phase difference between the waves arriving at each the photoconductive elements for a given frequency range, allowing to perform balanced detection. However, no balanced detection measurements are presented here, only a characterization of the excess noise. In particular, the interest is in determining how significant excess noise is and how much it can be reduced.

As explained in section 2.4, excess noise in photoconductive mixers is the result of a steady rectification process of the laser intensity fluctuations, which arises from an asymmetry in the photocondutor electrode structure. The asymmetry can be caused either by an asymmetric illumination or by the geometry of the electrode structure itself. In the design tested here, the steady rectification process is the result of the dual electrode structure, which results in a net diffusion current in each of the photocondutive elements even when the mixer is illuminated symmetrically, as shown in Fig. 3.13.

Two different types of electrode structures were tested: a mirrored structure, and a point-symmetric one, shown in Fig. 3.13 (a) and (b), respectively. They were fabricated using superlattice B as photoconductive material and with the dimensions shown in Table 3.6, in accordance to the definitions of subsection 2.3.3. The separation between each of the two photoconductive elements was 2 μm.

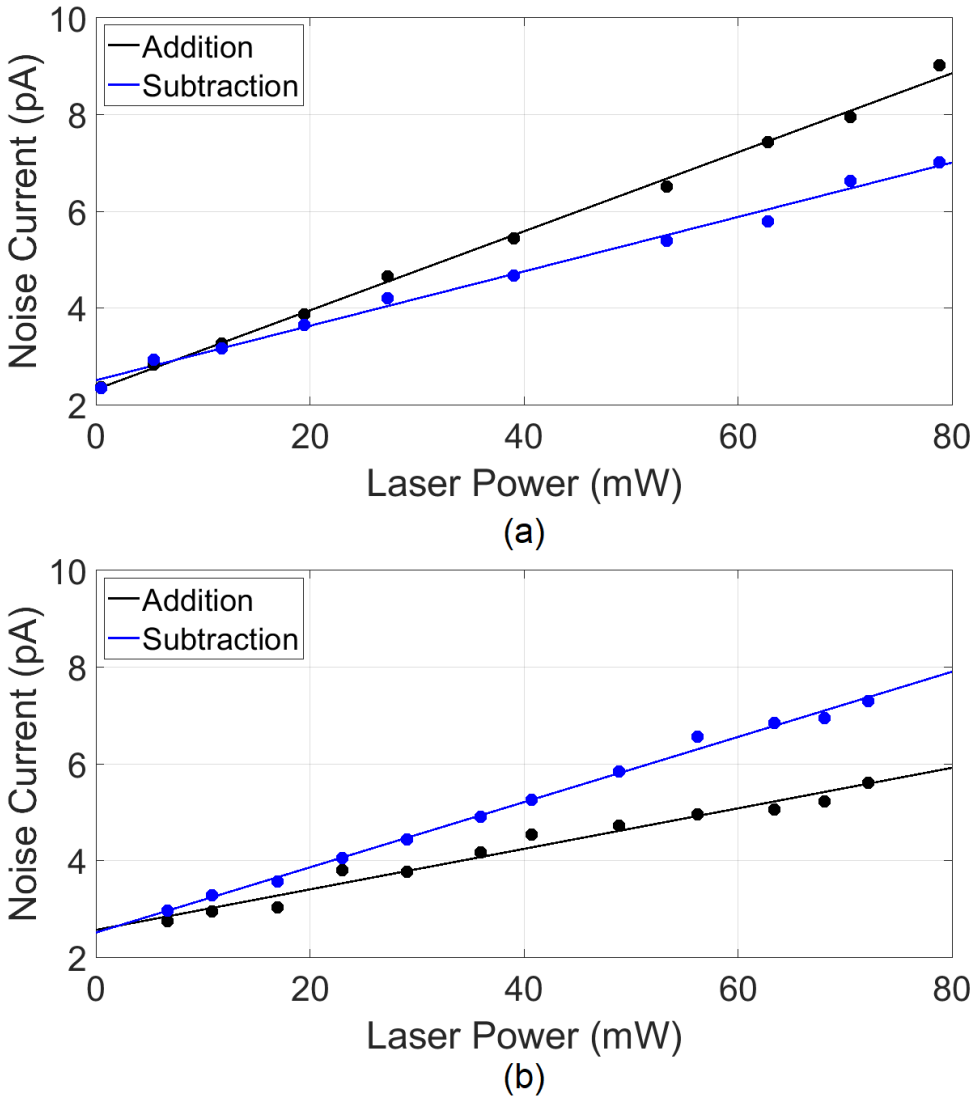

Figure 3.14.: Noise current versus laser power for: (a) mirrored and (b) point-symmetric structure. Points show measured values while lines show fitting.

If both types of electrode structures are connected in the same way to the post-detection electronics, e.g. if ground is always connected to the bottom electrodes in both types of structures, the theory presented in section 2.4 predicts that the steady diffusion currents responsible for the rectification process will flow in opposite directions in the point-symmetric configuration, while they will flow in the same direction in the mirrored configuration. This means that adding the noise currents produced by each of the photocondutive elements in the point-symmetric configuration will result in a reduced noise floor compared to one obtained by the subtraction of the same currents. Conversely, subtracting the noise currents produced by each of the photocondutive elements in the mirrored configuration will result in a reduced noise floor compared to the one obtained by the addition of the same currents. This is indeed the case, as shown in Fig. 3.14.

The sum and difference of the two noise currents of the photoconductive elements in each of the electrode structures were measured simultaneously employing the experimental setup shown in Fig. 3.15.

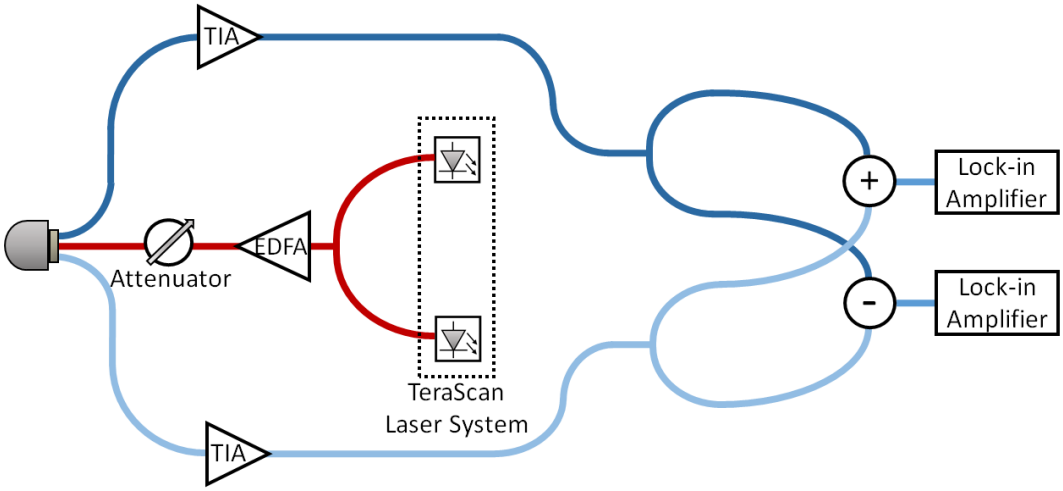

Figure 3.15.: Schematic diagram of the setup used to simultaneously measure the sum and difference of the two noise currents of each of the photoconductive elements.

The measurement was done using two synchronized lock-in amplifiers (MFLI from Zurich Instruments). The incident optical power was provided by an EDFA, which received the two laser signals from the TOPTICA TeraScan system and amplified them to 90 mW for the mirrored structure, and to 80 mW for the point-symmetric structure[1]. The incident optical power was varied using a linear free-space attenuator.

[1]The relatively high amount of laser power was required to compensate for the losses in the attenuator and to compensate for the large waist of the employed optical beam, with an approximate width of 13 μm. Such large waist was required to mitigate the effect of the mechanical drift in the beam incident onto the small photocondutive area of each of the photoconductors during the long times required to complete a whole set of measurements.

A total of 1200 noise samples were recorded for each attenuation step. To be able to record the addition and the subtraction of the noise currents simultaneously, each of the photoconductive elements was connected to a separate TIA with a dual output and a transimpedance gain of 10^6 V/A (PDA-S from TEM Messtechnik). The first output of the first TIA was connected to the first input of an RF power combiner (ZFSC-2-6+ from Minicircuits), while the first output of the second TIA was connected to the first input of an RF 180° power combiner (ZFSCJ-2-2-5 from Minicircuits). Similarly, The second output of the first TIA was connected to the second input of the RF power combiner, while the second output of the second TIA was connected to the second input of the RF 180° power combiner. Then, the outputs of each of the RF combiners were connected to the inputs of each of the lock-in amplifiers. A diagram of the connections is also shown in Fig. 3.15. Please note that the photoconductive elements could not be connected directly to the RF combiners because they had an input impedance of 50 Ω, while the photoconductors featured a very high impedance. Thus, the TIAs, with an output impedance of 50 Ω, did not only serve as amplifiers but also as impedance transformers.

The 1200 samples measured at each attenuation step were then used to obtain the standard deviation of the detected current, i.e. the noise current. The integration time in the lock-in amplifier was set to 10 ms, while the frequency of the TeraScan system to 0.33 THz.

As expected, Fig. 3.14 shows a clear difference between the addition and the subtraction signal for both types of electrode structures, and the difference follows the trend predicted by the theory introduced in section 2.4. Moreover, the difference increases as the laser power increases, indicating the origin of the difference is the laser signal itself. For both structures, the maximum difference is around 2 pA, thus, this is the magnitude of the excess noise. However, this magnitude is expected to be higher for smaller beam waists such as the ones used in the responsivity characterization.

Note that even for the cases in which the excess noise was removed, the noise current still scales linearly with laser power, as predicted by the theory proposed in section 2.4, something that would not not occur if the noise were purely thermal.

3.6. Conclusion and Outlook

In this Chapter, it has been shown that ErAs:InGaAs photocondutive detectors have a performance comparable, or even superior, to state-of-the-art photocondutive detectors pumped by telecom-wavelength lasers. However, in order to establish a rigorous comparison, a thorough characterization of the responsivity and the NEP of state-of-the-art telecom-wavelength photocondutive mixers is still required.

The thorough characterization performed here showed that packaged ErAs:InGaAs photoconductive mixers can have responsivities as high as 7000 $\mathrm{nA}^2/\mu\mathrm{W}$ and NEPs as low as 1.8 fW/Hz when acting as coherent detectors, results that are quite consistent and repeatable, as the measurements demonstrate.

In addition to that, it has been shown that it is possible to estimate the responsivity

and the NEP of photoconductive mixers with reasonable accuracy and robustness using a simple model composed of only a few parameters.

Lastly, it has been shown that noise in photocondutive mixers can be partially suppressed, validating the theory proposed in this thesis that noise in photoconductive mixers does not only have a thermal origin. Indeed, as shown here, the noise current scales linearly with laser power, as predicted by the theory introduced in the previous Chapter.

Further experimental work is still required to thoroughly characterize the performance of ErAs:InGaAs photoconductive mixers as non-coherent detectors, in particular, to determine their noise equivalent temperature. Further measurements are also necessary to determine the terahertz and optical power levels for which the photocondutive mixer still operates in the small-signal regime, as it was assumed in the measurements performed in this chapter. Finally, a through characterization of the noise constants in the proposed noise model is yet to be done, as well as an experimental investigation of the improvement brought by a truly balanced detection scheme.

4. Application 1: Frequency Selective Optoelectronic Downconversion of Pulses

4.1. Introduction

In this chapter, I present the results of the first application demonstrated in this thesis. The one presented here is a new optoelectronic technique for the detection of terahertz pulses that offers a resolution exceeding that of any other available detection technique. I have called it frequency selective optoelectronic downconversion (FreSOD) to emphasize the two aspects that differentiate it from the existing optoelectronic techniques for the detection of terahertz pulses: the domain in which the detection process occurs and its selectivity, which are indeed the two aspects that ultimately give the technique its superior resolution.

The existing optoelectronic techniques for the generation and detection of terahertz pulses always make use of two MLL outputs and two mixers: one for emission and one for reception. The optical pulse of the first MLL output is used for terahertz generation in the emitting mixer, while the second optical output is used for coherent downconversion of the emitted terahertz pulse in the receiving mixer. For the specific case of photocondutive mixers, the downconversion process is the result of the optical excitation of a given amount of carriers in the receiving photoconductor, transformed into a steady DC current by the emitted terahertz field. Due the coherence between the optically excited carriers and the emitted terahertz pulse, the value of the DC current depends on the phase difference between them. In order to resolve the temporal structure of the terahertz pulse, the time delay between the two outputs of the MLL has to be varied, like in an interferometer. Usually, a mechanical delay stage is used to imprint the delay between the two optical pulses. Thus, after each movement of the stage, the DC current in the receiving mixer is recorded, and when enough steps have been recorded, an FFT is performed on the data to transform it from the time domain to the frequency domain. This is why this technique is called time-domain spectroscopy (TDS). Clearly, the resolution depends on the length of the recorded time trace and on the number steps taken. Therefore, for a very high frequency resolution one needs to record a very long time trace with enough data points. This means that high-resolution terahertz measurements using this technique take a considerable amount of time, and normally, by the time the measurement has finished, the optical pulses output by the MLL have already drifted in frequency quite significantly and noise has been added to the process. For this reason, the

highest resolution achieved using this detection technique is in the order of several tens of MHz [117].

A variation of this technique involves using two separate but synchronized MLLs with slightly different repetition rates: the output of the first MLL is sent the emitting mixer, while the output of the second one to the receiving mixer. The slight change in repetition rate effectively results in a time delay between the two optical pulses arriving at each of the mixers, allowing to spare the mechanical delay stage in the detection process. The result is a faster acquisition speed with a high resolution. However, the maximum frequency resolution is still limited by the stability of repetition rate difference during the time it takes to complete a whole measurement, since a complete time trace with enough points still has to be acquired to perform an FFT. This has restricted the resolution of this technique, known as asynchronous optical sampling (ASOPS), to a resolution not better than 82.6 MHz, but with an acquisition times of 10 s [118]. Slightly lower resolutions but with faster acquisition speeds have also been achieved with another variation of the technique known as electronically controlled optical sampling (ECOPS), where the repetition rate difference of the two separate MLLs is not kept constant but varied in electronically controlled steps [119].

As it will be evident throughout this Chapter, the detection technique introduced here allows to achieve a much higher frequency resolution by performing the detection directly in the frequency domain in a non-coherent fashion. Such features are not only relevant for terahertz measurements, but also for the study of the phase noise characteristics of the MLLs driving the photocondutive mixers, a topic that has not been thoroughly studied precisely due to the lack of experimental tools [120, 121].

This novel technique is demonstrated through two exemplary measurements, each one targeting a different application. Some of these measurements were done in cooperation with the Sensors and Instrumentation Techniques Group from Universidad Carlos III de Madrid. The results were published in [122], and many of them are reused here, in particular Figs. 4.5-4.14. Here, however, I present a more complete theoretical analysis of the results published in [122]. Section 4.2 presents the fundamentals of the FreSOD detection technique making extensive use of the theory presented in Chapter 2. Section 4.3 introduces the specific type of MLL and pulsed photoconductive mixer employed for the demonstrated measurements, and it shows an estimation of the power spectral distribution of the measured terahertz pulse. Section 4.4 shows the experimental demonstration of FreSOD with two different applications. The first one is the high-resolution characterization of the amplitude response of a terahertz filter in the 0.070-0.080 THz range. The second one is the phase noise analysis of two of the individual modes composing the measured terahertz pulse, one located at 0.075 THz and one located at 0.340 THz. Finally, section 4.5 gives some concluding remarks and discusses how the technique can be developed further.

4.2. The Frequency Selective Optoelectronic Downconversion Process

As explained in section 2.3.2, the optically excited current giving rise to the emission of a terahertz pulse in a phtoconductive mixer driven by a MLL can be represented as the sum of N current modes, N being the number modes composing the MLL pulse. The frequency separation between any two consecutive modes is given by the repetition rate of the MLL Δf. Hence, the emitted terahertz pulse exhibits a discrete spectrum. Since most MLLs used in TDS systems have values of Δf that range between several tens of MHz and a few hundreds of MHz, it is de facto impossible to observe their discrete nature with resolutions offered by the usual time-domain detection techniques. For this reason, terahertz pulses are normally modelled using a continuum spectrum in the existing literature.

The key to understand FreSOD as a detection technique is to consider the truly discrete spectral structure of the terahertz pulsed emitted in a TDS system.

Using the theoretical model of section 2.3.2, the magnitude of emitted terahertz field in a given direction can be expressed as

$$e_{pl,tot} = \sum_{n=1}^{N-1} e_{pl,n} \cos(\omega_n t + \phi_{pl,n}(t)) \tag{4.96}$$

where $e_{pl,n}$ is the field amplitude of mode n and $\phi_{pl,n}(t)$ its respective phase, which can be written as

$$\phi_{pl,n}(t) = \phi_{PL,n}(t) + \phi_n. \tag{4.97}$$

ϕ_n being the constant phase added to mode n by the effect of the short carrier lifetime, and $\phi_{PL,n}(t)$ its timing jitter. So far, the timing jitter had not been taken into account given that it plays no role in coherent systems, as explained in section 2.5. However, for non-coherent detection schemes such as FreSOD, it must be taken into account. In fact, for the specific case of a terahertz pulse generated by a MLL, the timing jitter of a given terahertz mode n is a direct indication of the degree of coherence between any two MLL modes having separation of $n\Delta f$.

If one uses a CW photocondutive detector driven by a pair of CW lasers with the appropriate frequency, one can selectively detect any of the modes composing the terahertz pulse. However, the average terahertz power in the mode to be measured must be higher than the product between the photocondutive detector NEP and the measurement bandwidth. As it was shown in the previous chapter, the NEP of a fully-packaged ErAs:InGaAs photoconductive detector is in the fW/Hz level, and as it will be shown in the next subsection, the average power of the first few thousands of modes of the terahertz pulses emitted by ErAs:In(Al)GaAs photoconductors is well above the fW level. Hence, the main requirement is fulfilled.

In order to analyze the FreSOD detection process in detail, it is necessary to use the theory introduced in section 2.3.2, which models the performance of CW photoconductive detectors. It will be assumed that the power of the terahertz pulse

to be detected is small enough to operate in the small-signal regime. Hence, one can model the detection process by assuming that $e_{pl,tot}(t)$ will only modulate the transport of the CW excited electrons to give rise to a steady current density, as given by Eq. 2.46. The magnitude of such current density j_{dt} can be expressed as

$$j_{dt}(t) = en_{cw}\left(1 + \frac{\cos(\omega_{cw}t + \phi_{cw}(t))}{\sqrt{1+\omega_{cw}\tau_{cw}}}\right)\mu e_{pl,tot}(t) \tag{4.98}$$

where n_{cw} is the optically excited DC electron density in the CW photoconductive detector, τ_{cw} its carrier lifetime, μ_{cw} its mobility, and ω_{cw} the angular frequency difference between the two lasers pumping the detector. The term $\phi_{cw}(t)$ is the timing jitter of the CW electron density acting as photonic local oscillator, added to incorporate the effect of phase noise in the detection process due to its non-coherent nature. Its value can be written as the sum of the timing jitter due to the finite linewidth of the laser signals $\phi_{CW}(t)$ and the constant phase added by the effect of the short carrier lifetime $\phi_{\tau,cw}$, i.e.

$$\phi_{cw}(t) = \phi_{CW}(t) + \phi_{\tau,cw}\ . \tag{4.99}$$

In principle, j_{dt} will consist of three sets of terms: the single frequency terms, the difference-frequency terms, and the sum-frequency terms, i.e.

$$j_{dt}(t) \sim \sum_{n=1}^{N-1} e_{pl,n}\cos\left(\omega_n t + \phi_{pl,n}(t)\right) + \sum_{n=1}^{N-1} e_{pl,n}\cos\left((\omega_n - \omega_{cw})t + \phi_{pl,n}(t) - \phi_{cw}(t)\right) + \sum_{n=1}^{N-1} e_{pl,n}\cos\left((\omega_n + \omega_{cw})t + \phi_{pl,n}(t) + \phi_{cw}(t)\right) \tag{4.100}$$

however, most of the terms of Eq. 4.100 will be located outside the usual detection bandwidth of the post-detection electronics, mostly determined by the TIA immediately connected after the CW photoconductor. Since most TIAs have bandwidth $\Delta\omega_{dt}$ that ranges between a few tens of kHz and few hundreds of MHz, only when

$$\Delta\omega_{dt} > |\omega_{cw} - \omega_n| \tag{4.101}$$

it is possible to detect a terahertz current. Therefore, the choice of ω_{cw} determines the mode that is selectively detected.

The detected current i_{dt} can then be expressed as

$$i_{dt}(t) \sim e_{pl,n}\cos\left((\omega_n - \omega_{cw})t + \phi_{dt}(t)\right) \tag{4.102}$$

where $\phi_{dt}(t) = \phi_{pl,n}(t) - \phi_{cw}(t)$ is the total timing jitter in the detected signal. As discussed in section 2.5, the timing jitter can be modelled as a stochastic process, much like the noise in a photoconductive mixer. However, unlike the noise in a photocondutive mixer, the long-term mean and the long-term variance of the timing jitter do not converge, i.e. the process is not ergodic. Therefore, one has to use

its short-term versions, in particular, the short-term variance σ_s^2 and short-term standard deviation σ_s, with the definition of short-term depending on the signal to be measured[1].

In the most general case, one can write $\sigma_s\big(\phi_{dt}(t)\big)$ as

$$\sigma_s\big(\phi_{dt}(t)\big) = \sqrt{\sigma_s^2\big(\phi_{cw}(t)\big) + \sigma_s^2\big(\phi_{pl,n}(t)\big)}, \tag{4.103}$$

however, if $\sigma_s^2\big(\phi_{cw}(t)\big) \ll \sigma_s^2\big(\phi_{pl,n}(t)\big)$ then $\sigma_s\big(\phi_{dt}(t)\big)$ becomes almost entirely defined by $\sigma_s^2\big(\phi_{pl,n}(t)\big)$. In that case, $\sigma_s\big(\phi_{dt}(t)\big)$ can be used to characterize the timing jitter of the selected mode of the terahertz pulse. Alternatively, when $\sigma_s\big(\phi_{cw}(t)\big)$ is comparable or even higher than $\sigma_s\big(\phi_{pl,n}(t)\big)$, the jitter in $i_{dt}(t)$ will still allow to infer the peak value $e_{pl,n}(t)$, enabling the technique to still perform measurements with a resolution of f_{rep}, i.e. the repetition rate of the MLL. In fact, an approach exploiting this last feature has already been demonstrated, but using an all-electronic detection scheme [123].

4.3. Spectral Characteristics of Downconverted Terahertz Pulses

A necessary condition for this detection technique to work is that the average power in each of the terahertz modes to be detected must be higher than the product between the photocondutive detector NEP and the employed detection bandwidth. Hence, an estimation of the terahertz power spectral distribution in the pulse to be measured is essential to determine the possible operating range and the limits of FreSOD as a detection technique.

Such estimation can be obtained using the model introduced in section 2.3.2, but first, it is necessary to determine the parameters required by the model. They can be divided into three categories: the ones related to the MLL, the ones related to the pulsed photoconductor, and the ones related to the antenna attached to the photoconductor.

The MLL used to drive the pulsed photocondutive mixer was a passively-locked fiber laser from Menlo Systems. Its output optical pulse had a relatively flat spectrum, an average power of 42 mW, a mode spacing close to 100 MHz, a duration of less than 90 fs (as measured by an interferometric autocorrelator), and a center wavelength of 1560 nm. This corresponds to a bandwidth of least 8.32 THz, using the relationship between measured interferometric duration and actual intensity duration [62]. Therefore, the MLL parameters Δf, N and $N\Delta f$ were set to 100 MHz, 83200 and 8.32 THz, respectively.

The photoconductor used as pulsed emitter was an ErAs:In(Al)GaAs superlattice with the antenna design and electrode structure shown in Fig. 4.1. The design, fabrication and characterization of the antenna and of the electrode structure were

[1] It is also possible to measure the long-term statistics, but one needs to use the Allan variance instead. However, such measurements are out of the scope of this thesis.

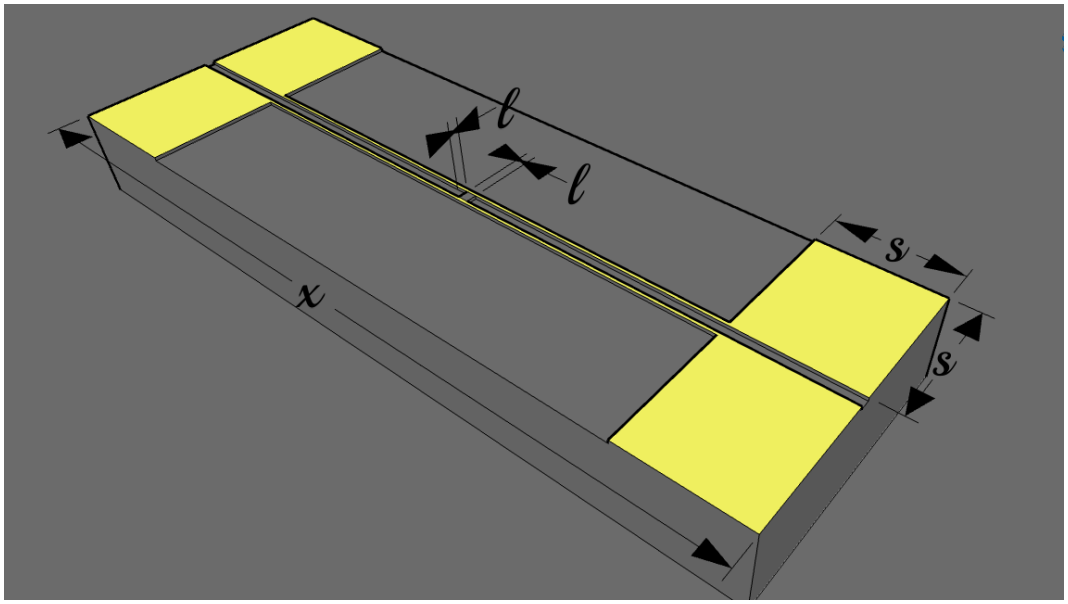

Figure 4.1.: Graphical depiction of the ErAs:In(Al)GaAs photoconductor and its attached antenna.

done by Dr. Uttam Nandi, a former member of the Terahertz Devices and Systems Group of the TU Darmstadt. The superlattice structure was designed by Prof. Dr. Sascha Preu and grown by Dr. Justin Norman at the University of California in Santa Barbara. The specific details of the design and its characteristics can be found in [105, 106], the relevant parameter for the estimation is the carrier lifetime τ, which was measured to be around 2.5 ps. The photoconductor was operated using a bias u_{bias} = 200 V. The illuminated DC current was 240 μA, while the dark current was 8 μA. Therefore, the optically excited DC current in the photoconductor $i_{pl,0}$ was 232 μA.

The dimensions of the antenna attached to the mixer were s = 350 μm, x = 2300 μm and l = 35 μm. Due to the extremely broad frequency range spanned by the terahertz pulse, the calculation of its impedance had to be split into three different ranges:

1. From 100 MHz to 5 GHz: In this range the effective wavelength of the emitted terahertz pulse is much larger than the size of elements composing the antenna. Hence, the antenna can be considered as a short dipole, and its behaviour can be well approximated by the well-known formulas for the impedance of Hertzian dipoles.

2. From 5 GHz to 2 THz: In this region, the effective wavelength of the emitted terahertz pulse is comparable to the size of the elements composing the antenna, but not to the size of the photoconductor. Hence, a full-wave EM solver incorporating a discrete port between the antenna electrodes was used to determine the antenna impedance.

Δf	N	τ	u_{bias}	$i_{pl,0}$
100 MHz	83200	2.5 ps	200 V	232 μA

Table 4.1.: Parameters used for estimation of terahertz power distribution.

3. Above 2 THz: In this region, the effective wavelength of the emitted terahertz pulse is comparable to the photoconductor size. Hence, a full-wave electromagnetic simulation using a discrete port between the antenna electrodes renders inaccurate results. Instead, a waveguide port must be used, and this results in a plethora of possible excitation modes. Moreover, a significant portion of the terahertz waves might be radiated before reaching the antenna at these wavelengths. In order to get a reasonable approximation, it was assumed that the waves that do reach the antenna were radiated by the leaky-wave behaviour of the coplanar striplines making up most of the antenna structure [124, 125]. Therefore, only the results of the mode that produced such behaviour were considered in this antenna impedance calculation. This implies that the terahertz waves radiated before reaching the electrode structure, i.e. when the photoconductor itself is acting as a Hertzian dipole, are not considered in this calculation. In any case, the radiation resistance of such Hertzian dipoles is very small.

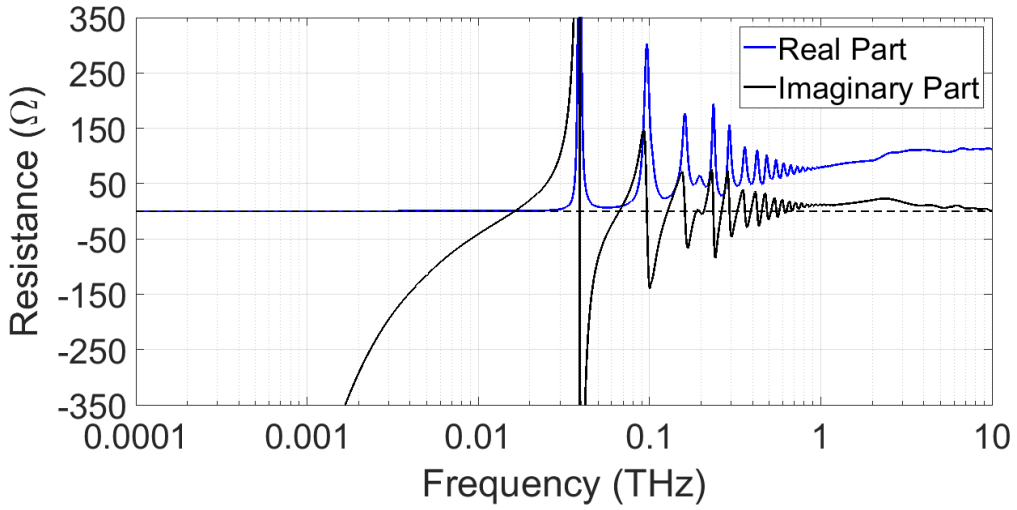

Figure 4.2.: Estimated values of the antenna resistance and antenna reactance.

The photocondutive emitter also incorporated a 10-mm diameter hyperhemispherical silicon lens with a hemisphericity of 0.95 mm, which was attached to the back of the the photoconductor substrate, however, its effect was not taken into account in

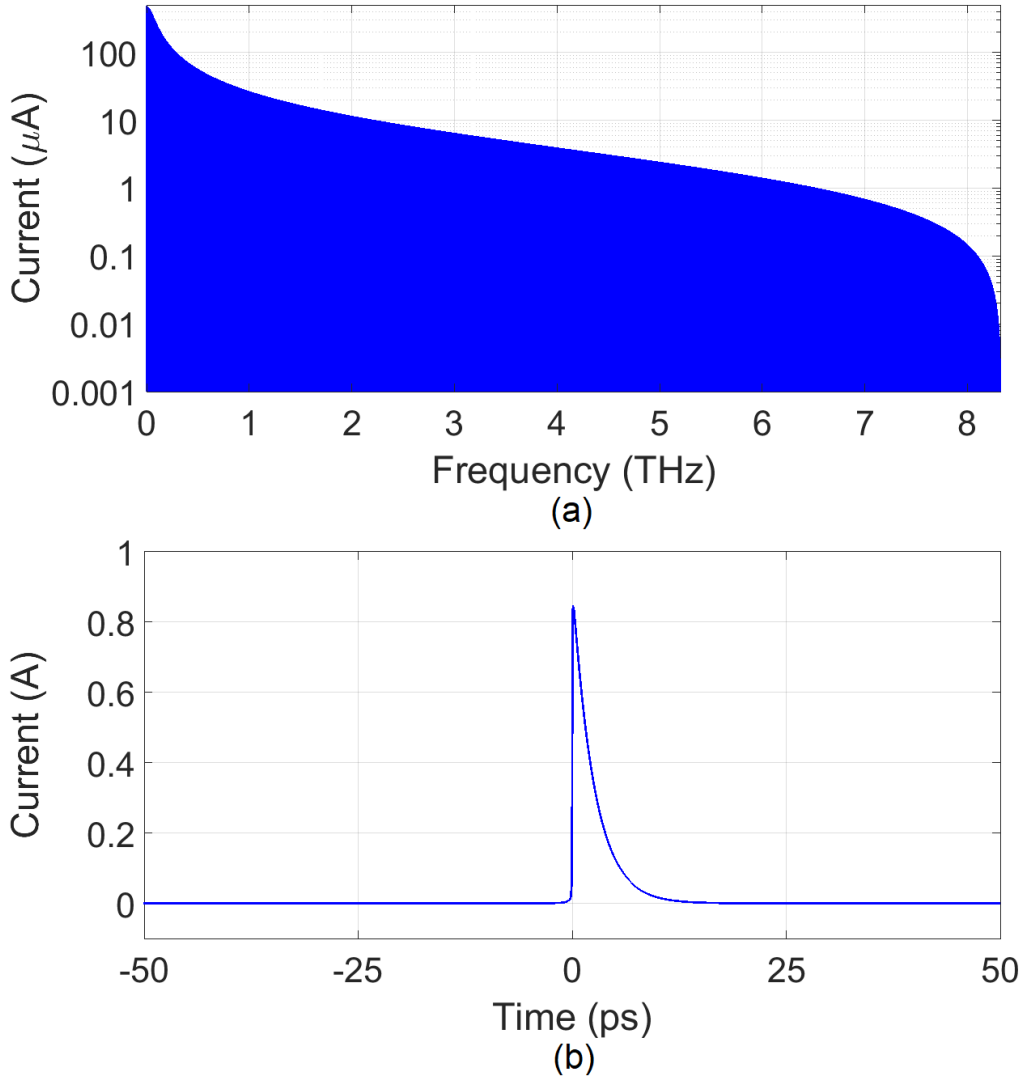

Figure 4.3.: Estimated amplitude of the optically excited current in the photoconductor: (a) per mode and (b) in the time domain.

the antenna simulations, but rather on the propagation losses experienced by the emitted terahertz pulse.

The parameters related to the MLL and to the photoconductor are summarized in Table 4.1, while the results of the antenna impedance simulation are graphically shown in Fig. 4.2. Using those parameters and the model introduced in section 2.3.2, one can readily estimate the amplitude of the optically excited current for each of the modes $i_{pl,n}$ and their associated resistances $r_{pl,n}$ by means of Eqs. 2.32 and 2.38. The values obtained in this way for $i_{pl,n}$ and $r_{pl,n}$ are shown in Fig. 4.3 and Fig. 4.4,

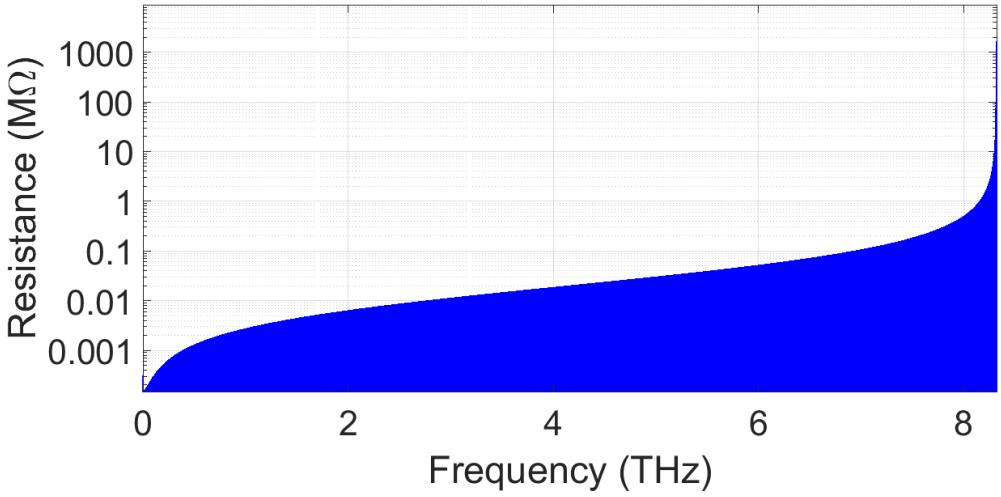

Figure 4.4.: Estimated photoconductor resistance per mode.

respectively. Fig 4.3 also shows the time domain representation of the total generated current, obtained by adding the values of all the current modes with their respective phases.

Having the values of $i_{pl,n}$, $r_{pl,n}$ and the values of the antenna impedance $z_{ant,n}$, it is straight-forward to obtain the current going to the antenna $i_{ant,n}$ and thus the average radiated power per mode $p_{pl,n}$ using Eqs. 2.40 and 2.41. The estimated power spectral distribution obtained in this way is shown in Fig. 4.5. This estimation already takes into account the propagation losses $\eta_{pl,n}$, defined in Eq. 2.45. A value of 0.36 was assumed as the minimum propagation loss η_{min}, and a value of 0.5 THz as the frequency at which half the propagation loss is attained ω_c. Such values were obtained from the results presented in [126] for a similar kind of antenna and terahertz setup.

The highest average terahertz power is estimated to be 82 nW, attained at 0.236 THz, while the total radiated power is estimated to be 390 μW. This is well above the minimum average power that the CW ErAs:InGaAs photoconductive mixers can detect when operating as homodyne detectors when using detection bandwidths of a few Hz. This allows to predict that FreSOD can work well at least for the low-frequency end of the emitted terahertz pulse if one uses narrow detection bandwidths.

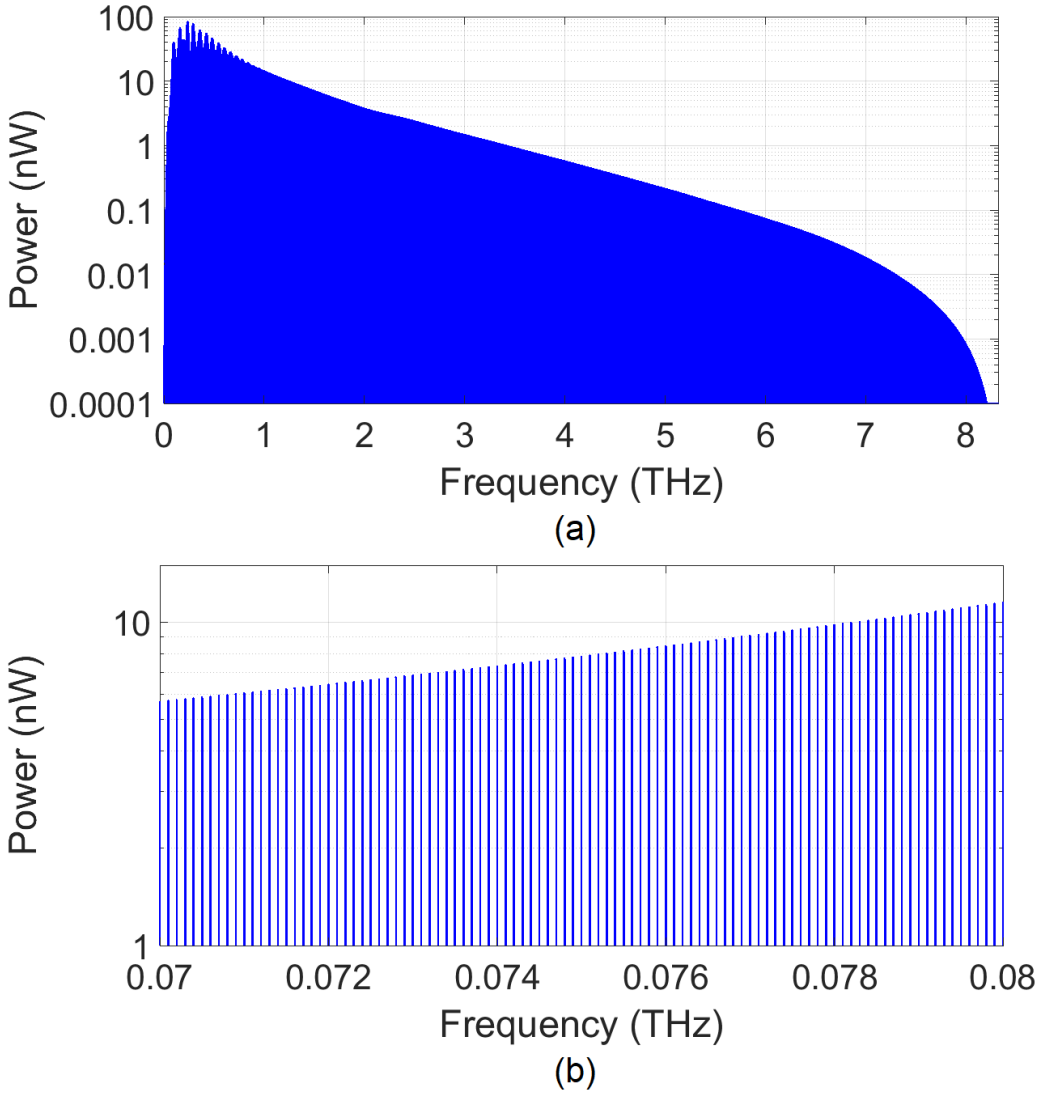

Figure 4.5.: Estimated power spectral distribution for different ranges: (a) 0-8.32 THz (b) 0.07-0.08 THz.

4.3.1. Experimental Demonstration

In order to experimentally demonstrate the capabilities of FreSOD as a measurement technique, two different applications were devised.

In the first one, shown in subsection 4.4.1, FreSOD is used to characterize the amplitude response of a free-space coupled bandpass filter within the 0.070-0.080 THz range. The filter consisted of three stacked dielectric layers: a 205-μm highly-resistive silicon layer, a 1.02-mm quartz layer, and a second 205-μm highly-resistive silicon layer. The surface of the two silicon layers acted as a partially reflective mirror and

the thick quartz layer as a high-Q cavity. The combination of these two features allowed to achieve a naroww spectral feature located between 80-90 GHz.

In the second one, shown in subsection 4.4.2, the phase noise of two terahertz modes having a significant frequency separation is analyzed to demonstrate how FreSOD can help in the experimental characterization of MLL noise.

For both applications, the pulsed photocondutive mixer and the MLL used to drive it were the ones described in the previous section, while the employed CW photoconductive detector was identical to the one described and characterized in Chapter 3, with the difference that instead of being driven by two free-running DFB lasers, it was driven by two selected modes of an EO generated optical frequency comb. This resulted in a photonic local oscillator with a very low timing jitter that permitted to use a narrow detection bandwidth with a relatively low noise level.

Please note that a EO-based CW system is strictly necessary only for phase noise analysis applications, where the highest possible spectral accuracy and purity is required. High resolution spectroscopic measurements only need a CW system with a linewidth as narrow as the detection bandwidth required to detect the donwnconverted mode.

4.3.2. Ultra High-Resolution Characterization of a Filter

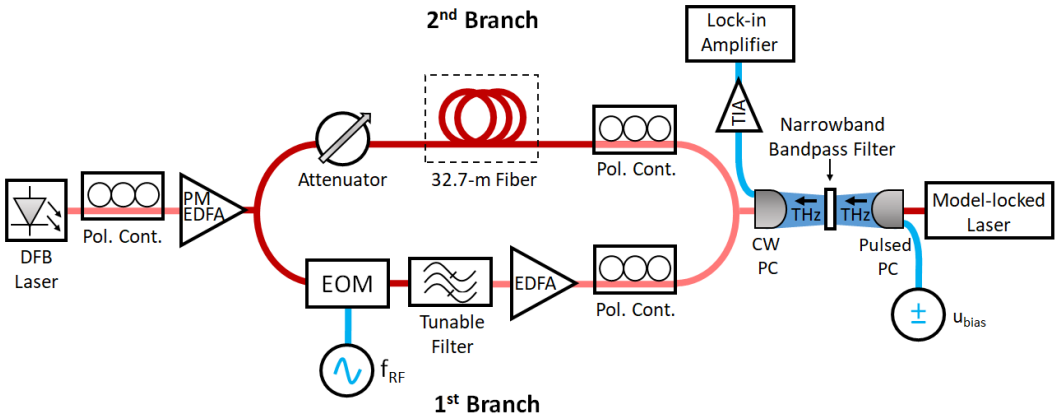

Figure 4.6.: Schematic diagram of EO-based CW optical system for the measurement of the narrowband bandpass filter. The pale red fibers represent non-PM fibers, while the bright red represent PM fibers.

The schematic diagram of the EO-based CW optical system used for this application is shown in Fig. 4.6. It consisted of a single DFB laser whose output was amplified up to 280 mW by an EDFA, and then split into two branches. The optical signal in the first branch was phase-modulated by an EOM driven by a RF generator with frequency f_{RF}. The phase modulation resulted in the generation of sidebands, as mathematically described by the Jacobi-Anger expansion [127]. These sidebands, or modes, were actively locked as they are all harmonics of the same RF signal, thus,

they shared almost the same timing jitter, mostly coming from the common DFB laser source. One of the modes was then selected by a tunable optical filter, and subsequently amplified by a second EDFA. Next, the selected mode m was combined with the main optical mode of the DFB laser carried by the second branch, in which 32.7 m of optical fiber were added to equalize the optical path lengths in both branches. The resulting optical signal containing the combined modes, with an optical average power of 15 mW, was used to drive the CW ErAs:InGaAs photoconductive mixer, resulting in optically-modulated electron density that acted as a local oscillator with frequency $f_{cw} = mf_{RF}$. Given that f_{cw} is the result of the frequency difference between two actively-locked optical modes, as indicated by Eq. 2.12, its spectral purity was of the order of the spectral purity of the function generator, i.e. in the Hz level. This is a direct consequence of the fact that all timing jitter that is common to both modes is removed by the difference frequency generation mechanism of the photoconductor [128]. For the same reason, its accuracy was also in the Hz level. Finally, in order to amplify the modes selectively downconverted by the photonic local oscillator, a PDA-S TIA from TEM Messtechnik with a gain of 3.3×10^6 V/A and a bandwidth of 120 kHz was directly connected to the CW ErAs:InGaAs photoconductor. The amplified downconverted modes were then processed by a MFLI lock-in amplifier with spectral analysis capabilities manufactured by Zurich Instruments, which was directly connected to the TIA.

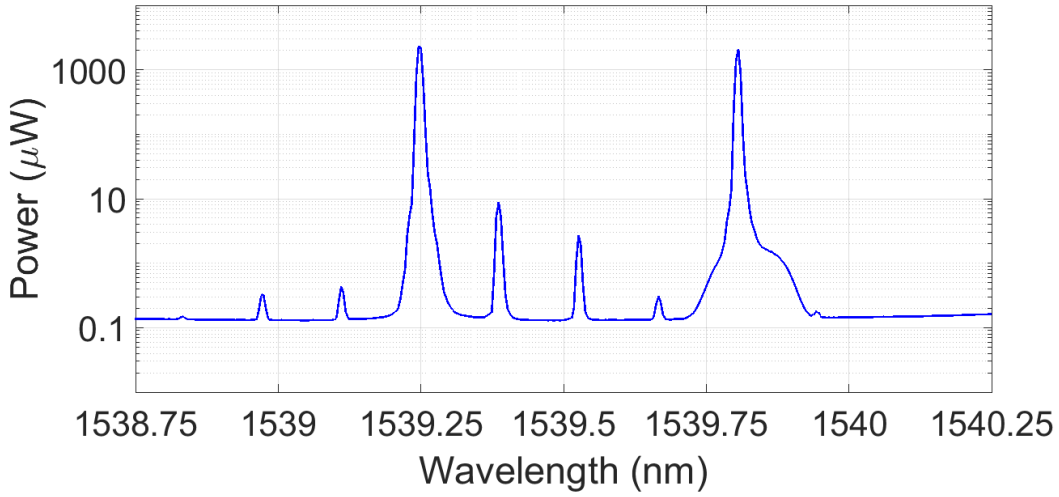

Figure 4.7.: Spectrum of the selected modes for CW generation for the case in which $f_{RF} = 0.0172057895$ THz and $m = 4$. Reproduced from [122] under a creative commons licence.

For the measurement, the CW local oscillator was swept between 0.068823158 THz and 0.07991076484 THz in steps of 99.88835 MHz, which was the actual value of Δf of the MLL driving the pulsed photoconductor during the measurement. In fact, given that the MLL is passively locked, the value of Δf drifts randomly during the course of a few minutes. Therefore, the detection bandwidth must be wide enough to account for this variation during the measurement time, or alternatively, the MLL driving the pulsed photoconductor must be actively locked and then synchronized to the CW system. For the frequency sweep performed here, m was set to 4, and f_{RF} was varied between 17.2057895 GHz and 19.9776912125 GHz in 24.9720875 MHz steps, which was the required frequency step to downconvert all the modes of the terahertz pulse without any gaps. This is what allowed to achieve the highest possible frequency resolution with the particular MLL utilized in this setup.

Fig. 4.7 shows a sample optical spectrum of the combined modes obtained for such configuration. This configuration resulted in a downconverted mode centered around 85 kHz for each of the detected modes. For signal processing, the local oscillator of the spectrum analyzer incorporated in the lock-in amplifier was tuned to 85.6 kHz, the sampling frequency was set to 26.79 kHz, and the detection bandwidth was set to 4 kHz (corresponding to an integration time of 11.97 μs). A sample spectrum of the downconverted mode before demodulation, for the emitted terahertz mode located at Δf_{750} = 0.0749162625 THz, is shown in Fig. 4.8. The two side modes appearing in the spectrum come from the DFB laser used to generate the CW local oscillator.

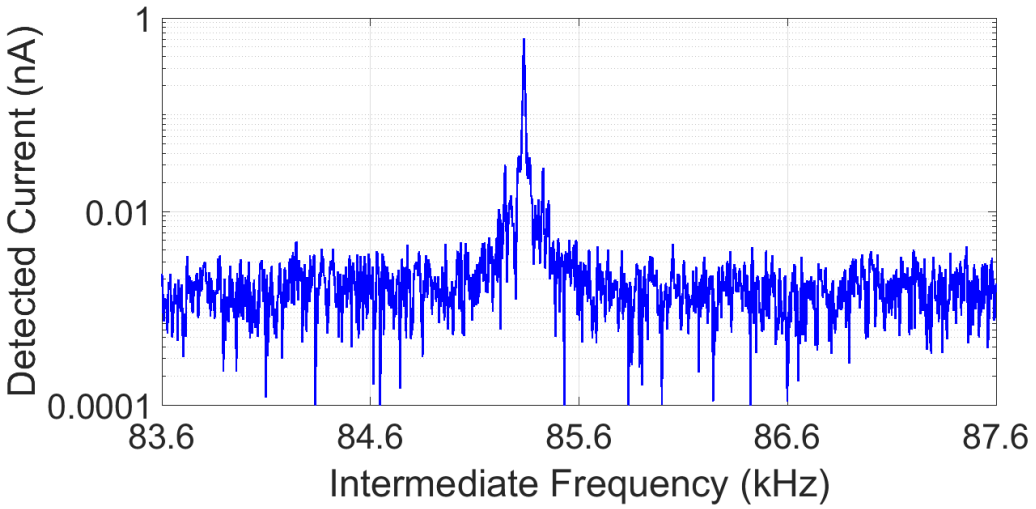

Figure 4.8.: Spectrum of the downconverted mode when f_{cw} was tuned to detect the 750^{th} mode of the emitted pulse, located at Δf_{750} = 0.074916243 THz. Reproduced from [122] under a creative commons licence.

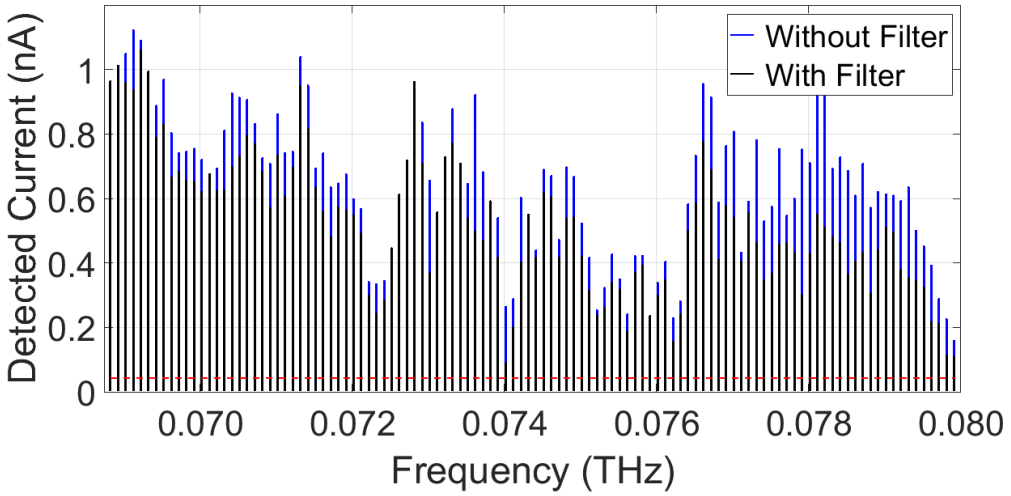

Figure 4.9.: Comparison between the detected currents with (black) and without (blue) filter on the terahertz path. The dashed red line represents the detection limit for this measurement. Reproduced from [122] under a creative commons licence.

The amplitudes of the downconverted modes obtained for the swept frequency range are shown in Fig. 4.9. The figure shows the values obtained with (black) and without (blue) filter in the free-space terahertz path. Each value was obtained after averaging 50 individual measurements at each frequency point in order to increase the measurement precision. The acquisition of the 224 points (112 per sweep) took around 4 minutes.

Fig. 4.10 shows the power transmission coefficient calculated with the values shown in Fig. 4.9 after applying an 11^{th} order moving average filter. The figure also shows the power transmission coefficient obtained using a commercial TDS system with a resolution of 2.49 GHz. The moving average filter in the data obtained with FreSOD was required to mitigate the effect of unwanted reflections inherent to any CW terahertz setup [129]. This fact underscores the extremely high-frequency resolution achieved, which ultimately leads to a more accurate characterization of the filter. In TDS systems, undesired reflections are separated in time, and one would need an extremely long scanning range to see all of them. Since the scanning range in the TDS measurement was limited to 400 ps, part of the information for some frequency components is missing, resulting in a decreased measurment accuracy. Indeed, the higher-than-one transmission coefficient is a direct result of such limited frequency resolution: unwanted reflections for the 70-80 GHz frequency range have very long periods, which overlap in time with the actual filter response, thus, one would require a very long scanning range to achieve the frequency resolution required to separate between unwanted reflections and actual filter response. This is where FreSOD excels,

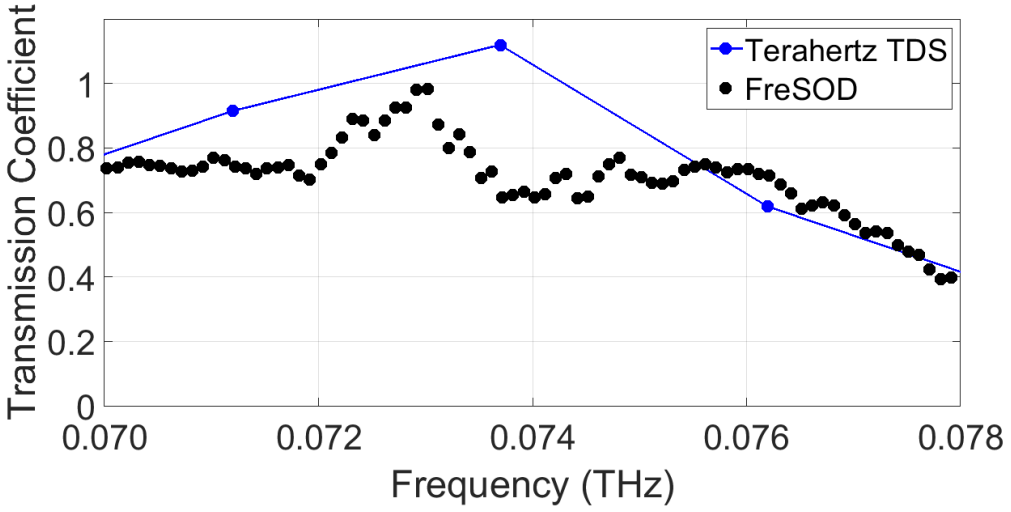

Figure 4.10.: Comparison between the power transmission coefficient obtained with FreSOD (black dots) and the one obtained with a commercial TDS system (blue line). The power transmission coefficient obtained with the TDS system is higher than one because its resolution does not allow to distinguish between the transmission peak of the filter and the transmission peaks due to undesired reflections occurring in the setup at such low frequencies. Reproduced from [122] under a creative commons licence.

enabling a measurement with a much higher frequency resolution and accuracy. It is worth mentioning that the achieved frequency resolution with FreSOD for this kind of applications is ultimately limited by the repetition rate of the MLL, given that it is not possible to measure between the frequency gap existing between any two emitted terahertz modes. As a matter of fact, a CW terahertz system with two tunable free-running CW lasers could acheive a higher frequency resolution but with a lower frequency accuracy, since the frequency accuracy would depend on the linewidth of the free-running lasers and on their frequency calibration, while with FreSOD it just depends on the accuracy of the utilized RF generator.

As a final step, the total terahertz average power arriving at the ErAs:InGaAs photoconductor was measured using a pyroelectric calibrated detector similar to the one used for the characterization presented in Chapter 3. The measured power was 76 μW, which is almost five times smaller than what was estimated in the previous section. The difference between the measured and the estimated value is likely caused by the overly simplistic approach used to estimate the losses during propagation. However, the actual measured power can be used to have an idea of the highest possible mode that could be measured under the same experimental conditions.

To do so, one can normalize the estimated power distribution to the 76 μW that

were measured in order to find the minimum terahertz power that was detected during the performed characterization. The result is that the smallest detected power must have been around 1 nW, attained at 0.068 THz, exhibiting a signal-to-noise ratio of 22.5 during the measurement. Making use of that result, the estimated power distribution, and the responsivity calculated in the previous Chapter, it is possible to predict that highest mode that could be detected under the same conditions should be located above 1 THz. Unfortunately, the EO-based CW system used in this measurement could only reach a maximum of 0.080 THz.

4.3.3. Comparison of the 750^{th} and 3400^{th} terahertz modes

In this measurement the goal is not the characterization of a sample, but the characterization of the terahertz pulse itself. In particular, the interest is to show how FreSOD can be used to study the phase noise behaviour as a function of the mode number in a terahertz pulse, since ultimately, this can help to characterize the phase noise of the MLL iteself. Indeed, the phase noise of the n^{th} terahertz mode is a measure of the degree of coherence between any two MLL modes having a separation of $n-1$ modes.

In section 4.2, the phase noise of a given terahertz mode and that of the CW photonic local oscillator were represented in time domain by the short-term timing jitter, given by $\phi_{pl,n}(t)$ and $\phi_{cw}(t)$, respectively. The condition established for $\phi_{dt}(t)$ to be a good indicator of $\phi_{pl,n}(t)$ was that $\sigma_s\big(\phi_{cw}(t)\big) \ll \sigma_s\big(\phi_{pl,n}(t)\big)$. In practice, the short-term timing jitter (in the time domain) is somewhat difficult to measure, so the linewidth (in the frequency domain) will be used instead, given that it can be easily measured using a spectrum analyzer[2].

The relationship between short-term timing jitter, phase noise and linewidth has been studied extensively. Here, I will adopt the simplified relationship proposed in [130], in which the phase noise spectral density $\mathcal{L}(f)$ is expressed as

$$\mathcal{L}(f) = \frac{1}{\pi}\frac{\delta f}{(\delta f)^2 + f^2} \tag{4.104}$$

where $2\delta f$ is the 3-dB linewidth (FWHM) of the signal and f is the offset from the center frequency. I have implicitly assumed a Lorentzian line shape for simplicity here, however, an equivalent expression can also be written for a Gaussian line shape.

Similarly, the phase noise can also be written as a function of the short-term timing jitter variance $\sigma_s^2\big(\phi(t)\big)$, resulting in [130]

$$\mathcal{L}(f) = \frac{\sigma_s^2\big(\phi(t)\big) f_s^3}{f^2} \tag{4.105}$$

where f_s is the center frequency of the signal. By equating Eq. 4.104 and 4.105, and by considering time scales shorter than the inverse of the linewidth, i.e. $t \ll \frac{1}{2\delta f}$, one obtains

[2] Actually, the most appropriate way to characterize the phase noise of a signal is to use a phase noise analyzer, but there was none available during the measurements.

$$2\delta f \approx 2\pi f_s^3 \sigma_s^2\big(\phi(t)\big). \tag{4.106}$$

This means that for a fixed frequency, a small linewidth is directly proportional to a small short-term timing jitter variance. This means that the requirement of having a local oscillator with a much smaller timing jitter variance than that of the mode to be analyzed can be directly translated as having a local oscillator linewidth much narrower than that of the mode to be analyzed.

Hence, in order to analyze the spectral characteristics of the higher order modes of the terahertz pulse in which the phase noise becomes significant, a different EO-based CW system featuring a wider span was used. A major difference with respect to the previous EO-based CW system was that the mode selection for the CW signal generation was performed using lasers as active filters instead of using tunable passive filters.

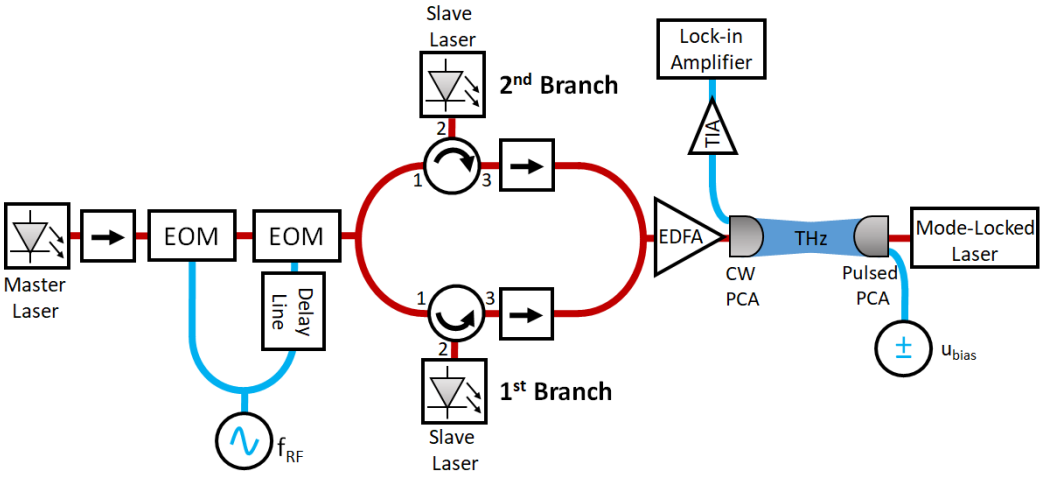

Figure 4.11.: Schematic diagram of the EO-based CW optical system for the spectral characterization of the 750^{th} and 3400^{th} modes.

The schematic diagram of the system, developed by the Sensors and Instrumentation Techniques Group of Universidad Carlos III de Madrid, is shown in Fig. 4.11. It consisted of a discrete-mode master laser whose output was modulated by two cascaded EOMs driven by a RF generator with frequency f_{RF}. The resulting optical signal, containing several sidebands of the main laser mode [127], was split into branches. In each of the two branches, a discrete-mode laser acted as a tunable active filter in a process known as optical injection locking. This process is described in detail in [131], but it basically consists of tuning the cavity of the discrete-mode slave lasers to match the frequency of the mode to be selected. In the end, the selected modes in each of the branches, with mode index difference m, are combined and subsequently amplified by an EDFA to reach 30 mW. The selected modes then generate the CW local oscillator with a frequency $f_{cw} = mf_{RF}$ driving the ErAs:InGaAs

photoconductor. As in the previous system, the ErAs:InGaAs photoconductor was then connected to the PDA-S TIA from TEM Messtechnik with a 3.3×10^6 V/A gain and a 120 kHz bandwidth, and from there to the MFLI lock-in amplifier from Zurich Instruments with spectral analysis capabilities.

The advantage of this EO-based CW system is the capability of achieving a substantially higher local oscillator frequency with a high spectral purity and a high spectral accuracy, but without being hindered by the excessive noise due the strong amplification required after the passive optical filters. A sample spectrum of the optical signal employed for CW local oscillator generation obtained with this EO-based system is shown in Fig. 4.12. As with the previous CW system, the spectral purity is ensured by the difference-frequency mechanism used for local oscillator generation, which removes the timing jitter common to all the electro-optically generated modes, ultimately limiting the jitter to that of the RF generator [128]. The spectral accuracy is also given by the same mechanism, which makes the local oscillator frequency accuracy only dependent on the RF generator. The 3-dB linewidth of the RF generator used in this system was measured to be narrower than 1 Hz, and its frequency stability better than 0.33 Hz/s. Its frequency accuracy is as good as its last calibration, but absolute frequency accuracy can be achieved by locking the generator to a frequency standard, as demonstrated in [131]. This would also improve the frequency stability.

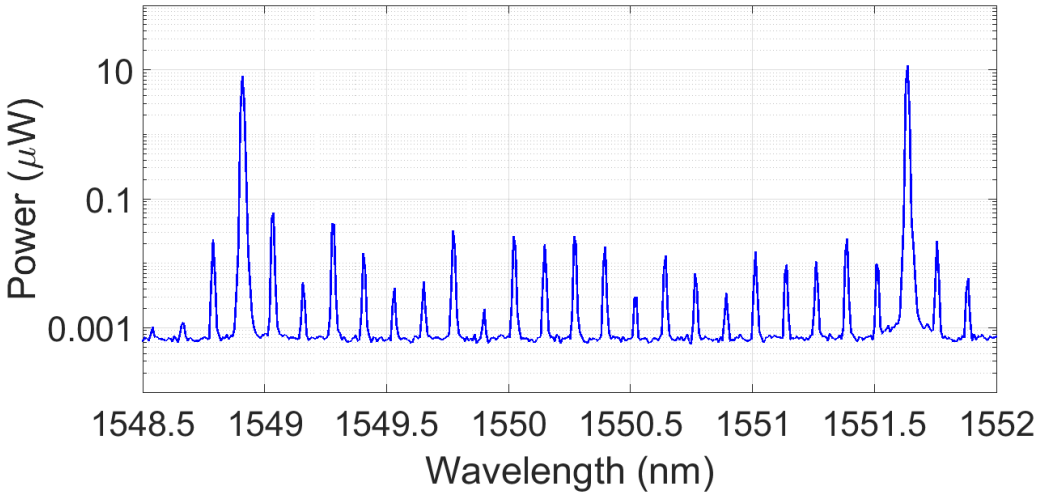

Figure 4.12.: Spectrum of the selected modes for CW generation for the case in which $f_{RF} = 0.0154373108987$ THz and $m = 22$. Reproduced from [122] under a creative commons licence.

The disadvantage of this EO-based CW system is the difficulty of performing a frequency sweep without the need to manually tune the lasers every time the frequency is changed, which is the reason why it was not used for the characterization

of the filter.

Two different modes of the emitted terahertz pulse were analyzed in this application: the 750^{th} and the 3400^{th}. For each of them, the power spectrum was recored.

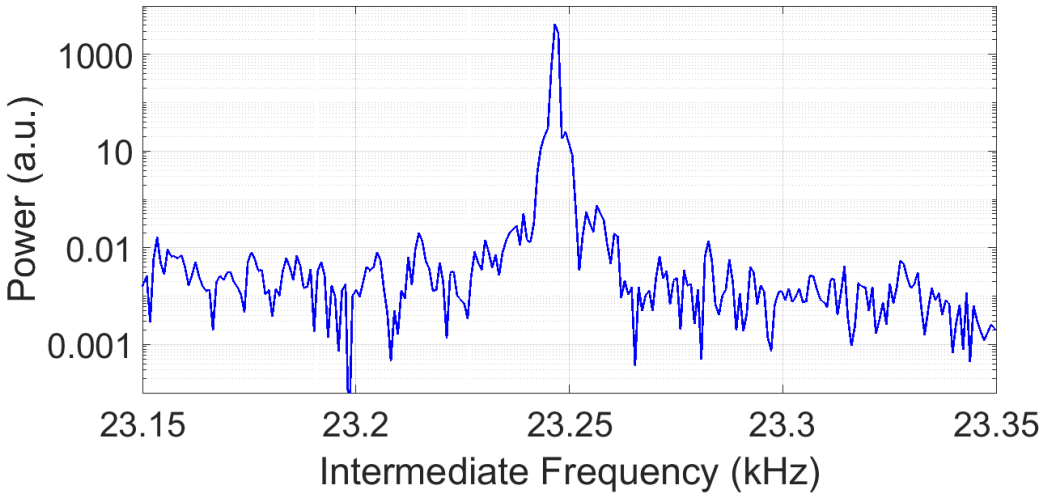

Figure 4.13.: Detected power spectrum of the 750^{th} mode located at 0.0749166255 THz. Resolution bandwidth: 0.817 Hz. Sweep time: 1.22 s. Estimated 3-dB linewidth: < 1.33 Hz. Reproduced from [122] under a creative commons licence.

Fig. 4.13 shows the power spectrum captured for the 750^{th} mode. For this measurement $\Delta f = 99.888834$ MHz, indicating that its frequency Δf_{750} was actually 0.0749166255 THz. In order to detect it, f_{RF} was set to 7.49166025 GHz, and m to 10. This resulted in a local oscillator frequency of 0.0749166025 THz, with a corresponding intermediate frequency of around 23 kHz. The center frequency of the spectrum analyzer integrated in the lock-in amplifier was then set to 23.25 kHz, the resolution bandwidth to 0.817 Hz, and the sweep time to 1.22 s. A 3-dB linewidth of 1.33 Hz was found to fit the measured spectrum, but given that in the frequency domain the measured spectrum is the convolution between the local oscillator spectrum and the terahertz mode spectrum, and that the local oscillator linewidth is also in the 1-Hz level, for this case, it is only possible to give an upper limit on the linewidth of the detected mode. Hence, one can say that the local oscillator linewidth and the 750^{th} mode linewidth are both narrower than 1.33 Hz. An RF generator with a better phase noise performance would be needed to perform a more accurate characterization.

Fig. 4.14 shows the power spectrum captured for the 3400^{th} mode. In this case $\Delta f = 99.888508$ MHz, resulting in $\Delta f_{3400} = 0.3396209272$ THz. For its detection, f_{RF} was set to 15.4373108987 GHz, and m to 22 to get a local oscillator frequency of

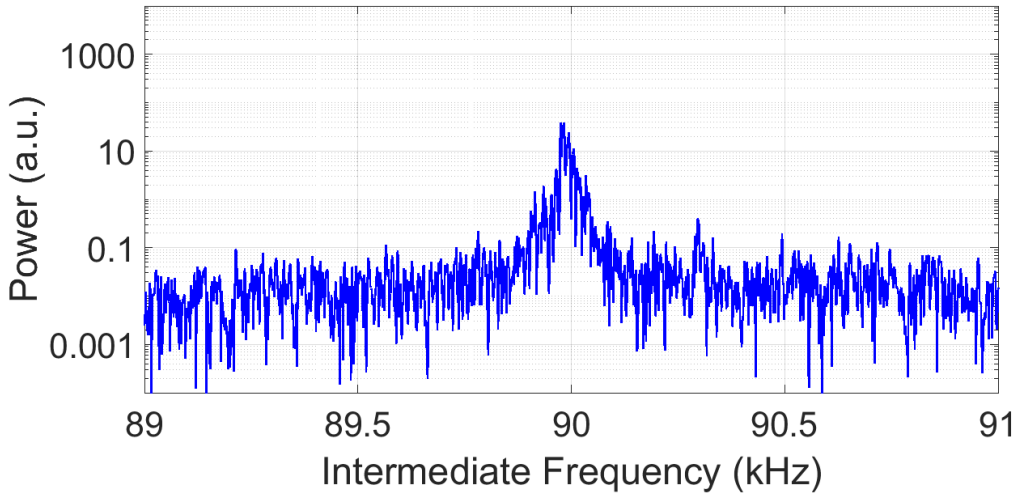

Figure 4.14.: Detected power spectrum of the 3400^{th} mode located at 0.3396209272 THz. Resolution bandwidth: 1.63 Hz. Sweep time: 0.61 s. Estimated 3-dB linewidth: 20.36 Hz. Reproduced from [122] under a creative commons licence.

0.3396208397714 THz, with a corresponding intermediate frequency of around 90 kHz. The spectrum analyzer was tuned accordingly, with the resolution bandwidth set to 1.63 Hz, and the sweep time to 0.611 s. A 3-dB linewidth of 20.36 Hz was found to fit the spectrum. The broadening of the linewidth, when compared to the one obtained for the 750^{th} mode, is clear. It might be argued that the broadening might be caused by the local oscillator, given that the mode number difference was increased from 10 to 22 for this case. However, from the measurement of the linewidth obtained for the 750^{th} mode, it can be inferred that in the worst case, for a mode difference of 10, the local oscillator would have a linewidth of 1.33 Hz. Therefore, when increasing from a mode difference of 10 to a mode difference of 22, one would expect an increase in the linewidth of less than 4.84 times, assuming a worst-case quadratic increase of the linewidth as function of mode number difference [128]. Since the increase in the measured linewidth was much higher than that, and since the 4.84-times increase in the linewidth of the CW local oscillator is a worst-case estimation, the broadening can be associated to the MLL generating the terahertz pulse.

Despite the measured increase in the linewidth, the phase noise performance of the passively locked MLL is quite impressive: a linewidth of less than 20 Hz for a tone generated by photomixing modes that are 3339 modes apart. On the one hand, this is somewhat expected, the linewidth of microwave signals generated by photomixing different modes of passively locked MLLs has been shown to be practically constant for the first hundreds of modes [120]. On the other hand, there is still a lack of theoretical understanding on how the phase noise behaves in passively locked MLLs

[132] [121], mainly due to the lack of experimental data for its behavior at higher order modes. FreSOD might help to fill that gap.

4.4. Conclusions

The foundations of a new optoelectronic technique for the detection terahertz pulses have been laid out in this chapter. The technique, coined FreSOD, allows a Hz-level frequency resolution, improving by several orders of magnitude the maximum resolution achieved with other optoelectronic time-domain detection techniques. When implemented with an EO-based CW system, the achieved frequency coverage is limited by the maximum frequency allowed by the EO-based generation mechanism, and by the available terahertz power in each modes of the terahertz pulse. Both factors can be significantly improved to achieve frequency coverages of around 1 THz. For example, one could use an architecture similar to the one shown in [133] to implement an EO-based CW system with a frequency coverage up to 1 THz, and one could use a pulsed photoconductor similar to the one shown in [134] to get as much as 0.637 mW of total emitted terahertz power. This would allow a thorough characterization of the phase noise behavior of terahertz pulses driven by passively-locked MLLs, and a characterization of the noise in the passively-locked MLLs themselves, given that both parameters still lack a good theoretical and experimental characterization.

Even though I have only characterized the short-term variance of the individual terahertz modes' phase noise in this Chapter, i.e. their linewidth, it is also possible to characterize their long-term variance with the same technique. To this end, the local oscillator generated by the EO-based CW system can be locked to a frequency standard, which could enable to have a local oscillator with frequency stabilities of around 5 Hz per hour, as shown in [131].

Lastly, if the phase noise analysis of the individual terahertz modes is not required, FreSOD can also be implemented using a CW system driven by two simple narrow-linewidth CW lasers without the need of using an EO-based CW system. This configuration would still allow to achieve a better resolution than the one achieved with traditional TDS systems. The main requirement would be to have a detection bandwidth that is higher than the CW local oscillator linewidth. This is perfectly achievable with external cavity lasers, exhibiting linewidths as low as 5 kHz [128], since, as shown here, detection bandwidths of a few tens of kHz still suffice to have a low enough noise level to perform the detection. The additional advantage of this configuration, besides the improved resolution, would be its simplicity: it would not need a mechanical delay stage or second MLL to preform the pulse detection.

5. Application 2: A Sub-Terahertz Optoelectronic Spectrum Analyzer

5.1. Introduction and State of the Art

In this Chapter, I present the second application demonstrated in this thesis, which in fact, can be considered as an extension of the one presented in the previous Chapter. While the goal of the previous application, namely FreSOD, was the detection of the individual modes composing a terahertz pulse, either for spectroscopic measurements or for phase noise characterization, the goal of the application presented here is the detection of arbitrary sub-terahertz signals for characterizing their spectra, which also involves a characterization of their phase noise. Consequently, many of the concepts and the tools utilized in both of the applications are the same. In particular, the use of an EO-based CW local oscillator with a very low phase noise.

However, there is a fundamental difference between FreSOD and the application presented here. FreSOD required an external electronic spectrum analyzer to operate, hence, the ultimate frequency limits were set by the features of the external electronic spectrum analyzer.

In this chapter I present a solution that does not require an external spectrum analyzer. Thus, in practice, the ultimate resolution limits are just set by the EO-based CW local oscillator. This application therefore constitutes a true optoelectronic sub-terahertz spectrum analyzer.

Compared to fully electronic architectures, a spectrum analyzer based on an optoelectronic architecture offers the following advantages:

1. Lower cost. Since the commercially available options for spectrum analyzers operating in the sub-terahertz range, i.e. the range going from 50 to 300 GHz, are all based on supplementing frequency extenders to electronic spectrum analyzers [135, 136], it is necessary to acquire around five of those frequency extenders to cover the whole sub-terahertz range; although with newer (and more expensive) spectrum analyzer versions this number can be reduced to three [137]. In any case, the overall cost of they system is very high. The reason behind the comparatively narrow frequency coverage of the extenders is the utilization of hollow-core metallic waveguides for the in-coupling of the sub-terahertz signal to be analyzed, which is honed for optimal performance only over a narrow frequency range. Photoconductive mixers, to the contrary, are usually optimized for broadband operation due to their optoelectronic nature. The local oscillator required for the downconversion, i.e. the laser

signal, is free-space coupled, while the in-coupling of the sub-terahertz signal is normally designed to achieve a broadband performance, either by using a self-complementary antenna or a CPS transmission line. The only fundamental frequency limitation is just set by the carrier dynamics, but as shown in Chapter 3, it only hinders the performance for frequencies above the sub-terahertz range.

2. Ease of use. The fact that a single photoconductive mixer can be used to replace a whole set of frequency extenders makes the measurement process much simpler, eliminating the need of exchanging components in the middle of measurement, or even the need of performing a recalibration [26].

3. Superior phase noise performance. The utilized frequency extenders in the commercially-available options are composed of electronic sub-harmonic mixers that, in effect, multiply the frequency of a microwave local oscillator and mix it for downconversion with the sub-terahertz signal to a suitable intermediate frequency. This means that the phase noise of the electronic local oscillator also gets multiplied by the harmonic mixer. Indeed, the phase noise increase is proportional to the square of the harmonic order [138], since correlated phase noise added in the multiplication process is never removed. This is in stark contrast with respect to photocondutive mixers driven by EO-based CW systems, in which all common phase noise is removed due to the frequency-difference generation mechanism of the photomixing process, as explained in the previous Chapter. The net result is a superior phase noise performance, as suggested in [139].

Yet, all high-resolution spectrum analyzers for the sub-terahertz range that have been demonstrated with photoconductive mixers have used MLLs to excite the electron density that acts as local oscillator [140–143]. The advantage of that architecture is that it provides an extremely wide frequency coverage. Its main disadvantage is the ambiguity of the downconversion process: since any of the optically excited modes in the MLL-driven photoconductor can act as a local oscillator, it is impossible to know which one downconverted the incoming sub-terahertz signal without prior knowledge of it. Its frequency remains ambiguous unless one has some approximate idea of it spectral location [143]. A possible solution to this problem is to vary the repetition rate of the MLL to be able to identify the exact origin of the local oscillator mode that downconverted the incoming sub-terahertz signal [140], however, this requires having a variable repetition rate MLL, moreover, it makes real-time detection challenging. Another possibility is to implement a dual-comb detection scheme where two photocondutive mixers driven by two separate but synchronized MLLs, each one having a different repetition rate. The difference in frequency between the two donwconverted modes, together with the knowledge of the two different repetition rates, allows to determine the frequency of the incoming sub-terahertz signal, as shown in [142], nevertheless, it makes the spectrum analyzer architecture very complex.

The optoelectronic spectrum analyzer demonstrated here employs an EO-based CW system to drive a photocondutive mixer instead of a MLL. This allows to remove the ambiguity of the downconversion process associated with the presence of the thousands of modes excited by a MLL. At the same time, the EO-based CW system allows to achieve an extremely low phase noise, and as a consequence, a high spectral resolution.

The optoelectronic spectrum analyzer architecture based on CW photocondutive mixers was devised by Prof. Dr. Sascha Preu [144]. My contribution to the architecture was the introduction of an EO-based CW system and the introduction of a predominantly digital intermediate frequency chain. The former allowed to increase the resolution by several orders of magnitude. The latter allowed to simplify the post-detection electronics and avoided the need of an external spectrum analyzer or lock-in amplifier.

The details of this novel spectrum analyzer architecture have been published in [145], and many of the published results, figures and tables are reused throughout the different sections of this Chapter to aid in the explanation of the architecture, in particular, Figs. 5.1-5.9 and Table 5.1.

Section 5.2 describes each of the subsystems composing the architecture. Section 5.3 introduces the two possible operation modes of the spectrum analyzer. Section 5.4 shows the experimental results obtained with both operation modes. Section 5.5 analyzes the obtained experimental results, and compares them with the results obtained by the MLL-based optoelectronic architectures, and by the purely electronic architectures. Finally, section 5.6 gives some concluding remarks and discusses the future prospects of the demonstrated architecture.

5.2. Spectrum Analyzer Architecture

The architecture of the spectrum analyzer is composed of three subsystems: the EO-based CW subsystem generating the local oscillator, the ErAs:InGaAs photoconductive mixer performing the downconversion, and the predominantly digital intermediate frequency chain acquiring the downconverted spectrum. A schematic diagram showing the main components of each of the subsystems is shown in Fig. 5.1. Each of them is detailed in the following subsections.

5.2.1. EO-based Subsystem for CW Local Oscillator Generation

This subsystem, illustrated also in Fig. 5.1, is almost identical to one used to generate the CW local oscillator for the characterization of the filter in the FreSOD demonstration of the previous Chapter. It was composed of the same DFB laser connected to the same EDFA whose output was split into two branches after reaching an optical power of 230 mW. In a similar manner, the optical signal in the first branch was phase-modulated, but in this case by two cascaded EOMs, both driven by a RF signal generator with frequency f_{RF}, which was digitally controlled by a computer. The two EOMs driven in series effectively increased the maximum

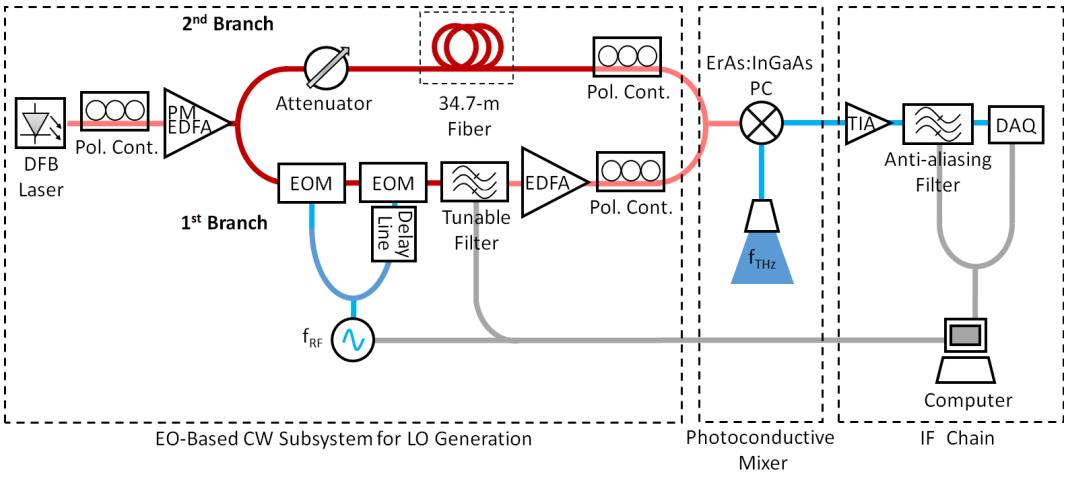

Figure 5.1.: Schematic diagram of the demonstrated optoelectronic spectrum analyzer (DAQ: Data acquisition card, PC: Photoconductor, Pol. Cont.: Polarization Controller). Reproduced from [122] under a creative commons licence.

achievable frequency. Right after the EOMs, the optical tunable bandpass filter, controlled by the same computer, selected mode number n of the EO generated modes that was subsequently amplified by the second EDFA. Meanwhile, the main optical mode propagating in the second branch was delayed by 34.7 m of fiber in order to compensate for the delay introduced by the two EOMs, the filter and the second EDFA in the first branch. Afterwards, the optical power in both branches was equalized by a series of optical attenuators, while the polarization was matched by means of two polarization controllers. Finally, the two branches were combined, resulting in an optical signal with a power ranging between 14 and 23 mW, depending on the selected mode. The output of this subsystem was an optical signal composed of two coherent modes with a frequency separation of nf_{RF}. As explained in the previous Chapter, these two optical modes were transformed into a spectrally accurate and pure sub-terahertz local oscillator by the difference-frequency mechanism of the photomixing process, with the spectral accuracy and purity solely determined by the RF generator [131], which featured a 3-dB linewidth of less than 1 Hz, and a frequency stability better than 0.33 Hz/s. If even higher spectral purity is required, the RF generator could be locked to a frequency standard [131].

Sample spectra of the optical output of this subsystem are shown in Fig. 5.2. The maximum measured frequency difference was 90 GHz, obtained with $n = 5$ and $f_{RF} = 18$ GHz, while the lowest one was 50 GHz, obtained with $n = 3$ and $f_{RF} = 16.667$ GHz. Thus, the measured frequency coverage was 40 GHz. Higher frequencies can easily be achieved by simply adding more cascaded EOMs, using wider-bandwidth EOMs, or by mixing positive and negative sideband orders by means of an additional filter. Indeed, similar photonic systems have demonstrated

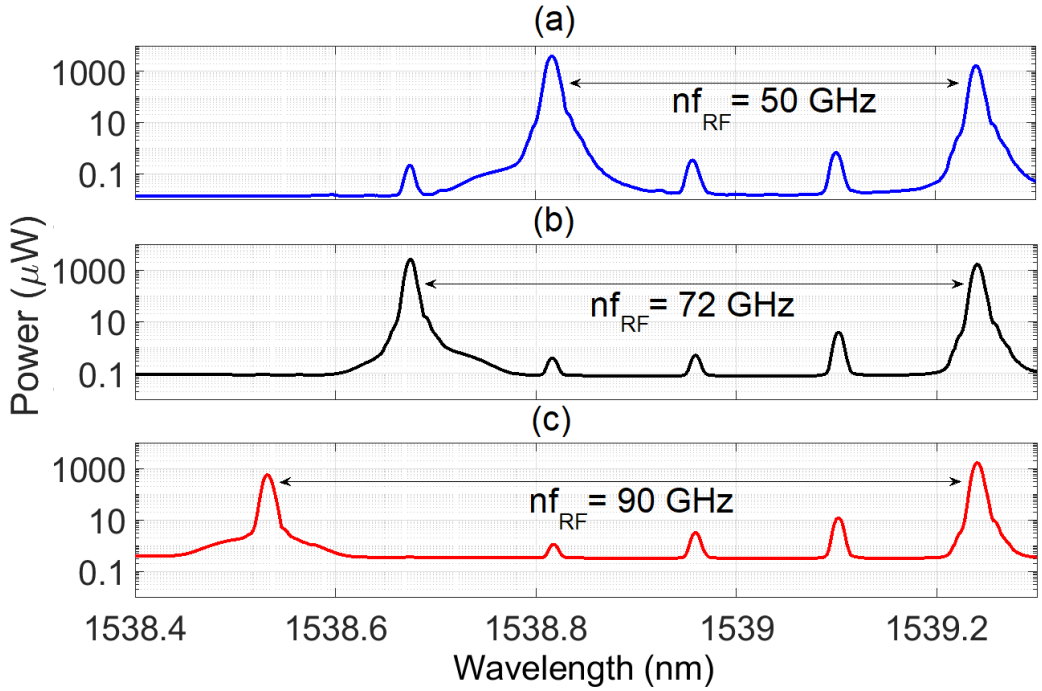

Figure 5.2.: Optical spectrum of the EO-based CW local oscillator subsystem output for three different configurations: (a) $n = 3$, $f_{RF} = 16.667$ GHz, (b) $n = 4$, $f_{RF} = 18$ GHz, and (c) $n = 5$, $f_{RF} = 18$ GHz. The shoulders in each of the peaks originate from the side lobes of the DFB laser, but they are suppressed by 30 dB. The undesired modes appearing periodically are due the finite roll-off of the optical filter. Further or higher order filters would allow for better mode suppression. Reproduced from [122] under a creative commons licence.

frequency coverages up to 1 THz [133]. Lower frequencies can certainly be achieved by reducing f_{RF}, the limit is just set by the minimum bandwidth of the optical filter, which is 25 GHz. However, below 50 GHz the photoconductive mixer stops working efficiently due to the limited bandwidth of its antenna, as explained in the next subsection.

5.2.2. Photoconductive Mixer

This subsystem is composed of an ErAs:InGaAs photoconductor and a logarithmic spiral antenna directly connected to it, which receives the sub-terahertz signal collected by a hyper-hemispherical silicon lens attached to the photoconductor substrate, as shown in Fig. 5.3 (a).

The ErAs:InGaAs photoconductive material implemented in the mixer was superlattice A, which was covered by an electrode structure identical to the one described

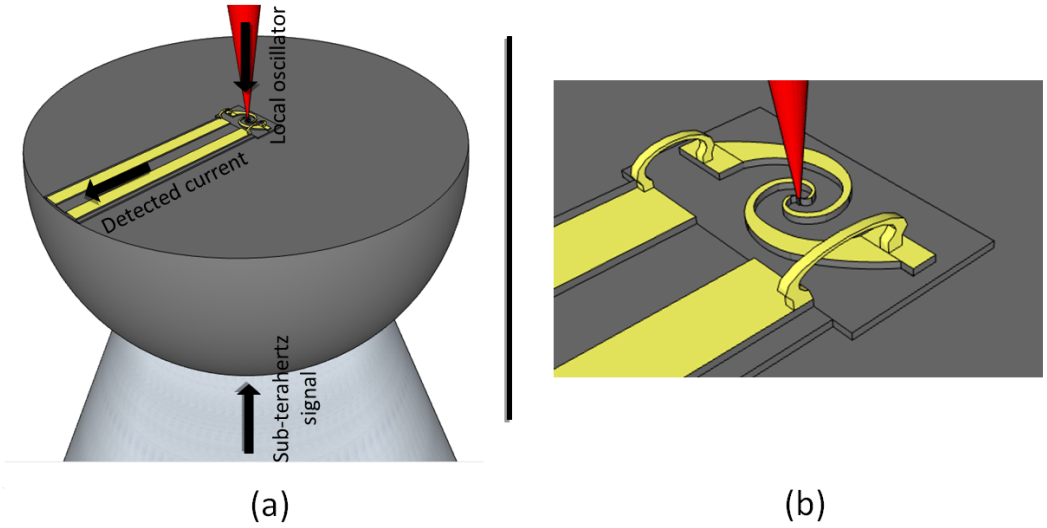

Figure 5.3.: (a) Graphical representation of the photocondutive mixer and the attached silicon lens used to collect the sub-terahertz signal. (b) Magnified view of the photoconductive mixer and its connection the CPS transmission line. Reproduced from [122] under a creative commons licence.

in section 3.3. The electrode structure was attached to the logarithmic spiral antenna, exhibiting a maximum radius of 600 μm, as illustrated in Fig. 5.3. Its impedance was similar to that of the logarithmic-periodic antenna employed in the characterization presented Chapter 3, given that both antennas are self-complementary. The attached silicon lens also had a diameter of 10 mm and hyperhemisphericity of 0.95 mm. Therefore, the performance of the mixer should be very similar to the one shown in Chapter 3.

The operation of the ErAs:InGaAs photoconductor as a heterodyne mixer can be modelled using the same approach employed in the previous Chapter, in which the optically-modulated CW electron density $n_{cw}(t)$, with angular frequency $\omega_{cw} = 2\pi n f_{RF}$ and timing jitter $\phi_{cw}(t)$, acts as local oscillator. The additional modulation of the electron transport velocity by the electric field of the sub-terahertz signal $e_{THz}(t)$ transforms $n_{cw}(t)$ into a steady current density with magnitude $j_{dt}(t)$, as expressed by Eq. 2.46, turning the photoconductor into a broadband heterodyne mixer. The bandwidth limitations are just set by the attached antenna and the carrier lifetime τ_{cw}, as explained in depth sections 2.3.3 and 3.4.

For the specific case where $e_{THz}(t)$ is a single-frequency tone with angular frequency ω_{THz}, timing jitter $\phi_{THz}(t)$, and field strength e_0, $j_{dt}(t)$ can be written as

$$j_{dt}(t) \sim \left(1 + \frac{\cos\left(\omega_{cw}t + \phi_{cw}(t)\right)}{\sqrt{1 + (\omega_{cw}\tau_{cw})^2}}\right) e_0 \cos\left(\omega_{THz}t + \phi_{THz}(t)\right) \tag{5.107}$$

however, of all the terms in Eq. 5.107, only the difference-frequency term generated

by the multiplication between the two cosine functions can be acquired by the detection bandwidth of the digital intermediate frequency chain. That difference-frequency term is the downconverted current $i_{dt}(t)$ detected by the intermediate frequency chain, i.e.

$$i_{dt}(t) \sim e_0 \cos\left(\omega_{IF} t + \phi_{THz}(t) - \phi_{cw}(t)\right) \tag{5.108}$$

with $\omega_{IF} = \omega_{THz} - \omega_{cw}$.

Note that I have assumed that the photocondutive mixer is operating under the small-signal regime. For the large-signal regime one cannot decouple the dynamics of $n_{cw}(t)$ from the dynamics of the $e_{THz}(t)$. The coupling dynamics between $n_{cw}(t)$ and $e_{THz}(t)$ inevitably leads to a non-linear behavior, which has not been thoroughly studied yet, as explained in section 2.3.3. However, the conversion efficiency of that process is at least one order of magnitude lower than the one exhibited by the small-signal regime. Hence, for the most part, this non-linearity can be neglected.

5.2.3. Intermediate Frequency Chain

The intermediate frequency chain was composed of a TIA (PDA-S from TEM Messtechnik), a reconfigurable analog anti-aliasing filter (LTC1564 from Linear Technology), and a data acquisition card (USB-6210 from National Instruments). The TIA featured a gain of $3.33{\times}10^5$ V/A. It was directly connected to the ErAs:InGaAs photoconductive mixer via a CPS transmission line in order to transform the relatively small value of $i_{det}(t)$ into a voltage. The output voltage was then fed to the anti-aliasing filter which was digitally controlled by the computer driving the local oscillator subsystem. The filter had a tunable cutoff frequency f_c that could be tuned between 10 kHz and 150 kHz in steps of 10 kHz. Its output was connected to the acquistion card, which featured a maximum reconfigurable sampling frequency of 250 kS/s and was connected to the controlling computer.

In principle, the maximum detection bandwidth of the subsystem Δf_{det} should be 125 kHz, according to the Nyquist–Shannon theorem. However, this would have required an analog anti-aliasing filter with an extremely sharp response that prevented any frequencies higher than 125 kHz to be sampled by the acquisition card. Since all analog filters have a rather smooth roll-off, f_c must be chosen lower than that limit. In this case, f_c was chosen a factor of approximately two lower than the Nyquist-Shannon limit. For the maximum sampling frequency used, viz. 250 kHz, f_c was chosen as 70 kHz, while for the minimum sampling frequency used, viz. 40 kHz, f_c was chosen as 10 kHz.

In addition to the analog anti-aliasing filter, a very sharp digital low-pass filter with a cutoff frequency also equal to f_c was implemented after digitization in order to remove any traces from frequencies higher than f_c. Hence Δf_{det} was effectively set by the value of f_c, having a maximum value of 70 kHz, a minimum value of 10 kHz, and tunable in steps of 10 kHz.

5.3. Operation Modes

The demonstrated spectrum analyzer featured two possible operation modes which were completely independent of each other: one with a very wide span but a limited resolution bandwidth (RBW), and one with an arbitrarily high RBW but a relatively limited span. One can use the first mode to locate the signal to be analyzed, and the second mode to perform a precise characterization of its spectral structure, for example. The details of both are explained in the next two subsections.

5.3.1. Operation Mode I (Wide-Span Mode)

This mode performs a sweep of the local oscillator frequency and records the square of the detected current at each frequency step, like a classical frequency-swept spectrum analyzer. Its RBW is equal to $2\Delta f_{det}$ due to the ambiguity existing between positive and negative frequency differences, i.e. it is impossible to distinguish if $\omega_{cw} > \omega_{THz}$ or if $\omega_{THz} > \omega_{cw}$ after the signal is detected. Thus, the value of the RBW can only be tuned between 20 kHz and 140 kHz in steps of 20 kHz, as dictated by the anti-aliasing filter. The frequency span is tunable to any range between 50 GHz and 90 GHz. The frequency step size guaranteeing full spectral resolution is $2\Delta f_{det}$. However, it is also possible to undersample the spectrum by taking frequency steps much bigger than $2\Delta f_{det}$ in order to analyze broadband signals in a shorter sweep time. It is also possible to oversample the spectrum by taking steps shorter than $2\Delta f_{det}$ in order to increase the number of acquired frequency points. This allows to apply higher-order video bandwidth (VBW) filters to the captured spectrum to reduce the noise, but it also increases the sweep time.

The minimum sweep time is given by Mt_{st}, where M is the number of frequency steps, and t_{st} the settling time of the RF generator after each frequency change, equal to 11 ms for this generator. In order to further increase the sensitivity, it is also possible to average over several samples at each frequency step, but this increases the measurement time.

5.3.2. Operation Mode II (High-Resolution Mode)

This operation mode keeps the frequency of the local oscillator fixed, while a time trace of the detected signal is acquired by the acquisiton card. A FFT then generates the spectrum, like in spectrum analyzers with a digital IF chain. The RBW is given by f_s/N, f_s being the sampling frequency of the acquisition card, and N the number of acquired points for each measured spectrum. N can be changed at will, allowing an arbitrary resolution bandwidth. In practice, however, the resolution bandwidth limit is determined by the long-term frequency stability of the RF generator, which limits it to around 1 Hz. The ambiguity in the resolution resulting from the impossibility to distinguish between negative and positive frequency differences is rather a soft limit for this mode. It can be easily overcome by first locating the actual frequency of the signal to be analyzed using the smallest RBW of the first mode, and then using this

mode with its maximum span. The maximum span is equal to the maximum Δf_{det}, i.e. 70 kHz. The minimum span is equal to the minimum Δf_{det}, i.e. 10 kHz. The sweep time is equal to N/f_s.

5.4. Measurements

Both operation modes were tested using two different sources emitting around 72 GHz, which is roughly at center of the frequency range of the demonstrated spectrum analyzer. To test operation mode I, the spectrum emitted by a CW terahertz PIN photodiode driven by the TOPTICA TeraScan system [116] was measured. To test operation mode II, the spectrum of a single mode of a terahertz pulse was measured, as with FreSOD. The results for each of the modes are shown in the first two subsections.

5.4.1. Measurements with Operation Mode I

Fig. 5.4 shows the measured spectrum of the sub-terahertz signal emitted by the CW photomixer when driven by the two DFB lasers from the TeraScan system [116], whose temperature and current are kept constant to generate a nominal frequency difference of 73.44 GHz. The settings used for the measurement were the following: the frequency of the local oscillator was swept between 71.92 and 72.08 GHz in 70 kHz steps, and at each step an average of 5,000 samples was taken using the maximum Δf_{det} of 70 kHz. Additionally, a VBW filter, implemented as a 13^{th} -order moving average filter, was used after the spectrum was acquired, which was composed of 2,286 frequency points, totaling an acquisition time of 10 minutes. The signal was not centered around 73.44 GHz, but around 72.02 GHz. It also drifted over time, as shown by the spectrogram of Fig. 5.5, recorded also with the demonstrated spectrum analyzer. Offsets and drifts of this order are indeed expected, as the lasers temperature and current settings are obtained from a look-up table that has no feedback mechanism.

To determine the sensitivity limits of this operation mode, the power of the sub-terahertz signal was varied by changing the voltage applied to the CW terahertz photodiode while keeping the rest of the measurement settings the same. Afterwards, the emitted power was measured for each of the applied voltages using the same calibrated pyroelectric detector used in the characterization of Chapter 3. The measured results, together with a linear fit, are shown in Fig. 5.6. The maximum detected power was 130 μW, corresponding to the spectrum shown in Fig. 5.4. Given that the spectral shape was found to be Gaussian with a 3-dB linewidth of 2.86 MHz, the maximum peak spectral density measured with this mode corresponded to 40 pW/Hz. The minimum detected power was 3 μW, corresponding to a minimum measured peak spectral density of around 980 fW/Hz. There was negligible saturation within the investigated power range, as the comparison with the linear fit shows. The 1 dB compression point was approximately at the highest measured power of 130 μW.

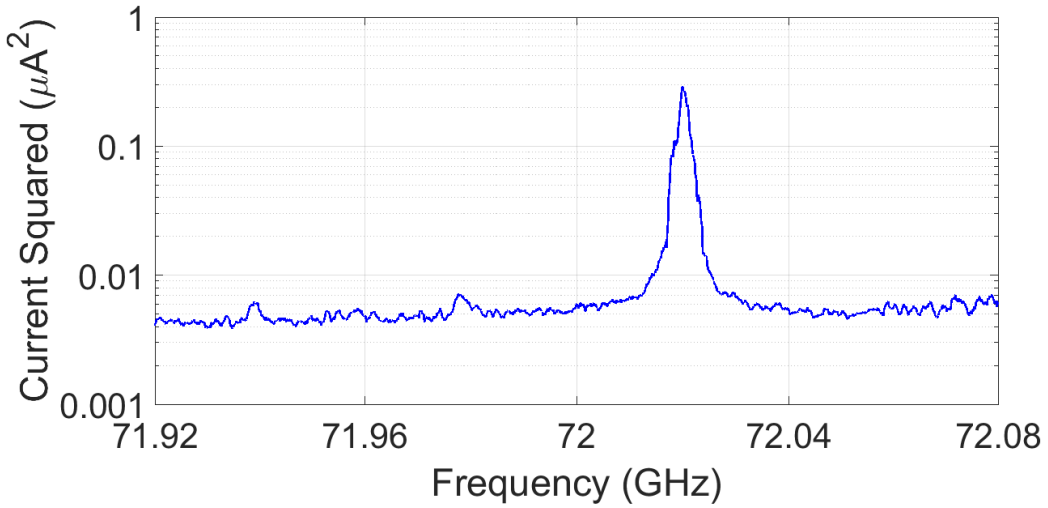

Figure 5.4.: Square of the detected current reproducing the spectrum of the signal emitted by the CW terahertz photodiode. Span: 160 MHz. Reproduced from [122] under a creative commons licence.

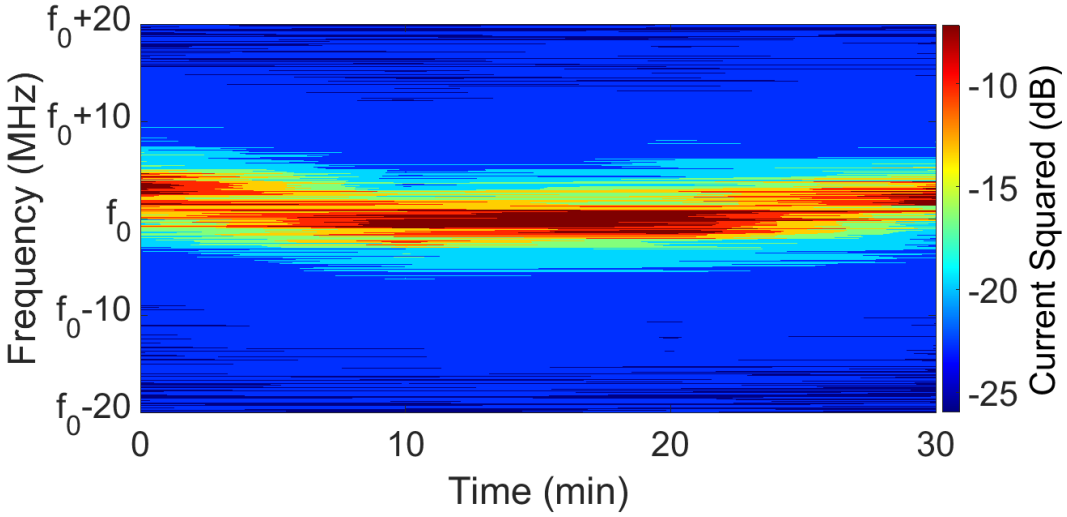

Figure 5.5.: Spectrogram of the signal emitted by the CW terahertz photodiode. The span was reduced to 40 MHz to highlight the frequency stability of the signal. As pointed out in the main text, f_0 = 72,020 MHz, the center frequency of the emitted signal.

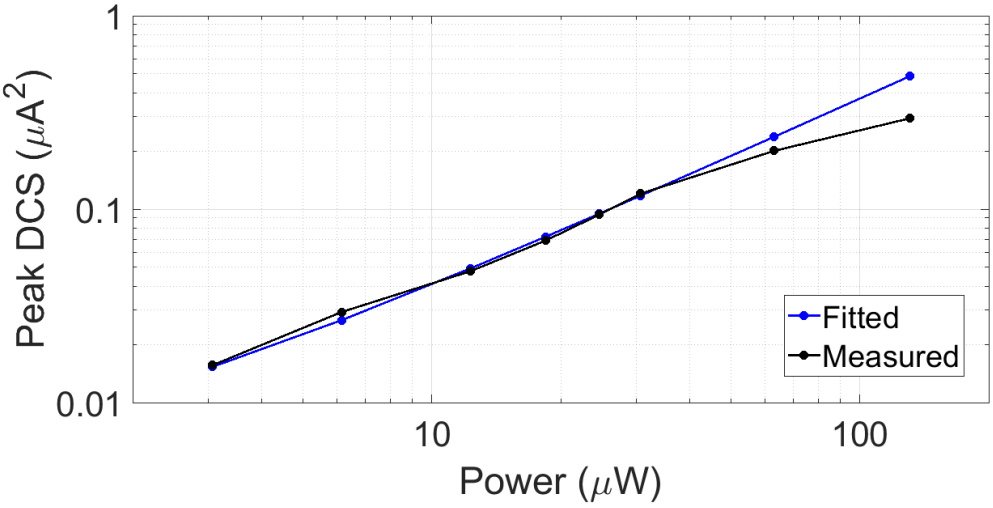

Figure 5.6.: Peak of the detected current squared (DCS) as function of incident power originating from the CW photomixer (black) and its linear fit (blue). Reproduced from [122] under a creative commons licence.

5.4.2. Measurements with Operation Mode II

Fig. 5.7 shows the obtained spectrum when measuring the 721^{st} mode of the terahertz pulse emitted by the same ErAs:In(Al)GaAs pulsed photoconductor described in the previous Chapter. The MLL driving the photoconductor was also the same as the one described in the previous Chapter, viz. a passively-locked fiber laser from Menlo Systems composed of around 83200 modes with average power of 42 mW, mode spacing close to 100 MHz, and pulse duration of less than 90 fs. The bias applied to the photoconductor was also 200 V, therefore, the emitted terahertz power and its distribution were the same as the ones found in Chapter 4.

The settings used in the measurement were the following: the frequency of the local oscillator was set to 72.0195167 GHz, N to 40,000, and f_s to 40 kHz, corresponding to the minimum Δf_{det} of 10 kHz. This resulted in a span of 10 kHz and a RBW of 1 Hz, however, the $1/f$ noise limited the IF range to 1 kHz-10 kHz, resulting in an effective span of 9 kHz. The acquisition of the spectrum took around 1 s, allowing to monitor the spectrum almost in real time. Although the repetition rate of the MLL was not actively stabilized, it showed negligible drift on the measurement time scale, as shown by the spectrogram of Fig. 5.8, recorded also with the demonstrated spectrum analyzer. The actual frequency of the measured mode shown in Fig. 5.7 was determined to be 72.019522086 GHz after using operation mode I to resolve for the frequency ambiguity. This implied an actual repetition rate of 99.888380 MHz, i.e. 111.620 kHz smaller than the nominal repetition rate. This repetition rate was confirmed by simultaneously measuring the second output of the MLL by means of

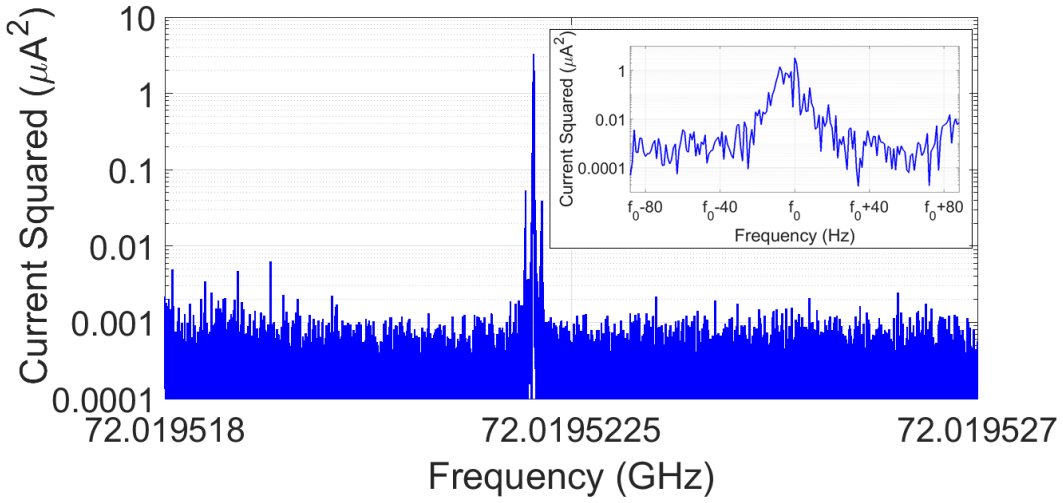

Figure 5.7.: Detected current squared reproducing the spectrum of the 721^{st} mode emitted by the pulsed photoconductor driven by the MLL. Span: 9 kHz. RBW: 1 Hz. The inset shows a magnified view of the spectrum centered at f_0 = 72,019,522,083 Hz. Reproduced from [122] under a creative commons licence.

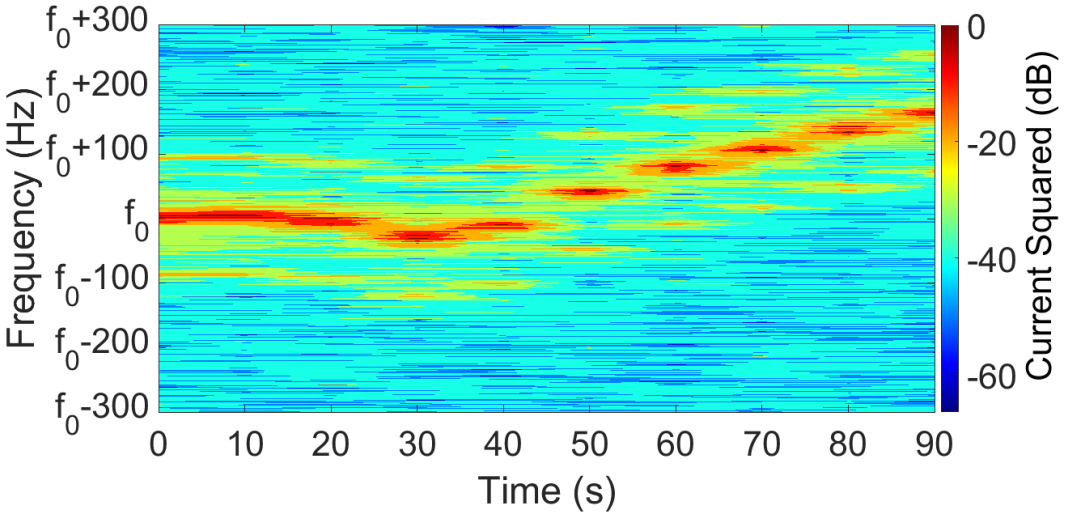

Figure 5.8.: Spectrogram of 721^{st} mode emitted by the pulsed photoconductor driven by the MLL. The span was reduced to 600 Hz to highlight the frequency stability of the signal. f_0 = 72,019,522,083 Hz.

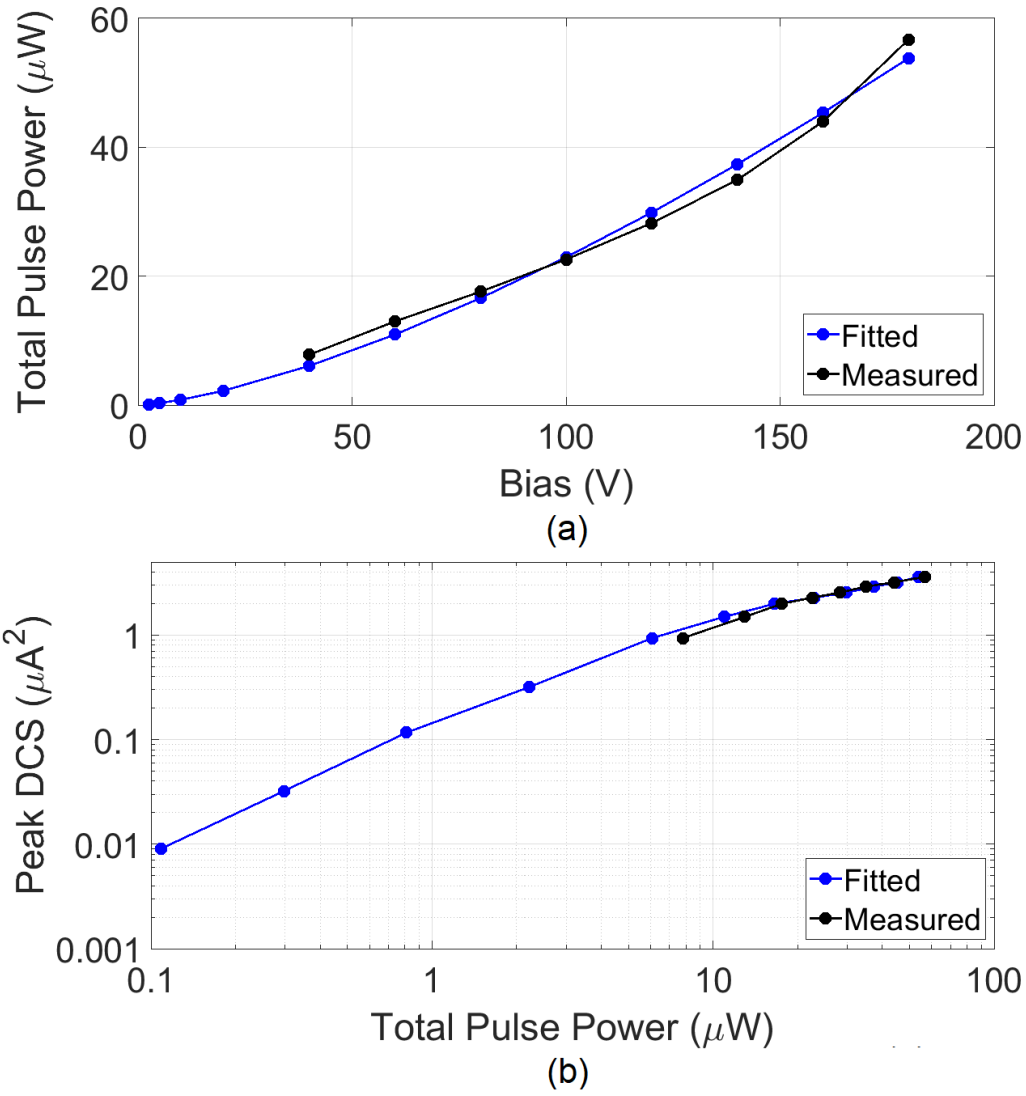

Figure 5.9.: (a) Total pulse power as a function of applied bias (black) and its sub-quadratic polynomial fit (blue). (b) Peak of the detected current squared (DCS) as a function of the measured total pulse power (black), and as a function of the fitted power (blue). Reproduced from [122] under a creative commons licence.

a photodiode and an external electrical spectrum analyzer.

A 3-dB linewidth of 1.14 Hz was found to fit the recorded spectrum, however, this value is the result of the convolution between the local oscillator linewidth, of around 1 Hz, and the linewidth of the 721^{st} mode. Hence, it is only possible to say that the linewidth of the 721^{st} mode is smaller than 1.14 Hz. Determining its actual linewidth

would have required an RF generator with a better phase noise performance, as also pointed out in the previous Chapter. Note that the two side lobes appearing in the spectrum come from the DFB laser used for the local oscillator generation. They can be removed by using a laser with higher side lobe suppression ratio.

Using the total measured pulsed power of 76 μW, and the power spectral distribution presented in the previous Chapter, it is possible to estimate that the average terahertz power in the 721^{st} mode was around 1 nW. However, to determine the true sensitivity limits of this mode, the terahertz power was again varied by changing the voltage applied to the pulsed photoconductor. The results are shown in Fig. 5.9. The black line in Fig. 5.9 (a) shows the average power of the emitted pulse measured with the calibrated pyroelectric detector, which had a noise floor of 1 μW. Hence, in order to obtain the emitted powers below that noise floor, a power-law fitting was used to extrapolate the values at lower biases. Ideally, a pulsed photoconductor shows a quadratic dependence of the emitted power versus applied bias. In reality, due to several nonidealities, that dependence is sub-quadratic. Therefore, the fit, represented by the blue line in Fig. 5.9 (a), resulted in a relationship between total pulse power p_{THz} and bias u given by $p_{THz}(u) = 0.02873u^{1.451}$. Fig. 5.9 (b) shows the peak value of the detected signal for the 721^{st} mode versus the total estimated terahertz power. The smallest detected signal was obtained when a bias of 2.5 V was applied to the pulsed photoconductor, resulting in a total estimated power of 100 nW, which corresponds to an estimated power of 400 fW in the 721^{st} mode. This last estimation was also obtained using the power distribution model presented in the previous Chapter. Thus, the smallest recorded peak spectral density was estimated to be smaller than 400 fW/Hz. Note that pulse powers beyond 10 μW already saturate the photoconductor of the spectrum analyzer for this mode.

5.5. Analysis of the Measurement Results

The differences between the sensitivity values obtained for operation mode I and operation mode II can be attributed to the linewidth and to the structure of the analyzed signal in each case. In particular, the lower power required to saturate the spectrum analyzer in operation mode II could have been caused by the influence of all the other modes composing the terahertz pulse in the detection process.

It is worth noticing that the calculated power in the 721^{st} mode is an estimate that depends on the simplistic theoretical model introduced in Chapter 2, and on the conservative assumptions made in Chapter 4, in particular, on the assumptions about propagation losses. A comparison with the NEP values obtained in Chapter 3 indicates that, indeed, one would expect the sensitivity to be in the fW level, but tending towards the tens of fW, not towards the hundreds of fW. However, the characterization presented in Chapter 3 was done using the photoconductive mixer in a coherent detection scheme. Moreover, only a single frequency tone was incident on the mixer at a time. Both factors could have played a role in the discrepancy.

To conclude this section, Table 5.1 presents a comparison between the results

Spectrum Analyzer	**Nominal Frequency Coverage**	**Frequency Scalability**	**Wideband Signal Analysis**	**Minimum Detectable Power with 1 Hz RBW**
Stand-alone spectrum analyzer [137]	2 Hz-90 GHz	Not possible without extenders	Possible	Not specified
VDI frequency extenders [135]	50-90 GHz (using 2 extenders and an external high-end analyzer)	Up to 1500 GHz (using 8 extenders and an external high-end analyzer)	Possible	1 aW (from 50 to 750 GHz)
RPG Radiometer Physics frequency extenders [136]	50-90 GHz (using 2 extenders and an external high-end analyzer)	Up to 500 GHz (using 6 extenders and an external high-end analyzer)	Possible	Not specified
MLL-based optoelectronic spectrum analyzer [140]	50-1600 GHz (using an external analyzer)	Not possible	Not possible	26 nW (at 99 GHz)
This thesis	50-90 GHz (using wideband EOMs and an additional) optical filter)	Up to 1 THz	Possible	400 fW (at 72 GHz)

Table 5.1.: Comparison between different commercially-available and non-commercially available spectrum analyzers and the one demonstrated here. Reproduced from [122] under a creative commons licence.

obtained with the demonstrated spectrum analyzer, and the ones obtained with other commercially available and non-commercially available spectrum analyzers. Compared to the stand-alone commercial spectrum analyzer in [137], the main advantage of the analyzer presented here is its frequency scalability. It is relatively easy and less expensive to modify the EO-based CW local oscillator subsystem to increase its coverage up to 1 THz [133] (by implementing EOMs with wider bandwidths, by cascading more phase-locked EOMs, or by utilizing the mixing product of positive and negative side lobes through the use of an additional filter), than to add the required amount of frequency extenders to the stand-alone spectrum analyzer to achieve that same coverage. Compared to the commercially available spectrum analyzers based on frequency extenders presented in [135, 136], the main advantage of the one demonstrated here is its superior phase-noise performance, as explained in the introduction. Finally, when compared to the non-commercially available MLL-based optoelectronic spectrum analyzer presented in [140], the two main advantages of the one demonstrated here are the possibility of analyzing wideband signals composed of several frequency tones and the increased sensitivity. From the results presented in Chapter 3, one can infer that this increased sensitivity, and in general, the performance of the photoconductive mixer subsystem, would remain the same up to 400 GHz.

5.6. Conclusions and Outlook

A new optoelectronic spectrum analyzer architecture with a Hz-level resolution and an estimated sensitivity of 400 fW/Hz has been demonstrated in this Chapter. An important difference with respect to other implemented architectures is that the one demonstrated here is neither an extension to an existing spectrum analyzer, nor does it require an external spectrum analyzer to operate. Hence, it is a true optoelectronic analyzer.

Although the demonstrated frequency coverage spanned only 40 GHz, i.e. from 50 GHz to 90 GHz, the presented architecture can be easily modified to cover at least 140 GHz by incorporating an additional non-tunable filter in the 2^{nd} branch of the subsystem for local oscillator generation, although the EO modulation would then need to take place before the branching point. Non-tunable optical filters, in particular fiber-Bragg gratings, are very narrow-band, inexpensive and easily available. Thus, their incorporation would be the simplest way to extend the frequency coverage of the analyzer. Other modifications that would allow to extend the frequency coverage are the use of more cascaded EOMs or the use of wider-bandwidth models. These modifications will enable the demonstrated architecture to be competitive with existing commercial options.

An important issue that needs further research is the emergence of additional harmonics when the photoconductive mixer starts to operate under the large-signal regime. This needs to be experimentally characterized in future implementations in order to establish the spurious-free dynamic range of this type of architecture.

6. Conclusion and Outlook

The contributions contained in this thesis can can be divided into two categories: contributions related to the modelling of short carrier-lifetime photoconductive mixers, and contributions related to the development of new applications with such mixers.

Most of the contributions related to the modelling are discussed in Chapter 2 and 3, and can be summarized as follows:

1. The operation of short carrier-lifetime photoconductive mixers can be modelled making use of two general conservation equations: a charge conservation equation and energy conservation equation. Both of them can be applied for any kind of operation regime.

2. The CW regime can be treated as particular case of the pulsed regime, given that the pulse is periodic. Under this view, a terahertz pulse can be modelled as a collection of discrete frequency modes, and the CW regime is what arises when only two modes are present: a DC mode and a single AC terahertz mode.

3. The use of both conservation equations and the fact that a terahertz pulse can be treated as a collection of discrete frequency modes allows to model the resistance of a photoconductive emitter operating under the pulsed regime as a frequency-dependent quantity, a feat that is not possible using other models. This, in turn, permits a detailed estimation of the power distribution in the terahertz pulse emitted by a photoconducive mixer attached to an antenna. Such estimation has proven to give reasonable results, as demonstrated by the measurements presented in this thesis.

4. The complete modelling of photoconductive mixers acting as terahertz detectors involves the solution of the full partial differential equation that arises from the charge continuity equation. For a small incident terahertz field, an approximate solution that assumes that the carrier dynamics is not affected by the incident field renders good results. However, for large incident fields, such assumption does not capture the full carrier dynamics. In particular, it does not accurately predict the amount of harmonics generated in the detection process, as early experimental results show. For this reason, two operation regimes have been defined for photoconductive detectors: a small-signal operating regime, and a large-signal operation regime. Only the first one has been treated in this thesis.

5. Noise in short carrier-lifetime photocondutive detectors, pumped by significant amounts of laser power, does not only have a thermal origin. An additional

source of noise arises due to the interplay between the random recombination events and the laser intensity fluctuations, as supported by the measurements presented in this thesis.

6. The minimum terahertz power than can be detected with photoconductive mixers when using a 1 Hz detection bandwidth is as low as 1.8 fW at 0.189 THz, and as low as 1 pW at 1 THz.

Some of these findings still require more experimental and theoretical work, in particular. One of the most urgent research questions, for example, is the quantitative definition of small-signal and large-signal operation regions.

Another point yet to be investigated is the influence that the performance of the particular pair of lasers used to drive the photoconductive detector can have on its noise floor. It would be especially interesting to investigate if using squeezed states of light instead of light in normal coherent states, as used here, can have a significant impact. Such research can result in interesting links between quantum optics and terahertz science and technology.

The contributions related to the development of new applications are discussed in Chapter 4 and 5. They include a novel technique for the detection of terahertz pulses and a new architecture for a truly optoelectronic spectrum analyzer.

The novel detection technique for terahertz pulses, coined FreSOD, allows to selectively resolve each of the individual modes composing the pulse with a resolution on the Hz level. This is an increase of several orders of magnitude compared to the resolutions achieved with time-domain detection techniques. Moreover, it does not require a mechanical delay stage or complex synchronization electronics between two MLLs. In its simplest form, which already allows ultra high-resolution spectroscopic measurements, it just requires two tunable narrow-linewidth CW lasers and a CW photocondutive detector. In its more sophisticated form, which allows the phase noise characterization of the individual terahertz modes composing the pulse, it requires an EO-based CW system. The latter is perhaps one of the most interesting applications of this technique, since it can allow to determine the fundamental stability limits of passively-locked MLLs. For this, EO-based CW systems with linewidths much smaller than 1 Hz and stabilities better than 0.33 Hz/s are required, since the first hundreds of modes are much more stable than that, as demonstrated by the results shown in Chapter 4.

The demonstrated optoelectronic spectrum analyzer is possibly the application of photoconductive mixers with the highest potential for commercial exploitation, given its capability to replace the sets of expensive frequency extenders required by current sub-terahertz spectrum analyzers, and the easiness with which one can already perform extremely useful measurements. Moreover, the EO-based architecture presented here can offer a superior phase noise performance compared to the one exhibited by frequency extenders. However, additional development work is still required to make it a viable option than can effectively compete with existing commercial solutions. For example, increasing the frequency coverage by either using

additional optical filters, different EOM models or by using different types of local oscillators subsystems which are not entirely based on EO generation but that also offer very low linewidths e.g. [146].

Finally, there are two further technological developments that are still required to make any terahertz application based on photoconductive detectors competitive:

1. Higher system integration. In particular, integration of the sophisticated laser systems required for photomixing in compact photonic integrated circuits. Efforts in that direction have already been realized [147], but the availability and the performance of such photonic circuits does not yet compare with the ones achieved by the relatively bulky laser systems used in most benchmarking terahertz applications.

2. Increased detection bandwidths. This has been one of the most challenging tasks to implement in photoconductive detectors, given the limited availability of high-bandwidth TIAs, and electromagnetic interference problems associated with the design of simple packaging structures. Some work has been done in this direction already [148, 149], but the obtained results are not satisfactory yet.

In conclusion, even though a lot has been achieved in the field of photocondutive mixers, there is even more that needs to be done, both in terms in fundamental research and in terms of technology development.

A. Appendix 1: Fabrication of ErAs:In(Al)GaAs Photoconductive Mixers

In its most simplified version, the fabrication consisted of ten steps:

1. Antenna and electrode structure lithography:

   Once a quartz mask containing the desired antenna and electrode structure has been fabricated, a 7 × 8 mm sample of the ErAs:In(Al)GaAs photoconductor, grown on a 500-μm InP:Fe substrate wafer, is cleaved out from the wafer to imprint on it the desired structures via contact lithography.

   Since the electrode structures can be as narrow as 1 μm, a good contact is critical in this step. Hence, a very thin and uniform layer of AZ 5414E is deposited on the sample by spin coating it at 8000 rpm. A first litographic step to remove a 1-mm wide frame of photoresist from the sample is then carried out, leaving a 6 × 7 mm square of photoresist after developing the sample with AZ MIF 726. This square, called active area, is where all the fabricated mixers will reside. This first step just helps to achieve a good contact between the quartz mask and the active area during the second lithographic step, since it removes the photoresist edge irregularities that result from spin coating.

   Afterwards, the sample is heated at 120 °C for 1 minute to transform the AZ 5414E from positive to negative, and the second lithographic step is performed, in which the antenna and the electrode structures are patterned. The surfaces that will form such such structures on the saple are then exposed.

2. Metal deposition:

   The sample is dipped in a 1:1 solution of H_2O and HCl for 30 seconds in order to remove the native oxide of the InGaAs cap layer of the sample. This greatly enhances the adhesion of the deposited metal. A 0.04-μm layer of Titanium is then deposited by electron beam evaporation, followed by the deposition of a 0.2-μm layer of gold by simpl evaporation.

   After the metal deposition is completed, the sample is dipped in acetone for 15 minutes to remove the photoresist from the non-metallized areas.

3. Annealing:

   The sample is annealed at 420 °C in a nitrogen atmosphere for 1 minute to improve the quality of the contact between the photoconductor and the metal.

4. Mesa lithography: A thick layer of AZ 1518 of photoresist is deposited on sample by spin coating it at 4000 rpm. A protective photoresist layer covering the antenna and the electrode structure is then patterned via lithography and subsequent developing.

5. Mesa etching:

   The thin ErAs:In(Al)GaAs photocondutive material is etched from the areas that were not protected by the photoresist layer, leaving the semi-insulating InP:Fe substrate exposed in those areas.

6. Antireflection coating deposition:

   A SiN layer is grown on top of the sample by plasma-enhanced chemical vapor deposition. The thickness of the layer is chosen to minimize optical reflections. In addition to improve optical coupling, this layer helps to protect the photoconductive material from oxidation and other sources of contamination.

7. Antireflection coating litography:

   Another thick layer of AZ 1518 of photoresist is deposited on the sample by spin coating it at 4000 rpm. A protective photoresist layer covering only the electrode structure is then patterned via lithography and subsequent developing.

8. Antireflection coating etching:

   The SiN layer is etched out from the areas that were not protected by the photoresist, exposing the contacting metal pads attached to the antenna. The etching is done via reactive ion etching with CF_4.

9. Cleaving:

   Each individual mixer in the the 7×8 mm sample is cleaved out to be used separately from the rest.

10. Bonding:

    Each of the cleaved devices is then bonded, through the contacting pads, to an electrical connector.

B. Acronyms

AC	Alternating current
CPS	Coplanar stripline
CMOS	Complementary metal–oxide–semiconductor
CW	Continuous-wave
DC	Direct current
DFB	Distributed Brag reflector
DFB	Distributed feedback
DNR	Dynamic range
EDFA	Eribum-doped fiber amplifier
EM	Electromagnetic
EO	Electo-optic
EOM	Electo-optic phase modulator
FFT	Fast Fourier transform
FWHM	Full width at half maximum
IF	Intermediate frequency
MLL	Mode-locked laser
NEP	Noise equivalent power
RF	Radio frequency
SIS	Superconductor-insulator-superconductor
TIA	Transimpedance amplifier

RMS	Root mean square

C. List of Own Publications

Journal Publications

- A.D.J. Fernandez Olvera et al. “Continuous-wave 1550 nm operated terahertz system using ErAs:In(Al)GaAs photo-conductors with 52 dB dynamic range at 1 THz”. In: *Optics Express* 25.23 (2017), pp. 29492–29500. DOI: 10.1364/OE.25.029492.

- A.D.J. Fernandez Olvera et al. “International system of units (SI) traceable noise-equivalent power and responsivity characterization of continuous wave ErAs:InGaAs photoconductive terahertz detectors”. In: *Photonics* 6.1 (2019). DOI: 10.3390/PHOTONICS6010015.

- A.D.J. Fernandez Olvera et al. “Frequency selective optoelectronic downconversion of a terahertz Pulse using ErAs:In(Al)GaAs photoconductors”. *IEEE Access* 9 (2021), pp. 95391–95400. DOI: 10.1109/ACCESS.2021.3094358.

- A.D.J. Fernandez Olvera, B.L. Krause, and S. Preu. “A true optoelectronic spectrum analyzer for millimeter waves with Hz resolution”. *IEEE Access* 9 (2021), pp. 114339–114347. DOI: 10.1109/ACCESS.2021.3105030.

- A.D.J. Fernandez Olvera, A.K. Mukherjee , and S. Preu. “A fully optoelectronic continuous-wave 2-port vector network analyzer operating from 0.1 THz to 1 THz”. *IEEE Journal of Microwaves* 1.4 (2021), pp. 1015 -1022. DOI: 10.1109/JMW.2021.3107472.

International Conference Proceedings

- A.D.J. Fernandez Olvera et al. “Dispersive properties of self-complementary antennas in pulsed THz systems”. In: *42nd International Conference on Infrared, Millimeter, and Terahertz Waves (IRMMW-THz)* (Cancun, Mexico). IEEE, August 2017.

- A.D.J. Fernandez Olvera et al. “Architecture and component characterization of a high-resolution free-space vector network analyzer for the terahertz range”. In: *2019 European Microwave Conference in Central Europe (EuMCE)* (Prague, Czech Republic). IEEE, May 2019.

- A.D.J. Fernandez Olvera et al. “W-Band heterodyne wireless system with 2.3 GHz intermediate frequency driven entirely by ErAs:In(Al)GaAs photoconductors”. In: *21st International Conference on Transparent Optical Networks (ICTON)* (Angers, France). IEEE, July 2019.

- A.D.J. Fernandez Olvera et al. "Continuous-wave electro-optic Terahertz dual-comb operating from 0.096 to 0.496 THz using ErAs:In(Al)GaAs photoconductors". In: *44th International Conference on Infrared, Millimeter, and Terahertz Waves (IRMMW-THz)* (Paris, France). IEEE, September 2019 **(Keynote Talk)**.

D. Acknowledgments

I was born in a small town in the Gulf of Mexico during the end of the eighties. My paternal grandfather was a local fisherman. My maternal grandmother was school janitor. I never met my maternal grandparents. They both died when my mom was still a teenager, leaving her alone with two smaller siblings. Yet, both of my parents managed to go to college and finish their degrees. Although an important part of their of success was the amount of effort they put in, another important part was the the people that were around them, always willing to help. My point with this is that success is never the result of an individual effort--how sad it would be if it were like that-- but the result of a collective one. So, in this section, I would like to thank all the people who helped me (consciously or unconsciously) throughout these years. My success, if any, is also yours.

First of all, I would like to thank Prof. Dr. Sascha Preu, or as we know him, Sascha. Thanks for the trust, the time, and for all the patience throughout these years. I know I was a disaster in the lab and in the clean room when I arrived. I still remember the day in which I ruined an alpha sample for dry etching it for more than 15 mins! I thought I was going to get kicked out, but you still believed in me. I hope I didn't disappoint you at the end. From my side, I can only say that I have enjoyed these years as your student. I have really learned a lot, and not only about science. I will always admire the way you manage your time, the importance that you give to your family, and how you treat everyone inside and outside the lab. This is hard to find in academia these days.

Secondly, I would like to thank all my colleagues in the terahertz lab and in the CELTA consortium. Mario, you taught me many of the tricks in the lab and in the clean room at the very beginning, and also shared all your recipes and calibration routines. Thanks for that. Stefan, thanks for all your efforts to try to make me a more organized and tidy colleague. Your were always the german spirit of this lab. Uttam, you were always there to discuss any idea, whether it was related to terahertz or not. I honestly don't know which discussion were more fun, but I do know that you were the best office mate I could ever had. I hope you continue being that transparent and curious. Those traits are becoming scarce nowadays. Also, thanks for all the biryani evenings. Fahd, thanks for all your good vibes and your willingness to always try something new, either for lunch or just for fun, and also for the occasional beer here and there. Amlan, thanks for all your smart points of view when discussing a problem, it usually made consider things I had not thought of. Thanks also for the nice evenings at your place and the debates during lunch. Benedikt, thanks for your support in the lab during the last year, it made the last experiments much easier and enjoyable. Frederik, thanks for all the good advice and the parties in Madrid. It

was always a pleasure to talk to you and to work in the lab with you. Rahul, thanks for your neverending optimism and enthusiasm to organize stuff.

Thirdly, I would like to thank my friends from the Netherlands, who were always there when I needed to feel at home in Europe. Ruben, thanks for always allowing me to stay in your place whenever I was back in Eindhoven. The parties that we had there were always the best. Edgar, thanks for keeping alive my interest in social sciences and politics with your views. Rodrigo, thanks for your nice recommendations on music, podcasts and culture, in general. Stefanos, thanks for the nice scientific and philosophical discussions. Talking to you always motivate me to achieve more.

Last but not least, I would like to thank my family in Mexico. Alan, whenever I went back to Mexico, it was like if time had not passed. It really makes feel like if we were in high-school again. Talking to you over the phone always made me feel better. Tomas, thanks for all the musical influence and the interesting ideas thorough these years, you have always been beacon for me. Luis Alberto, thanks for always being there and visiting me whenever I was in Mina. I think it was one of the reasons I kept going. I do not know what will happen now that you are not there anymore. Fred, Faride and Mom, thanks for all the support through the years, being with you is one of the few things that makes feel alive, and one of the things that keeps me going. I would have never become what I am without you, specially without you Mom. I have no words to thank all the efforts, sacrifices, and all the things you gave up for us. You taught me one of the most important lessons in life: to never give up in the face of adversity, and that efforts are always rewarded. I hope to become as resilient as you someday.

Finally, Dorely, thank you for these last years. Thanks for listening to me everyday after work. I think by now you're as fed up with the thesis as I am, but I would not have managed to finish without you.

"No sólo no hubiera sido nada sin ustedes, sino con toda la gente que estuvo a mi alrededor desde el comienzo; algunos siguen hasta hoy. !'Gracias totales!"

Bibliography

[1] T. Nagatsuma, G. Ducournau, and C.C. Renaud. ''Advances in terahertz communications accelerated by photonics''. In: *Nature Photonics* 10.6 (2016), pp. 371–379. DOI: 10.1038/NPHOTON.2016.65.

[2] W. Hong et al. ''The role of millimeter-wave technologies in 5G/6G wireless communications''. In: *IEEE Journal of Microwaves* 1.1 (2021), pp. 101–122. DOI: 10.1109/JMW.2020.3035541.

[3] A.I. McIntosh et al. ''Terahertz spectroscopy: a powerful new tool for the chemical sciences?'' In: *Chemical Society Reviews* 41.6 (2012), pp. 2072–2082. DOI: 10.1039/C1CS15277G.

[4] J.C. Pearson, B.J. Drouin, and S. Yu. ''Instrumentation for THz spectroscopy in the laboratory and in space''. In: *IEEE Journal of Microwaves* 1.1 (2021), pp. 43–54. DOI: 10.1109/JMW.2020.3032454.

[5] M. Naftaly, N. Vieweg, and A. Deninger. ''Industrial applications of terahertz sensing: State of play''. In: *Sensors* 19.19 (2019). DOI: 10.3390/S19194203.

[6] G. Valusis et al. ''Roadmap of terahertz imaging 2021''. In: *Sensors* 12 (2021). DOI: 10.3390/S21124092.

[7] C.E. Shannon. ''Communication in the presence of noise''. In: *Proceedings of the IRE* 37.1 (1949), pp. 10–21. DOI: 10.1109/JRPROC.1949.232969.

[8] European Space Agency. *Herschel Science Instruments*. 2021. URL: https://www.cosmos.esa.int/web/herschel/science-instruments.

[9] M. Küppers et al. ''Localized sources of water vapour on the dwarf planet (1) Ceres''. In: *Nature* 505 (2014), pp. 525–527. DOI: 10.1038/NATURE12918.

[10] C.J. Strachan et al. ''Using terahertz pulsed spectroscopy to quantify pharmaceutical polymorphism and crystallinity''. In: *Journal of Pharmaceutical Sciences* 94.4 (2005), pp. 837–846. DOI: 10.1002/JPS.20281.

[11] A. Giles Davies et al. ''Terahertz spectroscopy of explosives and drugs''. In: *Materials Today* 11.3 (2008), pp. 18–26. DOI: 10.1016/S1369-7021(08)70016-6.

[12] Teraview. *TeraCota - Terahertz Coating thickness analysis*. 2021. URL: https://teraview.com/teracota/.

[13] Luna. *Luna Terahertz Sensors and Gauges Provide Blow Molding and Other Process Control Insights*. 2021. URL: https://lunainc.com/blog/luna-terahertz-sensors-and-gauges-provide-blow-molding-and-other-process-control-insights.

[14] Lytid. *TeraEyes-Highly Versatile TeraHertz Imaging System*. 2021. URL: https://lytid.com/imaging-system/.

[15] Swiss Terahertz. *RIGI Camera*. 2021. URL: https://www.swissterahertz.com/rigicamera.

[16] Lytid. *TeraCascade 2000 Series*. 2021. URL: https://lytid.com/products/terahertz/teracascade2000/.

[17] TeraSense. *Terahertz sources*. 2021. URL: https://terasense.com/products/terahertz-sources/.

[18] X. Mei et al. ''First demonstration of amplification at 1 THz using 25-nm InP high electron mobility transistor process''. In: *IEEE Electron Device Letters* 36.4 (2015), pp. 327–329. DOI: 10.1109/LED.2015.2407193.

[19] M. Seo et al. ''InP HBT IC technology for terahertz frequencies: Fundamental oscillators up to 0.57 THz''. In: *IEEE Journal of Solid-State Circuits* 46.10 (2011), pp. 2203–2214. DOI: 10.1109/JSSC.2011.2163213.

[20] Z. Hu, M. Kaynak, and R. Han. ''High-power radiation at 1 THz in silicon: A fully scalable array using a multi-functional radiating mesh structure''. In: *IEEE Journal of Solid-State Circuits* 53 (5 2018). DOI: 10.1109/JSSC.2017.2786682.

[21] B. Khamaisi, S. Jameson, and E. Socher. ''0.61 THz radiating source with on-chip antenna on 65nm CMOS''. In: *11th European Microwave Integrated Circuit Conference* (London, United Kingdom). IEEE, Oct. 2016.

[22] A. Ahmad, M. Lee, and K.O. Kenneth. ''1.4 THz, -13dBm-EIRP frequency multiplier chain using symmetric- and asymmetric-CV varactors in 65nm CMOS''. In: *2016 IEEE International Conference on Solid-State Circuits* (San Francisco, United States of America). IEEE, Jan. 2016.

[23] A. El Fatimy et al. ''AlGaN/GaN high electron mobility transistors as a voltage-tunable room temperature terahertz sources''. In: *Journal of Applied Physics* 107.2 (2010). DOI: 10.1063/1.3291101.

[24] T. Onishi, T. Tanigawa, and S. Takigawa. ''High power terahertz emission from a single gate AlGaN/GaN field effect transistor with periodic Ohmic contacts for plasmon coupling''. In: *Applied Physics Letters* 97.9 (2010). DOI: 10.1063/1.3486473.

[25] T. Maekawa et al. ''Oscillation up to 1.92 THz in resonant tunneling diode by reduced conduction loss''. In: *Applied Physics Express* 9.2 (2016). DOI: 10.7567/APEX.9.024101.

[26] K.H. Al-Khalidi Alharbi et al. ''Resonant tunneling diode terahertz sources with up to 1 mW output power in the J-band''. In: *IEEE Transactions on Terahertz Science Technology* 10.2 (2020), pp. 150–157. DOI: 10.1109/TTHZ.2019.2959210.

[27] J.L. Hesler and T.H. Crowe. ''NEP and responsivity of THz zero-bias Schottky diode detectors''. In: *32nd International Conference on Infrared and Millimetre Waves* (Cardiff, United Kingdom). IEEE, Sept. 2007.

[28] M. Yahyapour et al. ''A flexible phase-insensitive system for broadband CW-terahertz spectroscopy and imaging''. In: *IEEE Transactions on Terahertz Science and Technology* 6 (5 2016). DOI: 10.1109/TTHZ.2016.2589540.

[29] C. Cojocari et al. ''European Schottky-diode based receiver technology''. In: *44th International Conference on Infrared Millimetre and Terahertz Waves* (Paris, France). IEEE, Sept. 2019.

[30] S. Preu et al. ''An improved model for non-resonant terahertz detection in field-effect transistors''. In: *Journal of Applied Physics* 111.2 (2007). DOI: 10.1063/1.2743400.

[31] M Dyakonov and M. Shur. ''Detection, mixing, and frequency multiplication of terahertz radiation by two-dimensional electronic fluid''. In: *IEEE Transactions on Electron Devices* 43.3 (1996), pp. 380–387. DOI: 10.1109/16.485650.

[32] A. Soltani et al. ''Direct nanoscopic observation of plasma waves in the channel of a graphene field-effect transistor''. In: *Light: Science & Applications* 9 (2020). DOI: 10.1038/S41377-020-0321-0.

[33] K. Ikamas et al. ''Broadband terahertz power detectors based on 90-nm silicon CMOS transistors with flat responsivity Up to 2.2 THz''. In: *IEEE Electron Device Letters* 39.9 (2018), pp. 1413–1416. DOI: 10.1109/LED.2018.2859300.

[34] M.W Ryu et al. ''High-Performance plasmonic THz detector based on asymmetric FET with vertically integrated antenna in CMOS technology''. In: *IEEE Transactions on Electron Devices* 63.4 (2016), pp. 1742–1748. DOI: 10.1109/TED.2016.2526677.

[35] T.Y. Chang, T.J. Bridges, and E.G. Burkhardt. ''CW submillimiter laser action in optically pumped methyl flouride, methyl alcohol and vinyl chloride gases''. In: *Applied Physics Letters* 17.6 (1970), pp. 249–251. DOI: 10.1063/1.1653386.

[36] D. Pereira et al. ''A review of optically pumped far-infrared laser lines from methanol isotopes''. In: *International Journal of Infrared and Millimeter Waves* 15 (1994), pp. 1–44. DOI: 10.1007/BF02265874.

[37] P. Chevalier et al. ''Widely tunable compact terahertz gas lasers''. In: *Science* 366.6467 (2019), pp. 856–860. DOI: 10.1126/SCIENCE.AAY8683.

[38] J. Faist et al. ''Quantum cascade laser''. In: *Science* 264.5158 (1994), pp. 553–556. DOI: 10.1126/SCIENCE.264.5158.553.

[39] B.S. Williams et al. ''Terahertz quantum-cascade laser at $\lambda = 100$ μm using metal waveguide for mode confinement''. In: *Applied Physics Letters* 83.11 (2003). DOI: 10.1063/1.1611642.

[40] C. Walther et al. ''Quantum cascade lasers operating from 1.2 to 1.6 THz''. In: *Applied Physics Letters* 91.13 (2007). DOI: 10.1063/1.2793177.

[41] A. Khalatpour et al. ''High-power portable terahertz laser systems''. In: *Nature Photonics* 15 (2021), pp. 16–20. DOI: 10.1038/S41566-020-00707-5.

[42] D. Rosenthal et al. ''Stressed Ge:Ga detector arrays for PACS and FIFI LS''. In: *Far-IR, Sub-Millimeter & Millimeter Detector Technology Workshop* (Monterey, United States of America). Apr. 2002.

[43] B. Billade, A. Pavolotsky, and V. Belitsky. ''An SIS mixer with 2hf/k DSB noise temperature at 163-211 GHz band''. In: *IEEE Transactions on Terahertz Science and Technology* 3.4 (2013), pp. 416–421. DOI: 10.1109/TTHZ.2013.2255734.

[44] J. Zmuidzinas and P.L. Richards. ''Superconducting detectors and mixers for millimeter and submillimeter astrophysics''. In: *Proceedings of the IEEE* 92.10 (2004), pp. 1597–1616. DOI: 10.1109/JPROC.2004.833670.

[45] J.R. Tucker. ''Quantum limited detection in tunnel junction mixers''. In: *IEEE Journal of Quantum Electronics* 15.11 (1979), pp. 1234–1258. DOI: JQE.1979.1069931.

[46] I. Wilke and S. Sengupta. ''Nonlinear optical techniques for terahertzpulse generation and cetection—optical rectification and electrooptic sampling''. In: *Terahertz spectroscopy. Principles and applications*. Ed. by S.L. Drexheimer. CRC Press, 2009, pp. 31–72.

[47] M. Scheller et al. ''Room temperature continuous wave milliwatt terahertz source''. In: *Optics Express* 26 (2010), pp. 27112–27117. DOI: 10.1364/OE.18.027112.

[48] S.-H. Yang et al. ''7.5% optical-to-terahertz conversion efficiency offered by photoconductive emitters with three-dimensional plasmonic contact electrodes''. In: *IEEE Transactions on Terahertz Science and Technology* 4.5 (2014). DOI: 10.1109/TTHZ.2014.2342505.

[49] B.E.A. Saleh and M.C. Teich. ''Semiconductor photon detectors''. In: *Fundamentals of photonics*. Wiley, 2007, pp. 748–800.

[50] T. Gonazalez Sanchez et al. ''Electric transport in InP under high-electric field condition''. In: *Semiconductor Science and Technology* 7.1 (1991), pp. 31–36. DOI: 10.1088/0268-1242/7/1/006.

[51] L. Liebermeister et al. ''Optoelectronic frequency-modulated continuous-wave terahertz spectroscopy with 4 THz bandwidth''. In: *Nature Communications* 12 (2021). DOI: 10.1038/S41467-021-21260-X.

[52] B.E.A. Saleh and M.C. Teich. ''Beam optics''. In: *Fundamentals of photonics*. Wiley, 2007, pp. 74–100.

[53] W.W. Gärtner. ''Depletion-layer photoeffects in semiconductors''. In: *Physical Review* 116.1 (1959), pp. 84–87. DOI: 10.1103/PhysRev.116.84.

[54] S. Preu et al. ''Principles of THz Generation''. In: *Semiconductor terahertz technology: devices and systems at room temperature operation*. Ed. by G. Carpintero et al. Wiley, 2015, pp. 3–68.

[55] S. Preu et al. ''Efficient terahertz emission from ballistic transport enhanced n-i-p-n-i-p superlattice photomixers''. In: *Applied Physics Letters* 90.3 (2007). DOI: 10.1063/1.2743400.

[56] N.T. Yardimci et al. ''High-power terahertz generation using large-area plasmonic photoconductive emitters''. In: *IEEE Transactions on Terahertz Science and Technology* 5.2 (2015), pp. 223–229. DOI: 10.1109/TTHZ.2015.2395417.

[57] N.T. Yardimci et al. ''A high-responsivity and broadband photoconductive terahertz detector based on a plasmonic nanocavity''. In: *Applied Physics Letters* 113 (2018). DOI: 10.1063/1.5066243.

[58] S.M. Sze and K.K. Ng. ''Physics and properties of semiconductor-A review''. In: *Physics of semiconductor devices*. Wiley, 2007, pp. 7–75.

[59] S. Gupta et al. ''Subpicosecond carrier lifetime in GaAs grown by molecular beam epitaxy at low temperatures''. In: *Applied Physics Letters* 59.25 (1991), pp. 3726–3728. DOI: 10.1063/1.105729.

[60] B. Sartorius et al. ''All-fiber terahertz time-domain spectrometer operating at 1.5 µm telecom wavelengths''. In: *Physics Reports* 16.13 (2008), pp. 9565–9570. DOI: 10.1364/OE.16.009565.

[61] E.R. Brown, F.W. Smith, and K.A. McIntosh. ''Coherent millimiter-wave generation by heterodyne conversion in low-temperature-grown GaAs photoconductors''. In: *Journal of Applied Physics* 73.3 (1993), pp. 1480–1483. DOI: 10.1063/1.353222.

[62] M Wollenhaupt, A. Assion, and T. Baumert. ''Femtosecond laser pulses: Linear properties, manipulation, generation and measurement''. In: *Handbook of lasers and optics*. Ed. by A. Träger. Springer Science and Business Media, 2007, pp. 937–983.

[63] S.M. Duffy et al. ''Accurate modeling of dual dipole and slot elements used with photomixers for coherent terahertz output power''. In: *IEEE Transactions on Microwave Theory and Techniques* 49.6 (2001), pp. 1032–1038. DOI: 10.1109/22.925487.

[64] I.S. Gregory et al. ''Optimization of photomixers and antennas for continuous-wave terahertz emission''. In: *IEEE Journal of Quantum Electronics* 41.5 (2005), pp. 717–728. DOI: 10.1109/JQE.2005.844471.

[65] I.S. Gregory et al. ''Analysis of photomixer receivers for continuous-wave terahertz radiation''. In: *Applied Physics Letters* 91.15 (2007), p. 154103. DOI: 10.1063/1.2789709.

[66] C.W. Berry and M. Jarrahi. ''Principles of impedance matching in photoconductive antennas''. In: *Journal of Infrared Millimeter and Terahertz Waves* 33 (2012), pp. 1182–1189. DOI: 10.1007/S10762-012-9937-3.

[67] A. Garufo et al. ''Norton equivalent circuit for pulsed photoconductive antennas–part I: Theoretical model''. In: *IEEE Transactions on Antennas and Propagation* 66.4 (2018), pp. 1635–1645. DOI: 10.1109/TAP.2018.2800704.

[68] S. Preu. ''A unified derivation of the terahertz spectra generated by photoconductors and diodes''. In: *Journal of Infrared, Millimeter, and Terahertz Waves volume* 35 (2014). DOI: 10.1007/s10762-014-0096-6.

[69] N.W. Ashcroft and N.D. Mermin. ''The Drude theory of metals''. In: *Solid state physics*. Harcourt College Publishers, 1976, pp. 1–28.

[70] S. Ramo, J.R. Whinnery, and T. Van Duzer. ''Maxwell's equations''. In: *Fields and waves in communications electronics*. Wiley, 1993, pp. 114–162.

[71] C.A. Balanis. ''Fundamental parameters of antennas''. In: *Antenna theory. Analysis and design*. Wiley, 1997, pp. 28–115.

[72] A.W. Love. ''Equivalent circuit for aperture antennas''. In: *Electronic Letters* 23.13 (1987). DOI: 10.1049/EL:19870504.

[73] A.W. Love. ''Comment: On the equivalent circuit of a receiving antenna''. In: *IEEE Antennas and Propagation Magazine* 44.5 (2002). DOI: 10.1109/MAP.2003.1241317.

[74] A.W. Love. ''Comment on "Limitations of the Thevenin and Norton equivalent circuits for a receiving antenna"''. In: *IEEE Antennas and Propagation Magazine* 45.4 (2003). DOI: 10.1109/MAP.2003.1241317.

[75] R.E. Collin. ''Remarks on Comments on the limitations of the Thevenin and Norton equivalent circuits for a receiving antenna''. In: *IEEE Antennas and Propagation Magazine* 43.4 (2003), pp. 99–100. DOI: 10.1109/MAP.2003.1241318.

[76] W. Geyi. ''Derivation of equivalent circuits for receiving antenna''. In: *IEEE Transactions on Antennas and Propagation* 52.6 (2004), pp. 1620–1624. DOI: 10.1109/TAP.2004.829856.

[77] D. Pozar. ''Scattered and absorbed powers in receiving antennas''. In: *IEEE Antennas and Propagation Magazine* 46.1 (2004), pp. 144–145. DOI: 10.1109/MAP.2004.1296172.

[78] H.C. Torrey and C.A. Whitmer. ''Frequency Conversion''. In: *Crystal Rectifiers*. McGraw Hill, 1948, pp. 111–174.

[79] H.E. Rowe. ''Some general properties of nonlinear elements. II. Small signal theory''. In: *Proceedings of the IRE* 46.5 (1958), pp. 850–860. DOI: 10.1109/JRPROC.1958.286938.

[80] N. Wang et al. ''Room-temperature heterodyne terahertz detection with quantum-level sensitivity''. In: *Nature Astronomy* 3 (2019), pp. 977–982. DOI: 10.1038/s41550-019-0828-6.

[81] N. Wang and M. Jarrahi. ''Noise analysis of photoconductive terahertz detectors''. In: *Journal of Infrared, Millimeter, and Terahertz Waves* 34 (2013), pp. 519–528. DOI: 10.1007/s10762-013-9995-1.

[82] R. Zwanzig. ''Brownian motion and langevin equations''. In: *Nonequilibrium statistical mechanics*. Oxford University Press, 2001, pp. 3–23.

[83] K.M. Vliet. ''Noise in semiconductors and photoconductors''. In: *Proceedings of the IRE* 5.6 (1958), pp. 1004–1018. DOI: 10.1109/JRPROC.1958.286839.

[84] H. Nyquist. ''Thermal agitation of electric charge in conductors''. In: *Physical Review* 32.1 (1928). DOI: 10.1103/PHYSREV.32.110.

[85] A.D.J. Fernandez Olvera et al. ''Continuous-wave 1550 nm operated terahertz system using ErAs:In(Al)GaAs photo-conductors with 52 dB dynamic range at 1 THz''. In: *Optics Express* 25.23 (2017), pp. 29492–29500. DOI: 10.1364/OE.25.029492.

[86] G.L. Abbas, V.W.S Chan, and T.K. Yee. ''A dual-detector optical heterodyne receiver for local oscillator noise suppression''. In: *Journal of Lightwave Technology* 3.5 (1985). DOI: 10.1109/JLT.1985.1074301.

[87] H.P. Yuen and V.W.S. Chan. ''Noise in homodyne and heterodyne detection''. In: *Optics Letters* 8.3 (1983), pp. 177–179. DOI: 10.1364/OL.8.000177.

[88] S.E. Hashemi. ''Relative intensity noise (RIN) in high-speed VCSELs for short reach communication''. MA thesis. Chalmers University of Technology, Mar. 2012.

[89] M. Movassaghi. ''Characterization and modeling of erbium-doped fiber amplifiers and impact of fiber dispersion on semiconductor laser noise''. PhD thesis. The University of British Columbia, Oct. 1999.

[90] M. Nazarathy et al. ''Progress in externally modulated AM CATV transmission systems''. In: *Journal of Lightwave Technology* 11.1 (1993). DOI: 10.1109/50.210575.

[91] S. Shin et al. ''Characterization and analysis of relative intensity noise in broadband optical sources for optical coherence tomography''. In: *IEEE Photonics Technology Letters* 22.14 (2010), pp. 1057–1059. DOI: 10.1109/LPT.2010.2050058.

[92] R. Mueckstein et al. ''Near-Field analysis of terahertz pulse generation from photo-excited charge density gradients''. In: *IEEE Transactions on Terahertz Science and Technology* 5.2 (2015), pp. 260–267. DOI: 10.1109/TTHZ.2015.2395389.

[93] G Klatt et al. ''Terahertz emission from lateral photo-Dember currents''. In: *Optics Express* 18.5 (2010), pp. 4939–4947. DOI: 10.1364/OE.18.004939.

[94] M. Navarro-Cia et al. ''Generation of radially-polarized terahertz pulses for coupling into coaxial waveguides''. In: *Scientific Reports* 6 (2016). DOI: 10.1038/SREP38926.

[95] R.E. Burgess. ''Fluctuations of the numbers of electrons and holes in a semiconductor''. In: *Proceedings of the Physical Society. Section B* 68.9 (1955), pp. 661–671. DOI: 10.1088/0370-1301/68/9/311.

[96] K.M. Vliet and J. Blok. ''Electronic noise in semiconductors''. In: *Physica* 22.1-5 (1956), pp. 231–242. DOI: 10.1016/S0031-8914(56)80031-1.

[97] S. Ross. ''Conditional probability and conditional expectation''. In: *Introduction to probability models*. Academic Press, 2014, pp. 94–181.

[98] R. Schnabel. ''Squeezed states of light and their applications in laser interferometers''. In: *Physics Reports* 684 (2017), pp. 1–51. DOI: 10.1016/J.PHYSREP.2017.04.001.

[99] A.D.J. Fernandez Olvera et al. ''International system of units (SI) traceable noise-equivalent power and responsivity characterization of continuous wave ErAs:InGaAs photoconductive terahertz detectors''. In: *Photonics* 6.1 (2019). DOI: 10.3390/PHOTONICS6010015.

[100] M. Tani, K.-S. Lee, and X.-C. Zhang. ''Detection of terahertz radiation with low-temperature-grown GaAs-based photoconductive antenna using 1.55 μm probe''. In: *Applied Physics Letters* 77.9 (2000), pp. 1396–1398. DOI: 10.1063/1.1289914.

[101] M. Susuki, M. Tonuchi, and Y.-J. Lin. ''Fe-implanted InGaAs photoconductive terahertz detectors triggered by 1.56 μm femtosecond optical pulses''. In: *Applied Physics Letters* 86 (2005), p. 163504. DOI: 10.1063/1.1901817.

[102] A. Takazato et al. ''Detection of terahertz waves using low-temperature-grown InGaAs with 1.56 μm pulse excitation''. In: *Applied Physics Letters* 90 (2007). DOI: 10.1063/1.2712503.

[103] J.C. Delagnes et al. ''High photocarrier mobility in ultrafast ion-irradiated In0.53Ga0.47As for terahertz applications''. In: *Journal of Physics D: Applied Physics* 42.19 (2009). DOI: 10.1088/0022-3727/42/19/195103.

[104] B. Globisch et al. ''Terahertz detectors from Be-doped low-temperature grown InGaAs/InAlAs: Interplay of annealing and terahertz performance''. In: *AIP Advances* 6 (2018), p. 125011. DOI: 10.1063/1.4971843.

[105] U. Nandi et al. ''ErAs:In(Al)GaAs photoconductor-based time domain system with 4.5 THz single shot bandwidth and emitted terahertz power of 164 μW''. In: *Optics Letters* 45.10 (2020), pp. 2812–2815. DOI: 10.1364/OL.3888709.

[106] U. Nandi et al. ''Material properties and performance of ErAs:In(Al)GaAs photoconductors for 1550 nm laser operation''. In: *Journal of Vacuum Science & Technology A: Vacuum, Surfaces, and Films* 39.2 (2021), p. 023407. DOI: 10.1116/6.0000773.

[107] R.B. Kohlhaas et al. ''Photoconductive terahertz detectors with 105 dB peak dynamic range made of rhodium doped InGaAs''. In: *Applied Physics Letters* 114 (2019), p. 221103. DOI: 10.1063/1.5095714.

[108] M. Griebel et al. ''Tunable subpicosecond optoelectronic transduction in superlattices of self-assembled ErAs nanoislands''. In: *Nature Materials* 2 (2003), pp. 122–126. DOI: 10.1038/NMAT819.

[109] M. Sukhotin et al. ''Photomixing and photoconductor measurements on ErAs/InGaAs at 1.55 μm''. In: *Applied Physics Letters* 82.18 (2003), pp. 3116–3118. DOI: 10.1063/1.1567459.

[110] C.W. Berry et al. ''Significant performance enhancement in photoconductive terahertz optoelectronics by incorporating plasmonic contact electrodes''. In: *Nature Communications* 4.1 (2013), pp. 1182–1189. DOI: 10.1038/NCOMMS2638.

[111] N.T. Yardimci, D. Turan, and Jarrahi M. ''Efficient photoconductive terahertz detection through photon trapping in plasmonic nanocavities''. In: *APL Photonics* 8 (2021). DOI: 10.1063/5.0055332.

[112] J. Zmuidzinas et al. ''Room Temperature, Quantum-Limited THz Heterodyne Detection? Not Yet''. In: *arXiv* (2019). DOI: arXiv:1907.13198v1.

[113] P.-K. Lu, D. Turan, and M. Jarrahi. ''High-sensitivity telecommunication-compatible photoconductive terahertz detection through carrier transit time reduction''. In: *Optics Express* 28.18 (2020), pp. 26324–26335. DOI: 10.1364/OE.400380.

[114] J.Y. Suen et al. ''Measurement and modeling of ErAS:$In_{0.53}Ga_{0.47}As$ nanocomposite photoconductivity for THz generation at 1.55 μm pump wavelength''. In: *Journal of Applied Physics* 116.1 (2014), p. 013703. DOI: 10.1063/1.4886180.

[115] Y. Huo, G.W. Taylor, and R. Bansal. ''Planar log-periodic antennas on extended hemispherical silicon lenses for millimeter/submillimeter wave detection applications''. In: *International Journal of Infrared and Millimeter Wavers* 23.6 (2002), pp. 819–839. DOI: 10.1023/A:1015738932198.

[116] TOPTICA Photonics. *TeraScan*. 2021. URL: https://www.toptica.com/products/terahertz-systems/frequency-dpmain/terascan/.

[117] J. Xu et al. ''Limit of spectral resolution in terahertz time-domain spectroscopy, absolute spectroscopy''. In: *Chinese Physical Letters* 20.8 (2003), pp. 1266–1268. DOI: 10.1088/0256-307X/20/8/324.

[118] T. Yasui, E. Saneyoshi, and T. Araki. ''Asynchronous optical sampling terahertz time-domain spectroscopy for ultrahigh spectral resolution and rapid data acquisition, absolute spectroscopy''. In: *Applied Physics Letters* 87 (6 2005). DOI: 10.1063/1.2008379.

[119] M. Yahyapour et al. ''Fastest thickness measurements with a terahertz time-domain system based on electronically controlled optical sampling''. In: *Applied Sciences* 9 (2019). DOI: 10.3390/APP9071283.

[120] D. von der Linde. ''Characterization of the noise in continuously operating mode-locked lasers''. In: *Applied Physics B* 39 (1986), pp. 201–217. DOI: 10.1007/BF00697487.

[121] R. Paschotta. ''Timing jitter and phase noise of mode-locked fiber lasers''. In: *Optics Express* 18.5 (2010), pp. 5041–5054. DOI: 10.1364/OE.18.005041.

[122] A.D.J. Fernandez Olvera et al. ''Frequency selective optoelectronic down-converstion of a terahertz pulse using ErAs:In(Al)GaAs photoconductors''. In: *IEEE Access* 9 (2021), pp. 95391–95400. DOI: 10.1109/ACCESS.2021.3094358.

[123] A.S. Pavelyev D.G. Skryl and M.I. Bakunov. ''High-resolution broadband terahertz spectroscopy via electronic heterodyne detection of a photonically generated terahertz frequency comb''. In: *Optics Letters* 39.19 (2014), pp. 5669–5672. DOI: 10.1364/OL.39.005669.

[124] A. Neto et al. ''The leaky lens: A broad-band fixed-beam leaky-wave antenna''. In: *IEEE Transactions on Antennas and Propagation* 53.10 (2005), pp. 3240–3246. DOI: 10.1109/TAP.2005.856351.

[125] R.H. Frankel M.Y. Voelker and J.N. Hilfiker. ''Coplanar transmission lines on thin substrates for high-speed low-loss propagation''. In: *IEEE Transactions on Microwave Theory and Techniques* 42.3 (1994), pp. 396–402. DOI: 10.1109/22.277432.

[126] A. Garufo et al. ''Norton equivalent circuit for pulsed photoconductive antennas–part II: Experimental validation''. In: *IEEE Transactions on Antennas and Propagation* 66.4 (2018), pp. 1646–1659. DOI: 10.1109/TAP.2018.2800704.

[127] E.W. Weisstein. *Jacobi-Anger expansion*. 2021. URL: https://mathworld.wolfram.com/Jacobi-AngerExpansion.html.

[128] Z. Tong et al. ''Spectral linewidth preservation in parametric frequency combs seeded by dual pumps''. In: *Optics Express* 20.16 (2012), pp. 17610–17619. DOI: 10.1364/OE.20.017610.

[129] A. Roggenbuck et al. ''Using a fiber stretcher as a fast phase modulator in a continuous wave terahertz spectrometer''. In: *Journal of the Optical Society of America B* 29.4 (2012). DOI: 10.1364/JOSAB.29.000614.

[130] EEsof EDA Keysight. *Overview on phase noise and jitter*. Tech. rep. Keysight Technologies, 2017.

[131] A.R. Criado et al. ''Continuous-wave sub-THz photonic generation with ultra-narrow linewidth, ultra-high resolution, full frequency range coverage and high long-term frequency stability''. In: *IEEE Transactions on Terahertz Science and Technology* 3.4 (2013), pp. 461–471. DOI: 10.1109/TTHZ.2013.2260374.

[132] H.A. Haus and A. Mecozzi. ''Noise of mode-locked lasers''. In: *IEEE Journal of Quantum Electronics* 29.3 (1993), pp. 983–996. DOI: 10.1109/3.206583.

[133] E. Prior et al. ''1 THz span optical frequency comb Using VCSELs and off the shelf expansion techniques''. In: *The 2016 Conference on Lasers and Electro-Optics (CLEO)* (San Jose, CA, USA). IEEE, June 2016, pp. 2461–2463. ISBN: 978-1-5090-2434-6.

[134] R.B. Kohlhaas et al. ''637 μW emitted terahertz power from photoconductive antennas based on rhodium doped InGaAs''. In: *Applied Physics Letters* 117 (2020). DOI: 10.1063/5.0020766.

[135] Virginia Diodes. *Spectrum Analyzer Extension Modules*. 2021. URL: https://www.vadiodes.com/en/products/spectrum-analyzer.

[136] RPG Radiometer Physics. *FS-Z Mixers*. 2021. URL: https://www.radiometer-physics.de/products/mmwave-and-terahertz-products/spectrum-analyzer-extenders/fs-z-mixers/.

[137] Rohde & Schwarz. *R&S FSW signal and spectrum analyzer*. 2021. URL: https://www.rohde-schwarz.com/us/products/test-and-measurement/benchtop-analyzers/rs-fsw-signal-and-spectrum-analyzer_63493-11793.html.

[138] S. Schiller et al. ''Ultra-narrow-linewidth continuous-wave THz sources based on multiplier chains''. In: *Applied Physics B* 95 (2009), pp. 55–61. DOI: 10.1007/s00340-008-3279-9.

[139] A. Hati, C.W. Nelson, and D.A. Howe. ''PM Noise Measurement at W-Band''. In: *IEEE Transactions on Ultrasonics, Ferroelectrics, and Frequency Control* 61.12 (2014), pp. 1961–1966. DOI: 10.1109/TUFFC.2014.006647.

[140] S. Yokoyama et al. ''Terahertz spectrum analyzer based on a terahertz frequency comb''. In: *Optics Express* 16 (17 2008), pp. 13052–13061. DOI: 10.1364/OE.16.013052.

[141] T. Yasui et al. ''Real-time monitoring of continuous-wave terahertz radiation using a fiber-based, terahertz-comb-referenced spectrum analyzer''. In: *Optics Express* 17 (9 2009), pp. 17034–17043. DOI: 10.1364/OE.17.017034.

[142] G. Hu et al. ''Measurement of absolute frequency of continuous-wave terahertz radiation in real time using a free-running, dual-wavelength mode-locked, erbium-doped fibre laser''. In: *International Journal of Infrared and Millimeter Wavers* 7 (2017). DOI: 10.1038/SREP42082.

[143] N. Wang and M. Jarrahi. ''High-precision millimeter-wave frequency determination through plasmonic photomixing''. In: *Optics Express* 28.17 (2020), pp. 24900–24907. DOI: 10.1364/OE.400806.

[144] S. Preu. *Device and Method for Spectral Analysis*. U.S. Patent 0025614 A1. 2020.

[145] A.D.J. Fernandez Olvera, B.L. Krause, and S. Preu. ''A true optoelectronic spectrum analyzer for millimeter waves with Hz resolution''. In: *IEEE Access* 9 (2021), pp. 114339–114347. DOI: 10.1109/ACCESS.2021.3105030.

[146] R. Gotti et al. ''Comb-locked frequency-swept synthesizer for high precision broadband spectroscopy''. In: *Scientific Reports* 10 (2020). DOI: 10.1038/S41598-020-59398-1.

[147] M.-C. Lo et al. ''Mode-locked laser with pulse interleavers in a monolithic photonic integrated circuit for millimeter wave and terahertz carrier generation''. In: *Optics Letters* 42.8 (2017), pp. 1532–1535. DOI: 10.1364/OL.42.001532.

[148] A.D.J. Fernandez Olvera et al. ''W-Band heterodyne wireless system with 2.3 GHz intermediate frequency driven entirely by ErAs:In(Al)GaAs photoconductors''. In: *21st International Conference on Transparent Optical Networks (ICTON)* (Angers, France). IEEE, July 2019.

[149] Y. Dong et al. ''System integration and packaging of a terahertz photodetector at W-Band''. In: *IEEE Transactions on Components, Packaging and Manufacturing Technology* 9.8 (2019), pp. 1486–1494. DOI: 10.1109/TCPMT.2019.2928053.

Supervised Student Theses

- **Xiyao Zhao** *Circuit Design of Photonic Terahertz-Spectrum Analyzer*, Master Thesis, August 2019
- **Seyedeh Melika Rateghi** *Noise Squeezing in Photomixers for Terahertz Detection*, Master Thesis, July 2020

Curriculum Vitae

Personal Details

Name	Anuar de Jesus Fernandez Olvera
Date of birth	22.08.1988
Place of birth	Alvarado, Veracruz, Mexico

Education

Aug. 2006 - Dec. 2010	ITESM Estado de Mexico (magna cum laude) B.Sc. in Electronic and Computer Engineering
Aug. 2013 - Sept. 2015	TU Eindhoven M.Sc. in Electrical Engineering (cum laude)
Jun. 2016 - Feb. 2022	TU Darmstadt Dr-Ing. in Electrical Engineering (summa cum laude)

Employment

Aug. 2011 - Jul. 2013	QuetzSat Mexico Satellite Controller
Jun. 2016 - Present	TU Darmstadt Research Assistant at the Institute for Microwave Engineering and Photonics

Languages

Spanish: Fluent

English: Fluent

German: Basic

Erklärung laut Promotionsordnung

§ 8 Abs. 1 lit. c PromO
Ich versichere hiermit, dass die elektronische Version meiner Dissertation mit der schriftlichen Version übereinstimmt.

§ 8 Abs. 1 lit. d PromO
Ich versichere hiermit, dass zu einem vorherigen Zeitpunkt noch keine Promotion versucht wurde. In diesem Fall sind nähere Angaben über Zeitpunkt, Hochschule, Dissertationsthema und Ergebnis dieses Versuchs mitzuteilen.

§ 9 Abs. 1 PromO
Ich versichere hiermit, dass die vorliegende Dissertation selbstständig und nur unter Verwendung der angegebenen Quellen verfasst wurde.

§ 9 Abs. 2 PromO
Die Arbeit hat bisher noch nicht zu Prüfungszwecken gedient.

Darmstadt, 30. November 2021

Datum und Unterschrift